Development and Validation of a Computational Model for a Proton Exchange Membrane Fuel Cell

Nathan Phillip Siegel

Dissertation Submitted to the Faculty of
Virginia Polytechnic Institute and State University
in partial fulfillment of the requirements for the degree of

DOCTOR OF PHILOSOPHY
in
Mechanical Engineering

Committee Members:

Dr. Michael Ellis, Chair
Dr. Douglas Nelson
Dr. Michael von Spakovsky
Dr. Donald Leo
Dr. Benoît Olsommer

December 18, 2003
Blacksburg, Virginia

Keywords: Fuel cell, PEMFC, CFD, Modeling, Agglomerate, Catalyst

Development and Validation of a Computational Model for a Proton Exchange Membrane Fuel Cell

Nathan P. Siegel

Abstract

A steady-state computational model for a proton exchange membrane fuel cell (PEMFC) is presented. The model accounts for species transport, electrochemical kinetics, energy transport, current distribution, water uptake and release within the polymer portion of the catalyst layers, and liquid water production and transport. Both two-dimensional and three-dimensional geometries are modeled. For a given geometry, the governing differential equations are solved over a single computational domain. For the two-dimensional model, the solution domain includes a gas channel, gas diffusion layer, and catalyst layer for both the anode and cathode sides of the cell as well as the solid polymer membrane. For the three-dimensional model the current collectors are also modeled on both the anode and cathode sides of the fuel cell.

The model for the catalyst layers is based on an agglomerate geometry, which requires water species to exist in dissolved, gaseous, and liquid forms simultaneously. Data related to catalyst layer morphology that was required by the model was obtained via a physical analysis of both commercially available and in-house membrane electrode assemblies (MEA). Analysis techniques including cyclic voltammetry and electron microscopy were used.

The coupled set of partial differential equations is solved sequentially over a single solution domain with the commercial computational fluid dynamics (CFD) solver, CFDesign™ and is readily adaptable with respect to geometry and material property definitions.

A fuel cell test stand was designed and built to facilitate experimental validation of the model. The test stand is capable of testing cells up to 50 cm^2 under a variety of controlled conditions.

Model results for both two and three-dimensional fuel cell geometries are presented. Parametric studies performed with the model are also presented and illustrate how fuel cell performance varies due to changes in parameters associated with the transport of reactants and liquid water produced in the cell. In particular, the transport of oxygen, water within the polymer portions of the catalyst layers and membrane, and liquid water within the porous regions of the cell are shown to have significant impact on cell performance, especially at low cell voltage. Parametric studies also address the sensitivity of the model results to certain physical properties, which illustrates the importance of accurately determining the physical properties of the fuel cell components on which the model is based. The results from the three-dimensional model illustrate the impact of the collector plate shoulders (for a conventional flowfield) on oxygen transport and the distribution of current production within the cell.

Acknowledgements

I would like to thank my thesis committee, Drs. Ellis, Nelson, von Spakovsky, Olsommer, and Leo for taking the time to review this dissertation. I would especially like to thank Drs. Ellis, Nelson, and von Spakovsky for their support and advice over the course of the last three years. Even though we spent more time in our meetings discussing topics completely unrelated to fuel cells, I still learned a great deal. Dr. Olsommer's work on a mathematical fuel cell model was also very helpful throughout this project. I'd also like to thank former graduate students Brandon Eaton, Daniel Genevey, and Jason Russell for their help in developing the fuel cell model and test stand. I would like to thank Dr. Rita Schnipke, of Blue Ridge Numerics, for her help in adapting the software used in solving the numerical model which makes up the bulk of the work presented herein. Lastly, I would like to acknowledge all of the people who, although not directly connected with this project, assisted in its completion in one way or another, usually by giving me an excuse *not* to work on the project. I thank you all.

Dedication

To Adam, Beth, and Johnny Cash.

Preface

This work was completed at Virginia Polytechnic Institute and State University and funded in part by the Department of Energy GATE Program and the Department of Mechanical Engineering at Virginia Tech. Additional funding was provided by the United States Department of Energy under Contract No. DE-FC36-01G01186.

Table of Contents

List of Figures

List of Tables

Nomenclature

Subscripts

a	anode
act	activation
Adv	advective
aggl	agglomerate
c	cathode
C	carbon
cat	carbon supported catalyst
d	index for electrodes (anode: d=a, cathode: d=c)
Dar	Darcy pressure loss
drag	electro-osmotic drag
e	electrical
eff	effective
evap	evaporation
gdl	gas diffusion layer
H_2	hydrogen
i	ionic
e	electric
j	denotes gas species
k	denotes gas species
LV	mass transfer from liquid to vapor
mix	gas mixture
O_2	oxygen
p	polymer
pc	phase change
pl	current collector plate
Pt	platinum
rev	reversible heat
SAT	saturated
v	vapor
W	water
WD	water dissolved in polymer
WV	water vapor
WL	water liquid
WP	water production
x	x direction
y	y direction
z	z direction
Ω	ohmic

Superscripts

cp	capillary pores
g	gas phase

p	polymer phase
v	vapor phase
c	critical (as in critical pressure)
L	liquid
Sat	saturated

Parameters and variables

a	water vapor activity
A	catalyst surface area per catalyst layer volume, mm^2/mm^3
c	concentration, mol/mm^3
c_{eff}	effective heat capacity, J/g-K
c_{WL}	heat capacity of liquid water, J/g-K
c_g	heat capacity of the gas mixture, J/g-K
d	diameter, mm
D	diffusion, mm^2/s
E_{th}	Nernst potential, V
F	Farraday's constant, 96485 col/mol e^-
g	acceleration of gravity, 981 mm^2/s
h_{fg}	enthalpy of vaporization, J/g
h_m	water vapor / dissolved water mass transfer coefficient, s^{-1}
I	local current density, A/mm^2
k_{eff}	effective thermal conductivity, W/mm-K
K_L	liquid water permeability, mm^2
K_{Abs}	absolute permeability, mm^2
m	mass, g
M	molar mass, g/mol
N	species flux, g/mm^2-s
n	number of electrons
P	pressure, Pa
P_c	capillary pressure, Pa
Q	charge, μC
r_m	radius of curvature, mm
R	ideal gas constant, J/mol-K
R_d	reaction rate at an electrode, A/mm^3
R_{eff}	effective reaction rate, A/mm^3
s	liquid water saturation
S	source term – see Table 2
S_{tafel}	tafel slope, mV/decade
s_f^o	standard entropy of formation, J/mol-K
t	thickness, mm
T	temperature, K
u	mass average velocity, mm/s
V_{cell}	cell voltage, V
V_s	solid volume, mm^3
V_{tot}	total volume, mm^3

w	mass fraction
x	weight percent
y	mole fraction
α	charge transfer coefficient
β	Thiele's modulus
ε	porosity or volume fraction
κ	gas permeability, mm^{-2}
λ	polymer water content, H_2O/SO_3^-
ϕ	potential, V
η_{aggl}	effectiveness
ρ	density, g/mm^3
σ	ionic conductivity, $(\Omega\text{-mm})^{-1}$
ψ	liquid – vapor mass transfer coefficient, s^{-1}
Γ	surface tension, N/mm
τ	tortuosity
μ	viscosity, Pa-s
χ	tortuosity
γ	switch function

1 Introduction

Hydrogen may well be the energy carrier of the future. In the United States in particular a major change in the energy infrastructure, a transition from fossil fuels to hydrogen, appears to be on the horizon. This change, which comes amid concerns of an increasing dependence on an uncertain supply of foreign oil, will be made possible by several key technologies that allow for the efficient production, storage, and usage of hydrogen. One of these technologies is the fuel cell.

Fuel cells, which were invented 164 years ago by William Grove, have only recently become economically competitive with traditional power systems, such as the internal combustion engine. This is due primarily to innovations over the last couple of decades that have taken fuel cells from the very costly, yet short-lived systems used in the early U.S. space program, to the less expensive systems now appearing in cars, as backup generators for hospitals, and even in portable electronic devices such as laptops. In this chapter, an overview of fuel cell technology is given, the proton exchange membrane fuel cell (PEMFC) is introduced, computational modeling of PEMFCs is discussed, and the objectives of this work are presented.

1.1 Fuel Cell Technology

Simply put, a fuel cell is a device that converts the chemical energy of a fuel directly to electrical energy. The process by which this is done is very similar to the electrochemical process by which a battery generates power; at one electrode, a fuel such as hydrogen is oxidized, and at the other electrode an oxidant such as oxygen is reduced. The reactions exchange ions through a solid or liquid electrolyte and electrons through an external circuit. There are typically two principal differences between a fuel cell and a battery. The first is that, in a fuel cell, the electrodes themselves are not chemically changed during the reaction. The second is that fuel cells are open systems, with fuel and oxidant flowing through the cell, whereas batteries are typically closed systems containing a set amount of fuel and oxidant that is gradually consumed via chemical reaction.

The electrochemical reaction occurring in a fuel cell depends on the type of cell, as well as the chemical composition of the fuel and oxidant. The overall chemical reaction for a fuel cell running on hydrogen and oxygen is shown in Eq. (1.1).

$$H_2 + \tfrac{1}{2}O_2 \rightarrow H_2O \qquad (1.1)$$

This overall reaction is the sum of the reactions occurring at the two electrodes. At the cathode, oxygen is reduced and combines with protons to form water. At the anode, hydrogen is oxidized to form protons and electrons. These reactions are shown in Figure 1.1 along with a diagram of a fuel cell.

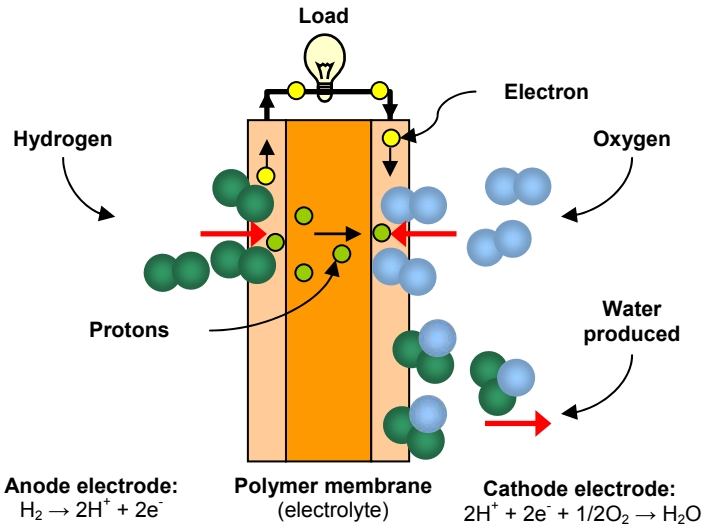

Figure 1.1 An illustration of a hydrogen / air fuel cell.

Figure 1.1 shows the components common to proton exchange membrane fuel cells. First, there is a region where reactants can enter and exit the fuel cell. The electrochemical reactions take place at the electrodes, which in most cases are made of porous material to maximize the reaction surface area. In many types of fuel cells, the electrodes contain a catalyst, usually platinum, to facilitate the chemical reactions. The electrodes are connected by an external circuit, through a load. Electrons can follow this circuit from the anode to the cathode of the fuel cell. The electrolyte can be solid or liquid and serves to separate the reactants at the two electrodes and to conduct ions from one electrode to the other.

There are many different types of fuel cells, the principle differences between them being the type of electrolyte and / or the type of fuel that they use. For instance, both the

phosphoric acid fuel cell (PAFC) and the molten carbonate fuel cell (MCFC) have a liquid electrolyte whereas a solid oxide fuel cell (SOFC) has a solid, ceramic electrolyte. A proton exchange membrane fuel cell (PEMFC) and a direct methanol fuel cell (DMFC) may have the same solid polymer electrolyte, but the DMFC uses liquid methanol for fuel whereas the PEMFC uses gaseous hydrogen. Some of the more common types of fuel cells, along with some of their distinctive characteristics, are listed in Table 1.1.

Table 1.1 Fuel cell characteristics.

Type	*Power Density, kW/m^2*	*Operating Temperature, C*	*Startup Time, sec*	Application
PEMFC	2.6-5.0	40-100	Sec-min	*Automotive, residential*
DMFC	0.6	80	Sec-min	*Portable electronics*
SOFC	1.5-6.5	600-1000	hours	*Industrial, commercial, residential*
MCFC	0.75-1.8	650	hours	*Industrial, commercial*
PAFC	0.9-3.2	220	*hours*	*Industrial, commercial*

Currently, there are three general areas of application for fuel cell technology: portable power, distributed power, and transportation (automotive in particular). For each application it is generally found that one type of fuel cell is better suited than the others to satisfy the requirements of the application. The DMFC, which has a low operating temperature and a relatively high fuel storage density, in the form of a liquid methanol solution, is well suited to portable power applications, such as powering personal electronic devices. The SOFC, because of its high power density and high grade waste heat that may be

used in cogeneration applications, is a frontrunner in distributed power applications at the industrial level. The PEMFC has many of the qualities required of an automotive power system including relatively low operating temperature, high power density, and rapid startup. In addition, PEMFC's may also be used in residential and commercial power systems.

1.2 Proton Exchange Membrane Fuel Cells

Figure 1.2 shows a PEMFC text fixture that uses hydrogen as the fuel and either oxygen or air as the oxidant. The cell consists of a current collector (including gas channels), gas diffusion layer, and catalyst layer on the anode and cathode sides as well as an ion conducting polymer membrane.

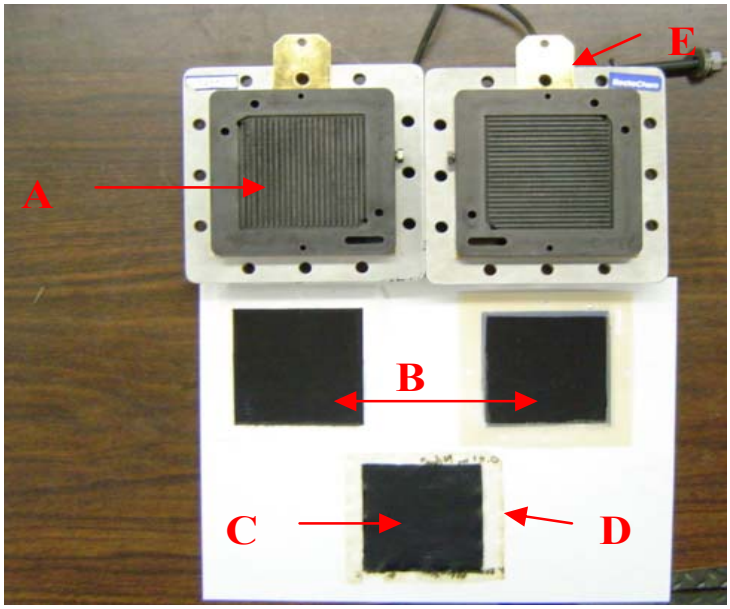

Figure 1.2 A proton exchange membrane fuel cell test fixture.

Reactants enter the cell through gas channels (labeled A in Figure 1.2), which are embedded in the current collectors. The gas diffusion layers (GDL), labeled B, are made of carbon cloth or paper and serve to uniformly distribute the reactants across the surface of the catalyst layers, C, as well as to provide an electrical connection between the catalyst layers and the current collectors. As mentioned earlier, the electrochemical reactions that drive a

fuel cell occur in the catalyst layers which are attached to both sides of the membrane, D. The catalyst layers must be designed in such a manner as to facilitate the transport of protons, electrons, and gaseous reactants. Protons, produced by the oxidation of hydrogen on the anode, are transported through ion conducting polymer within the catalyst layers and the membrane. Electrons produced at the anode are transported through the electrically conductive portion of the catalyst layers, usually a graphite catalyst support structure or the metallic catalyst itself, to the gas diffusion layers, then to the collector plates and through the bus plates, E, to the load, and finally to the cathode. Gaseous reactants are transported by both diffusion and advection through pores in the catalyst layers. Protons are conducted across the polymer membrane from the anode, where they are produced, to the cathode where they combine with oxygen and electrons to form water, which may be in vapor or liquid form, depending on the local conditions. Liquid water is transported through the pores in the catalyst and gas diffusion layers through a mechanism that may be similar to capillary flow. Upon reaching the gas channels, liquid water is transported out of the cell along with the bulk gas flow. Water may also be transported, in dissolved form, through the polymer portion of the catalyst layers and through the membrane. The mechanisms of dissolved water transport are diffusion, due to a concentration gradient between anode and cathode, and electro-osmotic drag (EOD). EOD is a term used to describe an interaction between water molecules dissolved in the polymer and protons being conducted through the polymer that causes water molecules to be dragged by the protons from the anode to the cathode. Figure 1.3 shows a diagram of the various transport mechanisms occurring in a PEMFC.

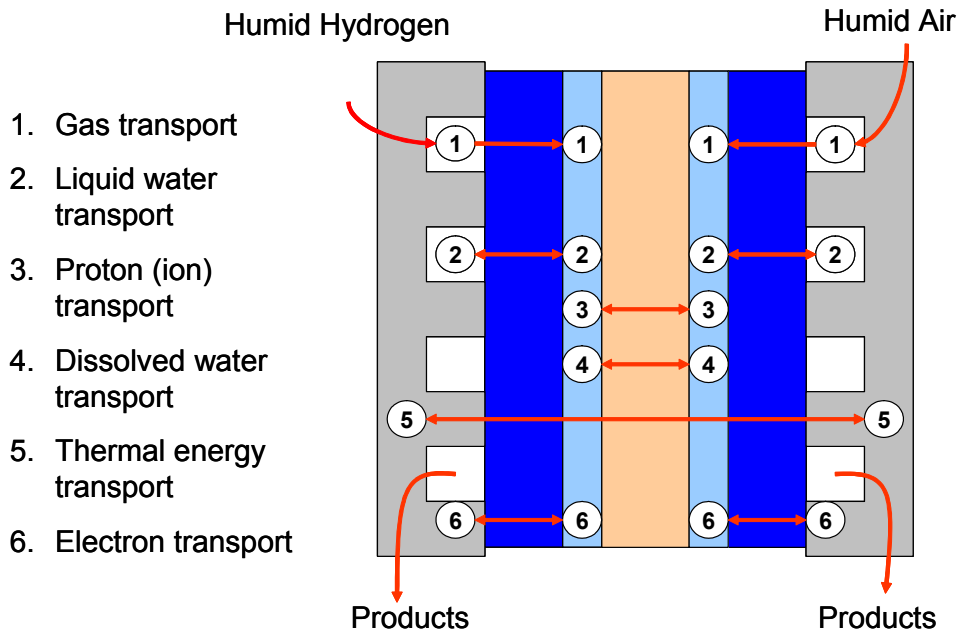

Figure 1.3 Transport processes in a PEMFC.

Heat produced in the cell is removed principally by conduction through the cell and convection by a coolant in contact with the collector plates. Most PEMFC's are approximately 50% efficient and any chemical energy that is not converted to electricity appears as a heat interaction. Chemical energy is converted to thermal energy by a variety of processes including ohmic resistance, the energy associated with initiating the chemical reactions (activation), and reversible heat transfer. For a PEMFC, performance increases with temperature up to the glass transition temperature of the polymer membrane. Great care must be taken to remove enough thermal energy to ensure that the cell, particularly the polymer membrane, does not overheat while at the same time maintaining a high enough temperature to maximize performance.

1.3 Fuel Cell Modeling

A computational fuel cell model is a mathematical representation of the physical phenomena (including electrochemical processes) governing fuel cell operation. This generally includes a set of differential equations and boundary conditions, which define the

transport processes within a fuel cell, and closure relations (or coupling equations) which express how the transport equations are related to one another. Additional equations that define the physical properties of the materials used in a given fuel cell are also needed. Once the mathematical model is developed, the resulting set of equations is solved numerically using a finite element or computational fluid dynamics (CFD) solver or other numerical method.

Computational models of PEMFC's are primarily useful in two regards. First, they offer a means of learning more about the complex physical phenomena governing fuel cell performance. For example, due to the nature of fuel cells, it is difficult to evaluate many of the physical phenomena *in situ*. With a model, this information, which would otherwise be difficult to obtain, is readily accessible. Computational models are also useful design tools. For instance, one might use a fuel cell model to perform parametric studies on a given design to evaluate its performance and identify areas in need of improvement.

The models themselves can be simple, focusing on one or more physical phenomena, or complex and comprehensive in scope [1-18]. The advantage of a simple model is that a great deal of information may be gained in a short period of time, since a simple model can be solved much more quickly than can a large, comprehensive model. Conversely, a comprehensive model will take longer to solve, but will yield much more information than a simple model. A comprehensive model is necessary when attempting to simulate how all of the phenomena occurring in a fuel cell are related to one another.

1.4 Research Objectives

The principal objective of this research is to create a comprehensive, computational model of a PEMFC that satisfies the following three criteria:

- The model is based on a mathematical description of fuel cell physics derived from first principles and can be solved in one, two, and three dimensions.
- The model is useful as a learning tool in that it can facilitate a greater understanding of the physical phenomena that govern fuel cell behavior.

- The model is useful as a design tool in that it allows for the evaluation of fuel cell design concepts. This requires that the model be flexible with respect to geometry and material properties.

In support of and in addition to the principal research objectives, the following objectives are also established:

- Experimentally characterize MEA's fabricated at Virginia Tech to determine physical parameters required by the model.
- Experimentally validate the modeling results.
- Conduct parametric studies using a two-dimensional model with particular attention given to the effects of the catalyst layer structure on cell performance and liquid water transport.

The remainder of this dissertation is organized into six sections as follows.

- A literature review containing summaries of existing fuel cell modeling work as well as research done in the area of physical property characterization.
- A description of the mathematical foundation of the computational fuel cell model.
- A discussion of the physical properties required to create a useful and accurate computational model.
- A discussion of numerical considerations related to the actual solution of the computational model.
- Results generated with the model including a comparison of 2D and 3D geometries as well as parametric studies.
- A section summarizing the conclusions that may be drawn from the research presented in this dissertation.

2 Literature Review

Within the literature there are many types of fuel cell models. In some cases, these models are aimed at examining specific phenomena, such as water management and flooding. In other cases the models are very broad in scope and used to describe, as fully as possible, all of the relevant transport mechanisms within the cell. In general, it is possible to categorize all models as belonging to one of two categories: partial cell models or complete cell models. Partial cell models include only a few of the components of a fuel cell, such as the membrane and the GDL. The membrane model by Eaton et al. [7] is an example of this type. In this work, transport of protons, dissolved water, and energy are modeled for the membrane only. The advantage of this type of model is that it is possible to simulate, in significant detail, specific transport mechanisms and still retain a relatively short solution time. Complete cell models include all or nearly all of the components of the fuel cell. The work of Um, Wang, and Chen [15] is an example of this type of model. In this case, the transport of species and protons is included in a two-dimensional, down-the-channel geometry. The advantage of this, more general model, is that it allows for a more accurate simulation of fuel cell performance. This comes at the cost of increased computation time and complexity. A review of existing fuel cell models is presented in Section 2.1, Partial Cell Models, and Section 2.2, Full Cell Models, and the accompanying tables.

All fuel cell models rely on certain physical properties, an accurate determination of which is needed to accurately simulate fuel cell operation. Examples of these properties include kinetic parameters such as exchange current density and catalyst surface area per unit volume, structural information such as porosity and tortuosity of the porous GDL, and properties of the polymer such as ionic conductivity and dissolved water diffusivity. Section 2.3, along with the accompanying tables, provides a review of the existing literature dealing with the characterization of the physical properties of fuel cell components.

2.1 Partial Cell Models

One of the more important aspects of fuel cell operation is water management, which involves how water is transported within the cell. In their work, Springer, Zawodzinski, and Gottesfeld [1] explore how water is transported through the polymer membrane (Table 2.1). Their paper has two sections. The first is the development of a computational model of a PEMFC that includes the gas diffusion layers and the membrane. The catalyst layers are treated as interfaces where source terms are applied. The second section includes experimental data for properties related to water uptake and transport through Nafion® 117 membranes. The water content of the membrane is given as a function of local vapor activity, and both the diffusion coefficient of water and the ionic conductivity of the membrane are given as a function of water content and temperature. In addition, a relation is derived that accounts for the amount of water transport by electro-osmotic drag per proton crossing the membrane from anode to cathode. Combining the experimental data with the computational model, Springer et al. generate cell performance curves for a range of operating conditions and also use the model to predict the net amount of water transport across the cell from anode to cathode. This turns out to be much less than what would be transported by electro-osmotic drag alone and indicates the importance of back diffusion from cathode to anode. The model itself is well suited to investigating water transport in the membrane, but since it is one dimensional and does not explicitly include the catalyst layers, it cannot be used to quantitatively model cell performance.

Table 2.1 Springer, Zawodzinski, and Gottesfeld (1991).

Model	Polymer Electrolyte Fuel Cell Model (1991)
Authors	Springer, Zawodzinski, and Gottesfeld [1]
Regions	• Polymer membrane and both gas diffusion layers
Dimensionality	• One – through the thickness
Assumptions	• Steady-state • Isothermal • One-dimensional • Catalyst is an interface • Polymer water content data at 30 C applies at 80 C • Liquid water effects neglected
Phenomena investigated	• Transport of water and protons through the polymer membrane • Changes in ionic resistance with current density and water content • Effect of membrane temperature and thickness on performance
Main conclusions	• Net water flux across the membrane is less than that predicted by electro-osmotic drag alone • Thinner membranes offer advantages in decreased resistance and water flux from anode to cathode
Limits	• The model focuses principally on performance issues associated with the polymer membrane alone and does not consider liquid water accumulation and the related mass transport effects.

Springer and Gottesfeld [2] present a computational model of the cathode catalyst layer based on a pseudohomogenous structure (Table 2.2). They assume that reactants are transported through a hybrid catalyst medium consisting of both gas pores and polymer which is modeled with a single effective diffusion coefficient and local concentration. The

model also accounts for ionic transport through the polymer. The results show that the model is able to predict the gradual change in slope seen in fuel cell performance curves at high current density. However, it does this without accounting for liquid water accumulation, which has been shown to influence performance at high loads [8, 10]. This indicates that the model predicts the right results, but for the wrong reasons.

Table 2.2 Springer and Gottesfeld (1992).

Model	**Pseudohomogenous Catalyst Layer Model for Polymer Electrolyte Fuel Cell (1992)**
Authors	Springer and Gottesfeld [2]
Regions	• Cathode catalyst layer
Dimensionality	• One – through the thickness
Assumptions	• Steady-state • Isothermal • Pseudo-homogenous catalyst layer structure • The electrical conductivity of the catalyst layer is infinite • Imposed limiting current
Phenomena investigated	• Performance limitation at high current density • Performance variation when using air vs. oxygen as the oxidant
Main conclusions	• The pseudo-homogenous model can be used to qualitatively explain gradual performance drop off at high current densities.
Limits	• Liquid water effects are neglected

Broka and Ekdunge [3] present a model for the cathode catalyst layer based on an agglomerate structure (Table 2.3). They assume that reactants are transported through gas pores in the catalyst and, upon reaching an agglomerate, dissolve into and diffuse through the surrounding polymer to reach the reaction sites within. The principle difference between this model and that of Springer and Gottesfeld [2] is that Broka and Ekdunge treat the diffusive resistance of the polymer in the catalyst layer not as a limitation on the diffusive flux of the

gaseous reactants, but as a limitation of the effective reaction rate using an effectiveness relationship. This type of treatment is used in heterogeneous catalysis theory [30]. The authors use SEM images to support their argument for an agglomerate catalyst structure. The results presented show that the agglomerate model can be used to predict cell performance curves up to the beginning of the mass transfer limited regime. Unfortunately, the authors do not present experimental data over the operating range covered by their modeling results. It is possible that this is because the model may deviate significantly from the experimental data at high current density. This model is somewhat limited in that a limiting current density must be externally specified rather than calculated during the simulation. In addition the model is one dimensional and does not include liquid water transport.

Table 2.3 Broka and Ekdunge (1996).

Model	**Modeling the PEM Fuel Cell Cathode (1996)**
Authors	Broka and Ekdunge [3]
Regions	• Cathode catalyst layer
Dimensionality	• One – through the thickness
Assumptions	• Steady-state • Isothermal • Diffusion through the catalyst layer either in the gas phase or in dissolved form through the polymer • Uniform catalyst distribution • Infinite electronic conductivity • Excess water is in liquid form but effects on transport are neglected.
Phenomena investigated	• Comparison of the pseudo-homogeneous and agglomerate catalyst models • Microscopic examination of an MEA to support development of the agglomerate catalyst model

Main conclusions	• The agglomerate model can more adequately fit experimental data, compared to the pseudohomogenous model, especially at high current density. • Microscopic analysis indicates that the catalyst is porous and that reactant transport occurs in the gas phase.
Limits	• The limiting current is artificially imposed using the thickness of the polymer shell surrounding the agglomerate, which is very difficult to accurately determine.

Sui et al. [4] present a comparison of a catalyst model based on a pseudohomogenous structure and one based on an agglomerate structure (Table 2.4). In their pseudohomogenous catalyst layer, it is assumed that reactant transport occurs only in the dissolved form within the polymer, i.e. no gas transport through the pores of the catalyst layer. The authors also perform a sensitivity analysis on some of the parameters commonly used to fit models to experimental data. The results show that the agglomerate model is able to achieve a closer agreement with experimental results. There is a drawback though, and that is that the agglomerate model requires the specification of many physical parameters. Even a small amount of uncertainty in these parameters, such as catalyst porosity or agglomerate size, can lead to a significant variation in the model predictions.

Table 2.4 Sui et al. (1999).

Model	**Modeling and Optimization of a PEMFC Catalyst Layer (1999)**
Authors	Sui, Chen, Seaba, and Wariishi [4]
Regions	• Cathode catalyst layer
Dimensionality	• One – through the thickness

Assumptions	• Steady-state • Isothermal • Diffusion through the catalyst layer either in the gas phase or in dissolved form through the polymer • Uniform catalyst distribution • Infinite electronic conductivity • Flooding neglected
Phenomena investigated	• Comparison of the pseudohomogeneous and agglomerate catalyst models • Investigation of model sensitivity to physical parameters
Main conclusions	• The pseudohomogenous model requires an externally imposed limiting current to fit experimental data. • The agglomerate model requires the determination of many more physical parameters than does the pseudo-homogenous model. Some of the parameters have a great deal of impact on the cell performance predicted by the model.

Marr and Li [5] present a cathode catalyst model based on a pseudohomogenous structure (Table 2.5) similar to the one used by Springer and Gottesfeld [2]. The main difference is that their reactant diffusion coefficient includes a term to account for diffusion through liquid water (although they don't explicitly solve a liquid water transport equation) and they neglect the transport of reactants in the gas phase, i.e. the pores are completely filled with water and ionomer. Their results indicate that all of the electrochemical reactions happen within a few microns of the gas diffusion layer interface. This is primarily a consequence of their assumption of no diffusion in the gas phase. They also show some results illustrating the effect on performance of both ionomer content and platinum content in the catalyst layer. The model is limited in that, by assuming a completely flooded catalyst structure, it will under-predict cell performance since reactant diffusion through the polymer or water is relatively slow when compared to that in the gas phase.

Table 2.5 Marr and Li (1999).

Model	Composition and Performance Modeling of Catalyst Layer in a Proton Exchange Membrane Fuel Cell (1999)
Authors	Marr and Li [5]
Regions	• Cathode catalyst layer
Dimensionality	• One – through the thickness
Assumptions	• Steady-state • Agglomerate catalyst structure • Catalyst layer pores are completely filled with liquid water. • Uniform catalyst distribution
Investigated phenomena	• Optimal void fraction of the catalyst layer • Optimal polymer content of the catalyst layer • Optimal weight fraction of platinum on carbon support
Main conclusions	• The cathode reaction occurs in a very thin region of the catalyst, suggesting poor utilization. • The optimal catalyst void fraction is 60% and is independent of current density. • The optimal ionomer/pore volume fraction is about 25%. • 40% Pt on carbon yields the best performance
Limits	• Cannot be used to model the performance of an entire cell. • The approximation of diffusion coefficient for oxygen within the catalyst layer is based on a series resistance model. Oxygen first dissolves through liquid water and then through a thin layer of polymer surrounding the reaction sites.

Wang and Wang [6] present a model of the gas diffusion layer that includes liquid water transport (Table 2.6). They present results for saturation profiles within the GDL, gas velocity contours for the gas and liquid phases, and a performance curve showing the increase in performance for an interdigitated flowfield relative to a conventional flowfield.

The authors use the Leverett equation to relate the capillary pressure of the liquid water within the porous GDL to the volume fraction of liquid in the pores, called the saturation. It has been speculated that the use of the Leverett equation, which is an empirical relation derived from an analysis of water transport through sand, may not be applicable to materials used in fuel cell electrodes [8]. In addition, mass transfer between the liquid and vapor phases is not considered.

Table 2.6 Wang and Wang (2000).

Model	**Two-phase Flow and Transport in the Interdigitated Air Cathode of Proton Exchange Membrane Fuel Cells (2000)**
Authors	Wang and Wang [6]
Regions	• Gas diffusion layer (cathode only) • Catalyst layer and gas channel as an interface
Dimensionality	• Two
Assumptions	• Steady state • Multi-phase • Multi-component • Performance is independent of catalyst layer transport
Phenomena investigated	• Performance effects related to liquid water transport in a cell with an interdigitated gas distributor • Performance comparison of interdigitated and conventional flow distributors
Main conclusions	• Liquid saturation values for an interdigitated gas distributor are low, about 7%, for high inlet relative humidity (96%). • The ability to more effectively remove liquid water contributes to increased performance of inderdigitated gas distributors relative to conventional ones. • The liquid water velocity is about four times slower than the gas velocity assuming that the liquid velocity can be scaled based on viscosity and permeability.

Limits	• Transport in the membrane and catalyst layer was neglected as was flow down the channel. The performance results are essentially qualitative

The model by Eaton et al. [7] includes transport equations for water, protons, and energy within the polymer membrane (Table 2.7). The authors incorporate a term in the water transport equation to account for a pressure gradient across the fuel cell. Their results show that the net water transport across the cell from anode to cathode can be reduced by applying a higher pressure on the cathode. Particular attention is paid to the transient aspects of transport. Results are presented to simulate the startup of a fuel cell under conditions similar to those that would be found in an automotive fuel cell system.

Table 2.7 Eaton et al. (2001)

Model	**One-Dimensional, Transient Model of Heat, Mass, and Charge Transfer in a Proton Exchange Membrane (2001)**
Authors	Eaton, von Spakovsky, Ellis, Nelson, Olsommer, and Siegel [7]
Regions	• Membrane
Dimensionality	• One – through the thickness
Assumptions	• Transient • Single phase • Multi-component • Linear pressure gradient
Phenomena investigated	• Performance effects related to the transfer of water, protons and energy
Main conclusions	• The water flux from anode to cathode increases with current but may be offset by the application of a pressure gradient. • The model is capable of predicting transient water concentration, voltage, and temperature profiles.
Limits	• Boundary conditions are arbitrary since the adjoining regions of the cell are not included in the model.

Natarajan and Nguyen [8] present a model for liquid water transport within the gas diffusion layer (Table 2.8). The model assumes that the motion of the water in the liquid phase is governed by capillary pressure alone and also allows for mass transfer between vapor and liquid phases. The relationship between capillary pressure and saturation is based on fuel cell test data as opposed to a relationship based on the Leverett function, which was used by Wang and Wang [6]. The authors show that their empirical relationship for the variation of capillary pressure with saturation is somewhat different from that obtainable with the Leverett equation. In addition, they include results showing the effect of the flowfield shoulders on liquid water accumulation within the cell. The model is limited in that it does not include the catalyst layers in the solution domain, and it does not include effects resulting from reactant depletion and water accumulation down the channel.

Table 2.8 Natarajan and Nguyen (2001).

Model	**A Two-Dimensional, Two-Phase, Multicomponent, Transient Model for the Cathode of a Proton Exchange Membrane Fuel Cell Using Conventional Gas Distributors (2001)**
Authors	Natarajan and Nguyen [8]
Regions	• Gas diffusion layer (cathode only) • Catalyst layer and gas channel as an interface
Dimensionality	• Two – through the thickness and across the channel
Assumptions	• Transient • Two-phase • Multi-component • Isobaric • Water transport by capillary pressure only – no advection

Phenomena investigated	• Influence of liquid water on cell performance • Effect of current collector shoulder on performance, specifically with regard to liquid water transport in the GDL • Empirical relationships for liquid water transport via capillary pressure
Main conclusions	• Liquid water accumulation is more pronounced in the regions of the GDL under the shoulders. • A large number of shoulders of smaller width is preferable. • Performance increases as the GDL thickness decreases
Limits	• Down the channel effects are neglected. • The porosity of the GDL is assumed constant as is thickness, even under the shoulders. • The relation used for capillary dependence on saturation is semi-empirical.

Jaouen, Lindbergh, and Sundholm [9] present a model of the cathode GDL and catalyst layer that is based on an agglomerate catalyst structure (Table 2.9). In their work, they assume spherical agglomerates and develop an effective reaction rate coefficient, based on diffusion through a spherical structure, which is used to account for the diffusive resistance that the reactants experience when diffusing through the polymer encapsulated agglomerates. The authors present results showing performance effects related to oxygen diffusion both through the agglomerates and the pores in the catalyst and GDL, proton conduction in the catalyst layer, and the kinetics of the oxygen reduction reaction. They find that the Tafel slope doubles when either transport limitation of protons or oxygen through the agglomerates is significant and quadruples in regimes where both are present. The modeling results also indicate that the change in Tafel slope disappears when gas transport limitations in the GDL become significant. This model can be used to generate qualitative results for some of the factors limiting cathode performance. It is one-dimensional and does not include water transport through the polymer or in the liquid phase through the pores of the catalyst layer and GDL.

Table 2.9 Jaouen, Lindbergh, and Sundholm (2002)

Model	Investigation of Mass-Transport Limitations in the Solid Polymer Fuel Cell Cathode (2002)
Authors	Jaouen, Lindbergh, and Sundholm [9]
Regions	• Cathode GDL and catalyst layer
Dimensionality	• One – through the thickness
Assumptions	• Steady • Incompressible • Isothermal • Uniform gas pressure over the electrode geometric area • Agglomerate catalyst structure
Phenomena investigated	• Gas transport in the catalyst layer • Gas transport in the GDL • Effect of ionic conductivity
Main conclusions	• Changes in the Tafel slope are related to kinetics, oxygen diffusion through the agglomerate, and proton transport.
Limits	• Liquid water effects that would affect gas transport are neglected.

In an extension of their previous work [8], Natarajan and Nguyen [10] present a pseudo three-dimensional model for water transport in the cathode GDL (Table 2.10). To capture transport effects that occur in the flow direction, the authors solve their two-dimensional model in succession, with each new solution using boundary conditions generated by the previous solution. The authors adjust their previously developed constitutive relation for the variation of capillary pressure with saturation and show a comparison illustrating how the modeling results change. The work includes parametric studies showing the effects of stoichiometry, relative humidity, and temperature on cell performance. In addition, the authors present plots showing the variation of current density in the flow direction. The model results also show the influence of the flowfield shoulder on water accumulation. Since the model is not truly three-dimensional, it does not accurately

capture transport processes that have significant components in the flow direction, i.e. transport of species in the gas channel. In addition, the membrane is not included nor is the catalyst layer.

Table 2.10 Natarajan and Van Nguyen (2003).

Model	**Three-Dimensional Effects of Liquid Water Flooding in the Cathode of a PEM Fuel Cell (2003)**
Authors	Natarajan and Van Nguyen [10]
Regions	• Gas channel, gas diffusion layer (cathode only) • Catalyst layer as an interface
Dimensionality	• Two are solved – through the thickness and across the channel • The down the channel solution is generated by successive solutions of the 2D model.
Assumptions	• Transient • Two-phase • Multi-component • Isobaric • Water transport by capillary pressure only – no advection
Phenomena investigated	• Performance effects related to liquid water transport in a cell with a conventional gas distributor • Effect of changes in species concentration down the channel
Main conclusions	• Down the channel effects, such as decreased reactant concentration, have a significant influence on cell performance. • Performance of the cathode decreases with increasing inlet humidity • The liquid water transport mechanism is the slowest and most dominant effect on performance at the cathode.

Limits	• The momentum equation is not solved in the gas channel. • The gas species and liquid water equations are not explicitly solved in the gas channel.

Genevey et al. [11] presents a comprehensive model of the cathode catalyst layer. The model is based on an agglomerate catalyst layer structure and includes the transport of thermal energy, gas species, liquid water, and charge (Table 2.11). In addition, the model is transient and can be used to illustrate how the various transport processes occurring within the catalyst layer behave over time. The authors present results showing how catalyst layer structural properties, porosity and reaction surface area in particular, affect performance. In addition, they present modeling results dealing with performance effects related to cathode temperature and flooding with liquid water. The model requires careful specification of boundary conditions on both the membrane and GDL boundaries (neither of which are included in the model). In addition, it is necessary to specify a limiting cell current density.

Table 2.11 Genevey et al. (2003)

Model	**Transient Model of Heat, Mass, and Charge Transfer as Well as Electrochemistry in the Cathode Catalyst Layer of a PEMFC (2002)**
Authors	Genevey, von Spakovsky, Ellis, Nelson, Olsommer, Topin, and Siegel [11]
Regions	• Cathode catalyst layer
Dimensionality	• One – through the thickness
Assumptions	• Transient • Isotropic and homogenous • One-dimensional • Polymer water content data at 30 C applies at 80 C

Phenomena investigated	• Effect of catalyst layer porosity on oxygen transport, current production, and overall performance • Influence of cell temperature on catalyst layer performance • Transport effects associated with the presence of liquid water within the porous catalyst layer • The transient behavior of the transport processes associated with oxygen, liquid water, and thermal energy
Main conclusions	• An increase in the cell operating temperature leads to a decrease in the performance of the catalyst layer. • Large values of liquid water saturation lead to non-uniform current production across the catalyst layer and a decrease in overall catalyst utilization.
Limits	• The model requires the specification of a limiting current based solely on oxygen diffusion through the cathode catalyst layer. • Performance effects related to the occlusion of the reaction sites within the catalyst layer by liquid water are not included.

2.2 Complete cell models

Bernardi and Vebrugge [12] present a one-dimensional model for transport within the fuel cell electrode (catalyst and GDL) and the membrane (Table 2.12). Their results focus on the transport of reactants and liquid water within the polymer itself as well as transport of reactants in the gas phase. The authors present results showing the distribution of reactants within the catalyst layers (the pores of which are assumed to be filled with polymer – pseudohomogenous structure) and the membrane. For high current densities, reactants are consumed completely within the first few microns of the 10 micron thick catalyst layers. This, the authors state, indicates that catalyst utilization is poor. Water transport across the membrane and catalyst layers is a function of electro-osmotic drag and applied pressure

difference. The modeling results show that for an applied pressure difference of 2 atm, electro-osmotic drag can be offset for a current density of less than 0.6 A/cm^2. In addition, the model is also used to illustrate the effect of GDL porosity on performance. Severe mass transport limitations are predicted for GDL porosities less than 20%. The model is well suited to simulating cell performance in regimes where mass transport limitations are not significant. In the regime where mass transport effects begin to dominate performance, the model does not agree well with experimental data. This is likely due to the fact that liquid water transport is not included in the model and to the assumption that reactants are transported only in dissolved form within the catalyst, as opposed to having a gas diffusion pathway.

Table 2.12 Bernardi and Verbrugge (1992).

Model	**A Mathematical Model of the Solid-Polymer Electrolyte Fuel Cell (1992)**
Authors	Bernardi and Verbrugge [12]
Regions	• Gas diffusion layers, catalyst layers, membrane
Dimensionality	• One – through the thickness
Assumptions	• Steady • Isothermal • Pseudo-homogenous catalyst layer
Phenomena investigated	• Water management and the effect of membrane hydration on performance • Fuel and oxidant crossover • Cell performance using Nafion® and Dow® membranes
Main conclusions	• Pore volume fraction in the GDL and catalyst layer should exceed 20%. • GDL hydraulic permeability should be low enough to maintain sufficient water to insure adequate membrane hydration. • Crossover effects are insignificant for current densities greater than 10ma/cm^2.

Limits	• Down the channel effects are neglected. • Cannot model mass transport limitations due to liquid water production.

The two-dimensional model presented by Gurau, Liu, and Kakac [13] includes all of the components of a PEMFC, with the exception of the current collectors, and is solved down the channel (Table 2.13). The solution space is segmented into three domains that must be solved separately and coupled to one another through an iterative technique. The catalyst layers are modeled as interfaces where mass transport is concerned and as volumes for the transport of protons and the calculation of the cell current. An effective gas diffusion coefficient is used in the gas species equations as a simplification to the Stefan-Maxwell equations. The diffusion coefficient is a function of the individual concentrations of the constituents of the multi-component flow. The authors present results showing how the model compares with experimental data. The comparison does not extend to the mass-transport limited regime which indicates that the model may not adequately handle mass transport effects. Additional results include parametric studies showing performance effects related to gas diffusion layer porosity, stoichiometry, and cell temperature. Contour plots of oxygen and water vapor mole fraction in the cathode gas channel and GDL are also presented. Results for liquid water velocity within the membrane are given at different current densities. The results do not include transport or water uptake and release within the catalyst layer. The principle limitations of this work are the absence of liquid water transport and the treatment of the catalyst layers as interfaces with respect to gas transport and dissolved water transport.

Table 2.13 Gurau, Liu, and Kakac (1998).

Model	**Two-Dimensional Model for Proton Exchange Membrane Fuel Cells (1998)**
Authors	Gurau, Liu, and Kakac [13]
Regions	• Gas channels, gas diffusion layers, catalyst layers (interfaces), membrane

Dimensionality	• Two – through the thickness and down the channel
Assumptions	• Steady • Laminar flow • Incompressible • Perfect gases • Liquid water volume in the gas channels is negligible. • Porous sections are isotropic. • The catalyst layers are interfaces • Reversible heat production is neglected.
Phenomena investigated	• Porosity of the GDL • Oxygen transport • Water transport through the membrane
Main conclusions	• The oxygen mole fraction distribution down the channel is non-linear • The current density distribution down the channel is non-linear
Limits	• Transport effects related to water buildup are neglected. • The transport of gases and dissolved water in the catalyst layer is neglected.

Yi and Nguyen [14] present a two-dimensional, down the channel model (Table 2.14). The authors are primarily concerned with investigating thermal and water management within the cell and include the transport of water within the gas phase in the gas channels as well as water transport through the polymer membrane. The equation for water transport through the membrane includes terms for diffusion, electro-osmotic drag, and convection via externally applied pressure difference. The authors present results for the partial pressure of water in the gas channel subject to different inlet conditions. These results show a decrease in the partial pressure of water on the anode due to water transport through the membrane to the cathode. Additional results show that this can be offset by an applied pressure difference. The authors also present results showing the effect of temperature on

cell performance and explore various options for cooling the collector plates in order to maintain a desired cell temperature. They find that the most effective way to regulate cell temperature is with a counterflow heat exchanger. The principal limitation of the model is the omission of the catalyst layers, which are important with regard to the transport of water within the polymer.

Table 2.14 Yi and Nguyen (1998)

Model	**An Along-the-channel Model for Proton Exchange Membrane Fuel Cells (1998)**
Authors	Yi and Nguyen [14]
Regions	• Gas channels, current collectors, membrane
Dimensionality	• Two – through the thickness and down the channel
Assumptions	• Steady • Laminar flow • Incompressible • Gas transport resistance is neglected in GDL and catalyst layers • Drag and water diffusion coefficient are determined by anode vapor activity. • Catalyst and GDL are interfaces
Phenomena investigated	• Water transport in the gas channels and membrane • Temperature distribution down the channel • Membrane water transport effects related to an applied pressure gradient

Main conclusions	• Humidification of the anode gas is required for best performance. • An applied pressure gradient can be used to offset anode dehydration due to electro-osmotic drag. • Running the reactants counterflow produces a more uniform temperature distribution than does parallel flow.
Limits	• The treatment of the GDLs and catalyst layers as interfaces makes it impossible to accurately simulate performance, especially at high current densities. • Using the anode vapor activity to set the water content throughout the entire membrane leads to an underestimation of the amount of water in the membrane.

Um, Wang, and Chen [15] present a two dimensional, single domain model for a PEMFC that includes the transport of gas species, momentum, and protons in a down the channel geometry (Table 2.15). The use of a single computational domain requires that all of the modeling equations are solved over the entire domain, even in regions where they are not physically valid. For instance, the equation for ionic potential is solved in the gas channels where ion transport does not occur. The advantage to the single domain approach is that it does not require the specification of interface conditions between computational domains. The authors present a performance comparison between modeling results and experimental data that does not extend into the mass transport limited regime. Additional results show current density distribution down the channel as well as contour plots of species concentration in the anode and cathode. The model is based on the assumption that the pores in the catalyst layers are filled with polymer. A novel approach is used to account for the concentration discontinuity between the GDL and the catalyst layer which results from gaseous reactants dissolving in the polymer filled catalyst layer as described by Henry's law. The model does not include liquid water transport and, although it does include the transport of water through the catalyst layer and the membrane, it is not clear how water uptake and release is handled.

Table 2.15 Um, Wang, and Chen (2000).

Model	**Computational Fluid Dynamics Modeling of Proton Exchange Membrane Fuel Cells (2000)**
Authors	Um, Wang, and Chen [15]
Regions	• Gas channels, GDLs, catalyst layers, membrane
Dimensionality	• Two – through the thickness and down the channel
Assumptions	• Transient • Laminar flow • Incompressible • Isothermal • Negligible ohmic drop in the electrically conductive regions • The catalyst is pseudohomogenous
Phenomena investigated	• Hydrogen dilution effects • Transient current response to a step change in voltage • Reactant transport in the polymer region of the catalyst and in the membrane
Main conclusions	• Hydrogen dilution depresses current density.
Limits	• Liquid water effects are neglected.

Dutta, Shimpalee, and Van Zee [16], present a three dimensional model of a PEMFC with a serpentine flowfield (Table 2.16). The model includes the transport of mass, momentum, gas species, and water within the polymer membrane. The catalyst layers are modeled as interfaces between the GDL and membrane at which point various source terms are applied to account for production and consumption of reactants. Liquid water transport is neglected. The results include a series of plots showing the velocity and density distribution within the gas channels and GDL. In addition, results are presented that show the variation of hydrogen consumption and water production across the surface of the MEA. Results for pressure drop show that, due to flow crossover from one channel to the next via the GDL, the drop in pressure along the serpentine flowfield is less than would be expected for laminar flow through the gas channel alone.

Table 2.16 Dutta, Shimpalee, and Van Zee (2001).

Model	Numerical Prediction of Mass-Exchange Between Cathode and Anode Channels in a PEM Fuel Cell (2001)
Authors	Dutta, Shimpalee, and Van Zee [16]
Regions	• Gas channels, GDL's, membrane
Dimensionality	• Three
Assumptions	• Steady • Laminar flow • Incompressible • Isothermal • The catalyst layer is an interface.
Phenomena investigated	• Effect of inlet humidity on performance • Distribution of species sources throughout the serpentine flowfield • Pressure drop for serpentine flow field
Main conclusions	• The flow directions of reactants within the porous media are dependent on mass consumption patterns. • Flow through the GDL is significant, leading to a lower than expected pressure drop.
Limits	• No liquid water effects. • Catalyst layer transport is neglected.

Siegel et al. [17] present a two-dimensional model based on an agglomerate catalyst structure (Table 2.17). The model is solved down the channel and includes all of the fuel cell components with the exception of the collector plates. The model of Siegel et al. is similar in many respects to the work presented in this dissertation. Transport equations are included for mass, momentum, species, protons, energy, and water within the polymer portions of the catalyst layers and the membrane. The treatment of water transport in the polymer phase is unique in that, since the catalyst layers are treated as volumes rather than interfaces, water uptake and release must be included. The authors present experimental data in the form of

SEM and TEM images that were used for physical property characterization as well as to justify the assumption of an agglomerate catalyst layer structure. The modeling results show that, for a given voltage, there is an optimal catalyst layer porosity required to maximize the amount of current produced. A porosity larger than this optimal value results in an increase in ohmic losses while less porosity leads to more mass transport losses. Results showing the influence of agglomerate size on performance are also presented and indicate that minimizing the size of the agglomerates leads to better performance due to a reduction in mass transport limitations. The model is limited in that it does not include liquid water transport. In addition, the limiting current is based on the thickness of the polymer coating surrounding each agglomerate, which is not known to a high degree of certainty.

Table 2.17 Siegel et al. (2003).

Model	**Single Domain PEMFC Model Based on Agglomerate Catalyst Geometry (2003)**
Authors	Siegel, Ellis, Nelson, and von Spakovsky [17]
Regions	• Gas channels, gas diffusers, catalyst layers, membrane
Dimensionality	• Two – through the thickness and down the channel
Assumptions	• Steady • Laminar flow • Incompressible • Ideal gases • Liquid water transport is neglected. • Agglomerate catalyst structure
Phenomena investigated	• Physical structure of the catalyst layer • Effect of catalyst layer porosity on performance • Effect of agglomerate size on performance • Oxygen transport in the cathode

Main conclusions	• Scanning electron microscopy is a useful tool for a physical characterization of the catalyst layer. • An optimal catalyst layer void fraction can be calculated for a given operating voltage. • Agglomerates larger than 0.5 microns in radius decrease cell performance.
Limits	• Model does not include liquid water transport

An improved model by Siegel et al. [18], that is very similar to the model detailed in Table 2.17, has recently been accepted for publication. This model includes revisions to mathematical formulation in [17] with regard to the treatment of the agglomerate structure. In addition, the improved model also includes liquid water transport within the porous catalyst layers and gas diffusion layers.

2.3 Physical property characterization

All computational fuel cell models, particularly those including the catalyst layers, require the specification of certain physical properties. Accurate specification of these properties is directly related to both the accuracy and utility of a given model. In many cases, it is possible to find empirical data for the required properties in the literature. Parthasarathy et al. [19] present experimental results for many of the kinetic and mass transport parameters required for modeling the oxygen reduction reaction at the fuel cell cathode (Table 2.18). The authors use a microelectrode, consisting of a thin platinum wire encased in Nafion®, to simulate the catalyst layer of a proton exchange membrane fuel cell. They present results for the Tafel slope, exchange current density, transfer coefficient, open circuit voltage, and solubility and diffusivity of oxygen in Nafion® for temperatures ranging from 30 C to 80 C. The tests were conducted with an applied oxygen pressure of 5 atm. The results for exchange current density show an increase in magnitude with temperature as well as with operating current. At low currents, there is an oxide layer present on the catalyst that reduces the exchange current density, this oxide layer is not present at high currents. The

transfer coefficient also increases with temperature as does the open circuit voltage. The solubility of oxygen in Nafion® decreases with temperature while the diffusion coefficient increases. Unfortunately, the work does not include results showing how the solubility varies with local gas pressure and polymer water content. The former is required to calculate the coefficient for Henry's law. The latter is useful in modeling reactant transport in the catalyst layer at high current density, when electro-osmotic drag creates a gradient in water content across the MEA.

Table 2.18 Parthasarathy et al. (1992).

	Temperature Dependence of the Electrode Kinetics of Oxygen Reduction at the Platinum/Nafion® Interface – A Microelectrode Investigation (1992)
Authors	Parthasarathy, Srinivasan, Appleby, and Martin [19]
Phenomena investigated	• Variation of kinetic parameters (exchange current density, Tafel slope, transfer coefficient) for oxygen reduction with temperature • Variation of open circuit potential with temperature • Solubility and diffusivity of oxygen in Nafion® as a function of temperature
Main conclusions	• The exchange current density varies with operating current density due to the presence of an oxide layer on the platinum at low current densities. • Oxygen diffusion in Nafion® increases with temperature while solubility decreases. • Transfer coefficient, exchange current density, and the open circuit voltage increase with temperature.

Zawodzinski et al. [20] present an experimental study of water uptake and transport in Nafion® 117 membranes and include comparisons with other types of ion exchange membranes (Table 2.19). The results presented in this work are similar to those presented in Springer et al. [1]. The authors show that Nafion® 117 achieves a maximum water content of

14 H_2O/SO_3^- when in equilibrium with a saturated vapor at 30 C and a maximum water content of 22 when immersed in liquid water at the same temperature (following pre-treatment by boiling). The diffusion coefficient and ionic conductivity are also given as a function of membrane water content. In addition, the ionic conductivity of a fully immersed membrane is presented as a function of temperature as is data related to electro-osmotic drag. A Dow XUS membrane was also evaluated in this work and was found to have a somewhat higher ionic conductivity than the Nafion® membrane.

Table 2.19 Zawodzinski et al. (1993).

	A Comparative Study of Water Uptake by and Transport Through Ionomeric Fuel Cell Membranes (1993)
Authors	Zawodzinski, Springer, Davey, Jestel, Lopez, Valerio, and Gottesfeld [20]
Phenomena investigated	• Membrane water content at equilibrium as a function of vapor activity and temperature • Variation of ionic conductivity with water content • Variation of the water diffusion coefficient with water content • Evaluation of the electro-osmotic drag coefficient
Main conclusions	• Comparison of Nafion® 117 to the Dow membrane showed that the Dow membrane had more water uptake per sulfonic acid group, a higher water diffusion coefficient, and a higher ionic conductivity.

Springer et al. [21] present impedance spectra for a PEMFC cathode from which information about losses associated with charge and mass transfer can be inferred (Table 2.20). The authors create a model of the transport of reactant species and protons within the cathode (GDL and catalyst layer) which is used to match physical causes to the observed trends in the impedance spectra. The results indicate that, at medium current density, proton conduction in the catalyst layer contributes significantly to cell impedance. At higher current density, mass transport limitations due to resistance to gas flow in the GDL become

significant. The tortuosity, which is the square of the ratio of effective tortuous path length to layer thickness, may be an important contributor to mass transport limitations in the GDL. This is in contrast to the belief that the porosity is more important in determining mass transport losses in the porous GDL. The results also show that insufficient cell humidification has a detrimental effect on electrocatalysis as well as on the conductivity of both the catalyst layer and the membrane.

Table 2.20 Springer et al. (1996).

	Impedance spectroscopy (1996)
Authors	Springer, Zawodzinski, Wilson, and Gottesfeld [21]
Phenomena investigated	• Used AC impedance spectroscopy to isolate some of the principal losses in a fuel cell • Investigate the effect of the gas diffusion layer on mass transport limitations • Investigate the effect of charge transfer in the catalyst layer
Main conclusions	• Charge and mass transfer effects in the catalyst layer contribute to impedance in the medium current density range. • The gas diffusion layer makes a large contribution to mass transfer limitations at high current density. • The tortuosity of the gas diffusion layer is important. The Bruggeman correction does not adequately explain observed phenomena. • Cell humidification affects protonic conductivity in the catalyst as well as the membrane and is also shown to influence electrocatalysis.

Zhang, Ma, and Muckerjee [22] present a microelectrode study in which they compare kinetic and mass transfer parameters for electrodes incorporating, in one case,

Nafion® as the ion conducting polymer, and in the other SPES-40, which is a different polymer capable of operation at higher temperatures (Table 2.21). The experimental procedure is very similar to the work of Parthasarathy et al. [19] with the exception that the tests are performed at 1 atm of oxygen pressure as opposed to 5 atm. The results for the kinetic parameters, exchange current density and transfer coefficient, are given over temperatures ranging from 30 C– 70 C. The values presented for both of these kinetic parameters are lower in magnitude than those presented in Parthasarathy et al. This could be because the lower oxygen pressure at which the tests were conducted led to decreased electrocatalysis. The results for the mass transport parameters, solubility and the diffusion coefficient of oxygen in Nafion®, are nearly the same as those given in Parthasarathy et al. There is some discrepancy, probably attributable to experimental error. It is interesting to note that the values for the dissolved oxygen concentration in Nafion® at 5 atm and at 1 atm of gas pressure are nearly identical over the range of temperature for which results are presented. This indicates that the data for oxygen solubility in Nafion® presented in both Zhang et al. and Parthasarathy et al. may not be sufficient for an accurate determination of Henry's constant. This will be discussed in detail in Section 4.

Table 2.21 Zhang et al. (2002).

	Oxygen Permeation Studies on Alternative Proton Exchange Membranes Designed for Elevated Temperature Operation (2002)
Authors	Zhang, Ma, and Mukerjee [22]
Phenomena investigated	• Evaluation of kinetic parameters for oxygen reduction (exchange current density, Tafel slope, transfer coefficient) in a Nafion® electrode and in an SPES-40 electrode • Evaluation of mass transport parameters (oxygen solubility, oxygen diffusion coefficient) in both types of polymers as a function of temperature • Comparison of water uptake characteristics of both polymers

Main conclusions	• Tafel plots display two slopes, corresponding to oxide - covered and oxide-free Pt. • The oxygen diffusion coefficient increases with temperature and solubility decreases. • Oxygen solubility was considerably lower in the SPES electrode.

Wang et al. [23] present experimental results for fuel cell performance under a range of operating conditions (Table 2.22). Their results, which consist of a series of polarization curves, show the influence of backpressure, cell temperature, and humidification on performance. One of the most interesting results indicates that the amount of humidification, at either the anode or cathode, has more influence on mass transport and activation losses than it does on ohmic losses. As humidity is decreased, the activation losses increase due to reduced ion mobility which translates into a reduction of the active catalyst area. Conversely, the limiting current increases as humidity is decreased and the reactant streams contain a larger fraction of either oxygen or hydrogen, relative to water vapor. The authors compare a previously developed computational model to the experimental data. The comparison is good in the activation and ohmic regimes, for the cases presented, but not in the mass transport limited regime. The disparity probably results from the omission of liquid water transport in the model.

Table 2.22 Wang et al. (2002).

	A Parametric Study of PEM Fuel Cell Performance (2002)
Authors	Wang, Husar, Zhou, and Liu [23]
Investigated phenomena	• Performance curves for a PEM test cell to show the effects of cell temperature, inlet humidity, and backpressure

Main conclusions	• Running the cell at low humidity causes the electrode to dehydrate, thus reducing the surface area available to electrochemical reactions. This leads to increased activation losses, particularly at low current density. The overall effect on performance is small. • The limiting current drops when humidification is increased due to flooding • Performance increases with backpressure due to increased exchange current density and reactant concentration.

Russell and Ellis [24] present experimental work showing the relationship between catalyst layer composition and PEMFC performance (Table 2.23). The authors fabricate and test a series of MEA's of varying composition with regard to the volume fraction of polymer, carbon support, and pores. They find that the best performance is achieved with a polymer loading (Nafion® in this case) of 33% by weight. In addition, they establish that the amount of carbon support is important independent of catalyst loading. The authors find that a carbon support loading of 1.3 mg/cm^3 gives the best performance. The porosity and thickness of the catalyst layer are also shown to affect performance.

Table 2.23 Russell and Ellis (2003).

	Experimental Investigation of the Effects of Catalyst Layer Composition on the Performance of Proton Exchange Membrane Fuel Cells (2003)
Authors	Russell and Ellis [24]
Investigated phenomena	• Show how fuel cell performance changes due to variations in the composition of the catalyst layer with regard to polymer and carbon loading as well as porosity and catalyst layer thickness

Main conclusions	• The optimum amount of polymer within the catalyst layer is 33% by weight. • A carbon support loading, independent of Pt catalyst loading, of 1.3 mg/cm^3 results in the best cell performance at 0.5 V. • Catalyst layer thickness and porosity influence performance due to their importance with regard to the transport of gaseous reactants and liquid water as well as the conduction of protons and electrons.

Ihonen et al. [25] present a detailed experimental analysis of the structure of the catalyst layer as well as cell polarization curves (Table 2.24). The authors fabricate MEA's and use mercury and gas porosimetry to determine the porosity and pore size distribution both for the catalyst layer and for the carbon supported catalyst itself. Their findings indicate that the carbon support contains small pores (~10 nm), but that these pores are either filled or covered with polymer when the catalyst layer is assembled. In addition, they present results for the size of the agglomerates in the catalyst layer. The polarization curves are presented to illustrate the change in kinetics as current density is increased. It is evident that the Tafel slope changes, doubling or even quadrupling, depending on operating conditions. The change in slope is related to a variety of different factors which are presented in another paper by the same authors [9] that uses a computational model to relate the experimental results to physical phenomena.

Table 2.24 Ihonen et al. (2002).

	Investigation of Mass-Transport Limitations in the Solid Polymer Fuel Cell Cathode (2002)
Authors	Ihonen, Jaouen, Lindbergh, Lundblad, and Sundholm [25]

Phenomena investigated	• Used an SEM to image the catalyst layer. Performed BET and Hg porosimmetry on the catalyst layer to determine pore size, pore size distribution, porosity, and agglomerate size. • Performed cell testing to investigate oxygen reduction kinetics at the cathode, with particular attention given to the change in Tafel slope. • Investigated the effect on performance of active layer thickness, total pressure, humidity, and oxygen mole fraction
Main conclusions	• The carbon support contains 10nm pores – which are smaller than those observed in the complete catalyst layer. • The average agglomerate size is 210nm. • Change in the Tafel slope outside of the activation region can be related to oxygen diffusion in the agglomerates. • The catalyst is used equally through the thickness of the layer. On an agglomerate level, utilization is non-uniform as the catalyst around the surface of an agglomerate will be more readily used than that at its center.

2.4 Conclusion

When reading the existing fuel cell modeling literature, it becomes readily apparent that one thing that all of the computational models have in common is that the results which they produce are dependent on a series of assumptions. Typically, assumptions are made in such a manner as to not compromise the accuracy of the model. For instance, when one is modeling the specifics of the oxygen reduction reaction in the cathode catalyst layer, it is fair to assume that only transport effects in the direction through the layer thickness are important. However, many of the comprehensive models in the literature, which seek to accurately model the performance of the entire cell, include assumptions that prevent them

from doing this. Most notably, the fairly common assumptions that liquid water transport need not be included and that the catalyst layers may be treated as interfaces rather than as volumes greatly diminish the accuracy and utility of a model. In addition, comprehensive models should include transport along the flow direction in order to capture important effects such as reactant depletion and non-uniformities in current density and cell temperature.

Equally as important as including the necessary mathematics and dimensionality in a model is the use of the correct physical properties. For a given model, many of the physical properties that are required can be experimentally determined but some cannot. The properties that cannot be experimentally determined are typically treated as estimated properties, some of which are adjusted to bring the model results into agreement with experimental data. It follows then, that as the number of estimated properties increases, the accuracy of the model decreases. In addition, the uncertainty of an estimated property also influences the accuracy of the model. To state it concisely, any model can be improved by maximizing the number of properties that are experimentally determined and minimizing the range of uncertainty of the estimated properties.

The model presented in this dissertation improves on existing comprehensive models in that the formulation includes:

- All of the relevant transport equations, including liquid water and water dissolved in the polymer phase of the catalyst layers and the membrane
- All of the components of a fuel cell with both catalyst layers modeled as volumes as opposed to interfaces
- Two and three-dimensional geometries that allow for the modeling of transport through the cell thickness and along the flow direction

Most of the physical properties used in the formulation are taken directly from experimental data found in the literature and from measurements made as part of this work. For the few parameters which are not well established empirically, uncertainty in each parameter is limited in accordance with the data that is available in the literature.

3 The Mathematical Model

In this section, the transport equations, source terms, and closure relations on which the computational fuel cell model is based are presented. Since the model is solved over a single solution domain, each transport equation is solved in every component of the fuel cell model. However, the form of the equations can vary from component to component. For example, the momentum equations appear as the full Navier-Stokes equations for an incompressible fluid in the gas channels, and are reduced to the Darcy equations within the porous gas diffusion and catalyst layers. For this reason, the equations are presented in the context of the fuel cell component in which they are solved, e.g. the equations as they appear in the gas channels are presented in the first section. Along with the mathematical relations, a description of the physical form and function of each of the fuel cell components is also presented. The assumptions associated with the equations as they relate to a given component are discussed.

3.1 The Gas Channels

Reactants enter and exit the fuel cell by way of the gas channels. Generally, the channels are machined into the collector plates (bi-polar or mono-polar) but may also be fabricated by stamping or injection molding [26]. The flowfield itself, which is the entire network of gas channels, is designed in such a way as to uniformly distribute reactants across the surface of the GDL. Common flowfield designs consist of either serpentine or straight gas channels. Figure 3.1 shows an example of a flowfield with straight channels. Figure 3.2 shows the serpentine flowfield in the 5 cm^2 test cell that was used to generate experimental data for model validation, which is discussed in Section 6.

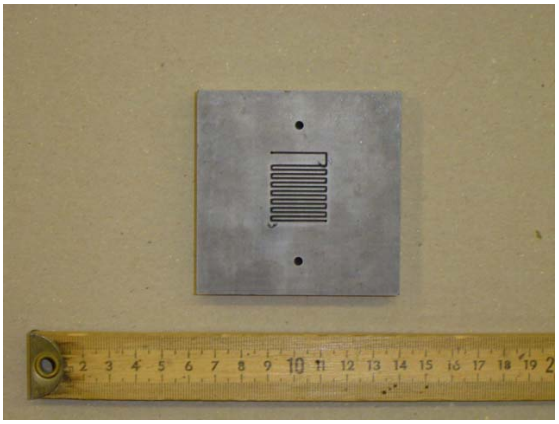

Figure 3.1 A flowfield with serpentine gas channels

Figure 3.2 A flowfield with straight gas channels

3.1.1 Model Assumptions

The following assumptions apply to the model when solved in the gas channels:

- Steady state
- Bends in the gas channels are neglected, and the flowfield on the anode and cathode sides is modeled as a straight channel.
- The gas flow is laminar and incompressible, but not constant density.
- The viscosity and thermal conductivity of the gas mixture are constant and calculated from the inlet conditions.

- Liquid water is transported by advection as small droplets moving at the same velocity as the gas flow.

3.1.2 Model equations

The conservation of mass equation is expressed as shown in Eq. (3.1a). The source term accounts for changes in the mass flux due to the evaporation or condensation of liquid water. The conservation of linear momentum in three dimensions takes the form of the Navier-Stokes equations for incompressible flow and is expressed as Eqs. (3.1 b-d)

$$\nabla \cdot \left(\rho^{g} \bar{u}\right) = S_{LV} \tag{3.1a}$$

$$\bar{u} \cdot \nabla\left[\rho^{g} u_{x}\right] = -\frac{\partial P}{\partial x} + \mu \nabla^{2} u_{x} \tag{3.1b}$$

$$\bar{u} \cdot \nabla\left[\rho^{g} u_{y}\right] = -\frac{\partial P}{\partial y} + \mu \nabla^{2} u_{y} \tag{3.1c}$$

$$\bar{u} \cdot \nabla\left[\rho^{g} u_{z}\right] = -\frac{\partial P}{\partial z} + \mu \nabla^{2} u_{z} \tag{3.1d}$$

The mixture density is calculated using the ideal gas law, Eq. (3.2), combined with the solutions to the local gas species equations. For both the anode and cathode sides of the cell, the number of species equations is one less than the number of species. At the anode, the species equation for water vapor is solved, Eq. (3.3). At the cathode, both the water vapor and oxygen, Eq. (3.4), species equations are solved. The hydrogen and nitrogen mass fractions, Eq. (3.5), are determined from the solutions to these species equations and the overall gas phase conservation equation, Eq. (3.1).

$$\rho^{g} = \frac{P}{RT \sum w_{j} / M_{j}} \tag{3.2}$$

$$\rho^{g} \bar{u} \cdot \nabla w_{WV} + w_{WV} \nabla \cdot \left(\rho^{g} \bar{u}\right) = \nabla \cdot \left(D_{WV}^{g} \rho^{g} \nabla w_{WV}\right) + S_{LV} \tag{3.3}$$

$$\rho^{g} \bar{u} \cdot \nabla w_{O2} + w_{O2} \nabla \cdot \left(\rho^{g} \bar{u}\right) = \nabla \cdot \left(D_{O2}^{g} \rho^{g} \nabla w_{O2}\right) \tag{3.4}$$

For N_2 and H_2

$$w_k = 1 - \sum_{j \neq k} w_j \tag{3.5}$$

The diffusion of each species within the bulk flow is given by the first term on the right side of Eqs. (3.3) and (3.4). The diffusion coefficients for multi-component flow, which are calculated from Eq. (3.6), are based on a simplification of the Stefan-Maxwell equations [13]. The binary diffusion coefficient for each of the mixture components is given by Eq. (3.7) [27]. Each of the species equations has a single advective term that is shown as two terms after expansion via the chain rule. The first is equal to the product of the velocity, mixture density, and mass fraction gradient and accounts for transport due to the motion of the bulk flow. The second term is the product of the mass fraction and the divergence of total mass flux. It represents the influence of the bulk concentration on the individual species mass fraction.

$$D_k^g = \frac{1 - y_k}{\sum_{j \neq k} \frac{y_j}{D_{jk}}} \tag{3.6}$$

$$D_{jk} = (P_j^c P_k^c)^{\frac{1}{3}} (T_j^c T_k^c)^{\frac{5}{12}} \left(\frac{1}{M_j} + \frac{1}{M_k} \right)^{\frac{1}{2}} a \left(\frac{T}{\sqrt{T_j^c T_k^c}} \right)^b \frac{101325}{P}$$

$$O_2 - N_2 : a = 2.745E^{-4}, b = 1.823 \tag{3.7}$$

$$O_2 - H_2O, N_2 - H_2O, H_2 - H_2O : a = 3.64E^{-4}, b = 2.334$$

Liquid water is assumed to be transported as droplets of negligible volume moving at the mass averaged velocity of the gas flow. The equation for liquid water transport is expressed as Eq. (3.8).

$$\bar{u} \cdot \nabla s = \nabla \cdot \left(D_{WL}^{cp} \nabla s \right) - S_{LV} / \rho_{WL} \tag{3.8}$$

The variable s is the liquid water saturation. It is expressed, within porous media, as the ratio of total liquid volume to total pore volume. Since the gas channel is non-porous, it is not possible to accurately calculate a liquid water distribution; Eq. (3.8) is solved simply as a

means of allowing liquid water to be removed from the solution domain in order to conserve mass. The mechanism of water removal is primarily advective. The diffusive term, which will be discussed in detail in the next section, allows water to move into the gas channel across the boundary with the GDL and is negligible in magnitude when compared to the advective term. The evaporation of liquid water is accounted for with the source term, S_{LV}, which is also used in the gas phase continuity and water species equations. Condensation is neglected in the gas channels. S_{LV} is expressed as Eq. (3.9a). The presence of the variable s prevents evaporation when there is no liquid water present.

$$S_{LV} = \psi s \gamma_{LV} \tag{3.9a}$$

$$\gamma_{LV} = (1.0 - 0.5(1.0 + \mathrm{Tanh}(C_1 * \frac{\rho_{WV}^{g}}{\rho_{SAT}^{g}} - C_2))) \tag{3.9b}$$

Equation (3.9a) allows for the evaporation of liquid water when the local relative humidity is less than 98%, and condensation when it is greater than 98%. The switch between evaporation and condensation is controlled by $\gamma_{LV,}$ given by Eq. (3.9b). When the local relative humidity is greater than 98%, Eq. (3.9b) has a value approaching zero, otherwise it approaches 1. The constants, C_1 and C_2, control the rate at which the switch changes between 0 and 1. The magnitude of the source term, with regard to either evaporation or condensation, is set by the mass transfer rate coefficient, ψ, which is chosen to be large enough to ensure local equilibrium between the vapor and liquid phases.

The equation for thermal energy transport is expressed as Eq. (3.10). The advective term is a function of the mass averaged gas velocity, mixture density, and effective specific heat given by Eq. (3.12). In addition, the advective term also accounts for energy transported by liquid water droplets entrained in the bulk fluid flow. The thermal conductivity is also an effective parameter and is expressed as Eq. (3.11). The mole fraction of the individual species can be calculated from the mass fraction and the mixture molecular weight as shown in Eq. (3.13). The last term in Eq. (3.10) is a source term that accounts for the energy transfer associated with the evaporation of liquid water.

$$(\rho^{g} c_{eff} + \rho_{WL} c_{WL} s)\bar{u} \cdot \nabla T = \nabla \cdot (k_{eff} \nabla T) - S_{LV} h_{fg} \tag{3.10}$$

$$k_{eff} = y_{O2}k_{O2} + y_{N2}k_{N2} + y^{g}_{H2O}k^{g}_{H2O} \quad \text{Cathode}$$
$$k_{eff} = y_{H2}k_{H2} + y^{g}_{H2O}k^{g}_{H2O} \quad \text{Anode} \tag{3.11}$$

$$c_{eff} = w_{O2}c_{O2} + w_{N2}c_{N2} + w^{g}_{H2O}c^{g}_{H2O} \quad \text{Cathode}$$
$$c_{eff} = w_{H2}c_{H2} + w^{g}_{H2O}c^{g}_{H2O} \quad \text{Anode} \tag{3.12}$$

$$y_k = w_k \frac{M_{mix}}{M_k} \tag{3.13}$$

The solutions to the equations for dissolved water and ionic charge transport are both forced to zero in the gas channels using a numerical method that is discussed in detail in Section 5.

3.1.3 Boundary Conditions and Initial Conditions

Boundary conditions are specified only at the inlets, outlets, and along the outer boundary of the gas channels as shown by the solid lines in Figure 3.3. The outer boundary of the membrane electrode assembly (gas diffusion layers, catalyst layers, and membrane), represented by a dashed line in Figure 3.3, is impermeable (zero flux) with respect to all transported quantities.

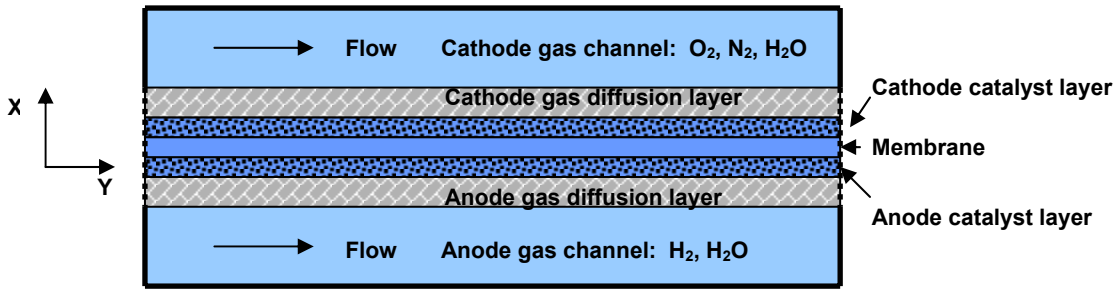

Figure 3.3 Boundaries of the gas channels.

Since the model is solved over a single solution domain, it is not necessary to specify conditions at any of the internal interfaces between the various components. Initial conditions, which may also be thought of as a starting solution, are specified at every point within the gas channels. The specification of initial conditions is required for some of the

governing equations to minimize numerical instabilities and also has the added benefit of decreasing the solution time. The boundary conditions and initial conditions for the governing equations as they pertain to the gas channels are shown in Table 3.1.

Table 3.1 Boundary conditions and initial conditions for the governing equations as solved in the gas channels.

Governing Equation	Anode Inlet	Anode Exit	Cathode Inlet	Cathode Exit	Sides	Initial Conditions
Mass	-	$P_{rel} = 0$	-	$P_{rel} = 0$	Flux = 0	-
Momentum	$u_{y,avg}$	Fully developed	$u_{y,avg}$	Fully developed	Flux = 0	-
Oxygen Transport	$\nabla \cdot w_{O2} = 0$	$\nabla \cdot w_{O2} = 0$	w_{O2}	$\nabla \cdot w_{O2} = 0$	Flux = 0	w_{O2}
Water Vapor Transport	w_{WV}	$\nabla \cdot w_{WV} = 0$	w_{WV}	$\nabla \cdot w_{WV} = 0$	Flux = 0	w_{WV}
Dissolved Water Transport[1]	$\nabla \cdot c^p_{WD} = 0$	$\nabla \cdot c^p_{WD} = 0$	$\nabla \cdot c^p_{WD} = 0$	$\nabla \cdot c^p_{WD} = 0$	Flux = 0	c^p_{WD}=0
Liquid Water Transport	$s = 0$	$\nabla \cdot s = 0$	$s = 0$	$\nabla \cdot s = 0$	Flux = 0	s =0
Ionic Potential[1]	$\nabla \cdot \phi_i = 0$	$\nabla \cdot \phi_i = 0$	$\nabla \cdot \phi_i = 0$	$\nabla \cdot \phi_i = 0$	Flux = 0	-
Energy	T_{cell}	-	T_{cell}	-	T_{cell}	T_{cell}

[1] Solution is set to zero in the gas channels.

3.2 The Gas Diffusion Layer

The gas diffusion layer (GDL) serves two purposes. The first is to uniformly distribute reactants across the surface of the catalyst layer while at the same time facilitating the removal of liquid water produced at the cathode. The second is to provide an electrical

connection between the shoulder of the collector plate and the catalyst layer. In general, the GDL is made of a porous material such as carbon cloth, carbon paper, or metal wire mesh. The porous nature of the GDL facilitates reactant distribution across the catalyst layer while the material itself is a good electrical conductor, providing a low resistance connection between the catalyst layer and the collector plate shoulders. The GDL material may be impregnated with a hydrophobic material, such as Teflon, to aid in liquid water removal. Figure 3.4 is an illustration of a typical GDL as it appears in a PEMFC between the collector plate and the catalyst layer.

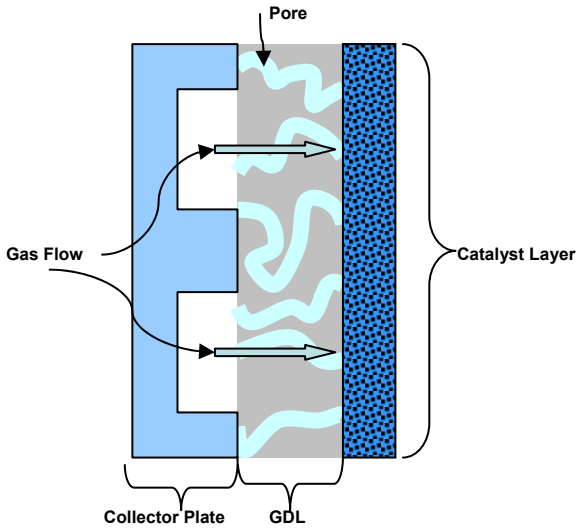

Figure 3.4 The gas diffusion layer (not to scale).

For the sake of simplicity, the GDL is represented as a block of material containing numerous pathways through which gaseous reactants and liquid water can pass. The physical characteristics of the GDL, such as the ratio of pore volume to total layer volume (porosity) and the square of the ratio of the average tortuous path length to the layer thickness (tortuosity), can have a significant impact on the transport of reactants as well as on overall cell performance [1,12,13].

Figure 3.5 is a micrograph of a carbon cloth GDL, and Figure 3.6 is a micrograph of a carbon paper GDL. The images were taken at a magnification of 200 X.

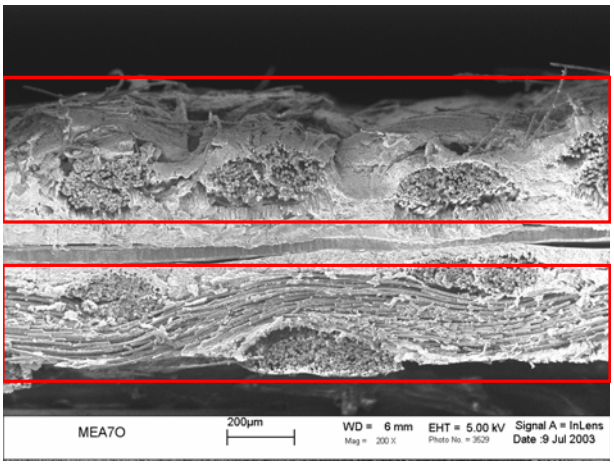

Figure 3.5 An SEM image of a carbon cloth GDL (outlined in red).

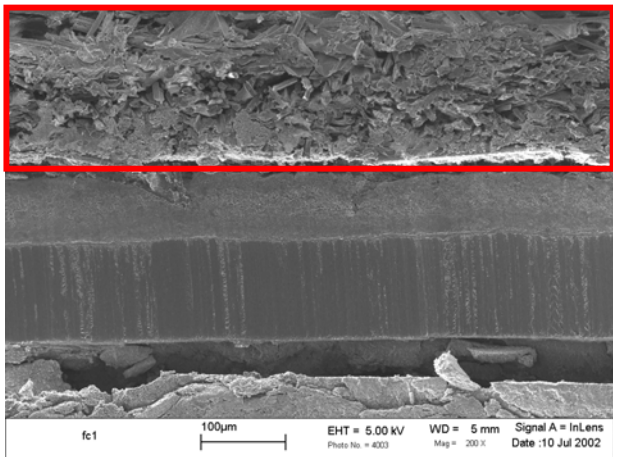

Figure 3.6 An SEM image of a carbon paper GDL (outlined in red).

Although the two materials look much different, the carbon paper GDL appearing more isotropic, both materials can be made to have similar properties with respect to electrical conductivity, porosity, and thickness. In addition, both can be treated to increase hydrophobicity.

One important difference between the two materials is that the carbon paper is more rigid than the cloth. When an individual fuel cell is assembled, a significant amount of clamping pressure is applied to achieve better contact between the individual components

and thereby minimize interface resistances. Due to its flexibility, the carbon cloth GDL will deform under applied pressure and, if the pressure is high enough, may bulge out into the gas channel and produce a restriction in the gas flow (the carbon paper GDL deforms much less). This is illustrated in Figure 3.7. In addition, the GDL will be crushed under the collector plate shoulders, leading to a decrease in porosity and possibly preventing reactants from reaching the portions of the catalyst layer directly under the shoulders.

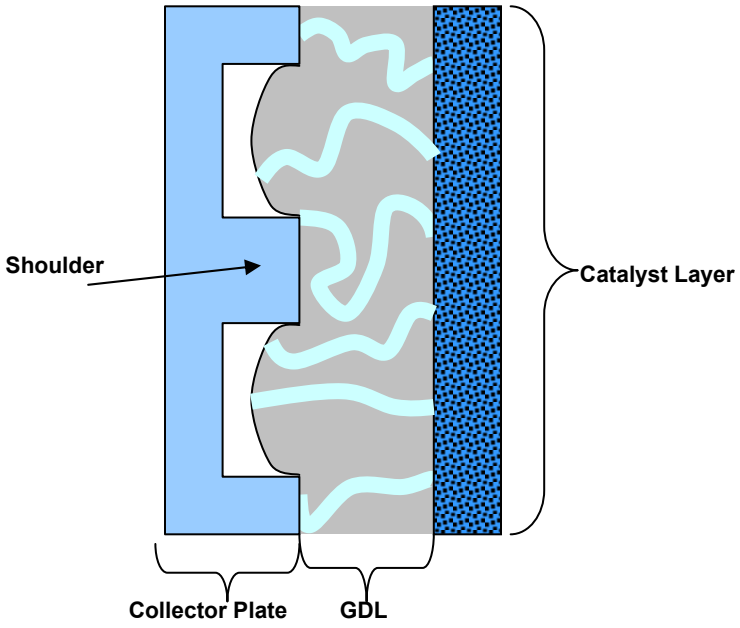

Figure 3.7 The GDL as assembled within the fuel cell.

3.2.1 Model Assumptions

The following assumptions apply to the model when solved in the gas diffusion layers:

- Steady state
- The gas diffusion media is isotropic, homogenous, and does not extend into the gas channels; the thickness and porosity of the GDL are set in a manner that accounts for GDL crushing under the shoulders of the collector plate.
- The momentum equations reduce to the Darcy equations.

- The gas flow is laminar and incompressible but not constant density.
- The viscosity of the gas mixture is constant and calculated from the inlet conditions.
- The thermal conductivity is based on the inlet gas species concentrations as well as the local liquid water saturation and is allowed to vary.
- Liquid water within the pores is transported by capillary flow.

3.2.2 Model equations

The conservation of mass equation is expressed as shown in Eq. (3.14a), which is identical to the form used in the gas channels. The conservation of linear momentum in three dimensions takes the form of the Darcy equation for flow in porous media, Eqs. (3.14b-d).

$$\nabla \cdot \left(\rho^{g} \overline{u}\right) = S_{LV} \tag{3.14a}$$

$$\frac{\partial P}{\partial x} = -\frac{\mu}{\kappa} u_{x} \tag{3.14b}$$

$$\frac{\partial P}{\partial y} = -\frac{\mu}{\kappa} u_{y} \tag{3.14c}$$

$$\frac{\partial P}{\partial z} = -\frac{\mu}{\kappa} u_{z} \tag{3.14d}$$

The species equations for the gas phase are expressed as Eqs. (3.15-3.16b). In the porous GDL, the diffusion coefficients for the individual species are modified to include terms to account for the effects of porosity, tortuosity, and liquid water accumulation on the diffusive flux, Eq. (3.17). An increase in saturation or in tortuosity or a decrease in porosity decreases the effective diffusivity of the gas phase.

$$\rho^{g} \overline{u} \cdot \nabla w_{WV} + w_{WV} \nabla \cdot \left(\rho^{g} \overline{u}\right) = \nabla \cdot \left(D_{WV}^{g} \rho^{g} \nabla w_{WV}\right) + S_{LV} \tag{3.15}$$

$$\rho^{g} \overline{u} \cdot \nabla w_{O2} + w_{O2} \nabla \cdot \left(\rho^{g} \overline{u}\right) = \nabla \cdot \left(D_{O2}^{g} \rho^{g} \nabla w_{O2}\right) \tag{3.16}$$

For H_2 and N_2:

$$w_k = 1 - \sum_{j \neq k} w_j \tag{3.16b}$$

$$D_k^g = \frac{1 - y_k}{\sum_{j \neq k} \frac{y_j}{D_{jk}}} \cdot \frac{\varepsilon_{gdl}(1 - s)}{\tau_{gdl}} \tag{3.17}$$

Liquid water is transported within the GDL via capillary flow as illustrated in Figure 3.8.

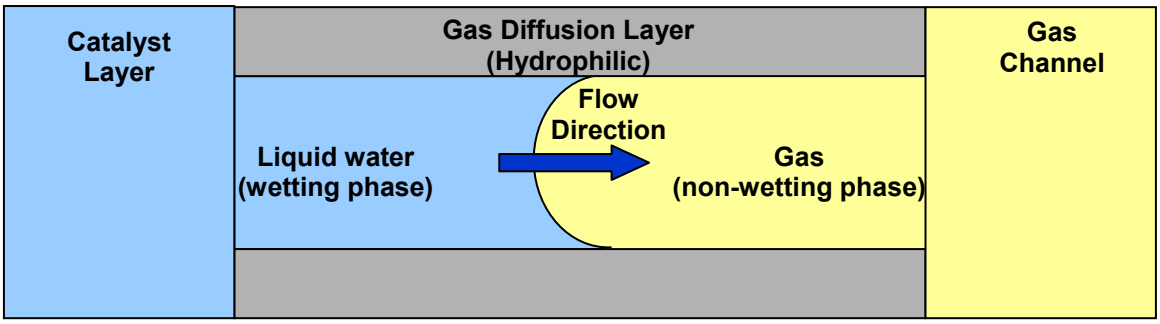

Figure 3.8 A single GDL pore showing the interface between the liquid and vapor phases.

As the pores in the GDL, which are assumed to be non-uniform in size, fill with water, a pressure difference between the liquid (wetting) and gaseous (non-wetting) phases is developed across a meniscus due to the interaction of the liquid with the solid pore wall. If the liquid wets the solid pore wall, as is assumed in this model, the pressure difference between the gas and liquid, i.e. the capillary pressure, causes the liquid to be pulled through the pores toward the non-wetting gas. Capillary pressure can be expressed as Eq. (3.22) and is a function of surface tension, Γ, and the mean radius of curvature, r_m, of the meniscus separating the gas and liquid phases [28].

$$P^c = P^g - P^L = 2\Gamma / r_m \tag{3.22}$$

The radius of curvature is related to, among other things, the pore size; for a given material, the radius of curvature decreases with pore size causing the capillary pressure to increase. It is generally accepted that when a material containing pores of different sizes, like the GDL, fills with liquid, the smallest pores fill first. If one was then to measure and

plot the capillary pressure within the pores as a function of liquid saturation, the resulting trend would look like that shown in Figure 3.9. At low values of saturation only the smallest pores have filled, leading to a large average value of capillary pressure. As saturation increases, the larger pores begin to fill and the average value of capillary pressure decreases.

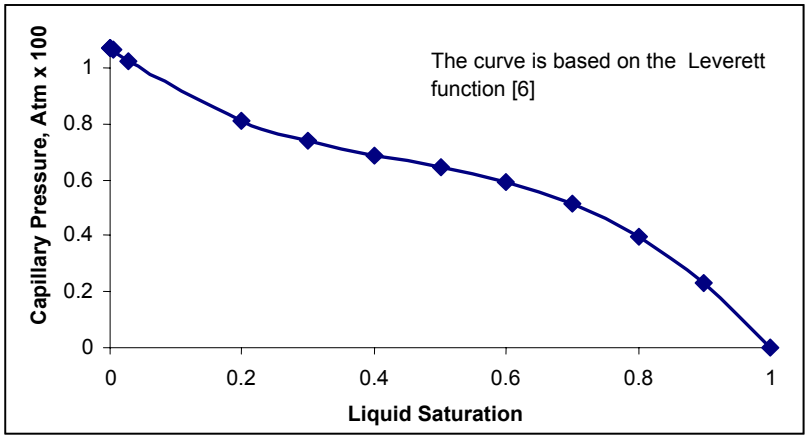

Figure 3.9 Capillary pressure predicted using the Leverett function.

Figure 3.9 was generated using a form of the Leverett function presented in the two-phase modeling work of Wang and Wang [6]. Like many functional relations describing the dependence of capillary pressure on saturation, the Leverett function is empirical and valid only for the materials used in the experiments from which it is generated. These materials are typically limited to sand, limestone, and other types of earth. A version of the Leverett function specific to the types of materials used in fuel cell gas diffusion media is not yet available.

The transport equation for liquid water used in this work is given in Eq. (3.23). The form of the liquid water diffusion coefficient, Eqs. (3.24a) and (3.24b), is based on results presented by Natarajan and Nguyen [8] for two phase flow in the gas diffusion layer. The source term, S_{LV}, accounts for mass exchange between the liquid and vapor phases and is given as Eq. (3.25). S_{LV} is discussed in detail in Section 3.4.

$$\nabla \cdot \left(D_{WL}^{cp} \nabla s \right) - S_{LV} / \rho_{WL} = 0 \tag{3.23}$$

$$D_{WL}^{cp} = \frac{\rho_{WL} g}{\mu_{WL}} K_L(s) \frac{\partial P_c}{\partial s} \tag{3.24a}$$

$$K_L(s)\frac{\partial P_c}{\partial s} = 0.0155s^3 - 0.0213s^2 + 0.0088s + 0.0002 \quad (3.24b)$$

$$S_{LV} = \psi s\gamma_{LV} - \psi(1-s)(1-\gamma_{LV}) \quad (3.25)$$

The principal difference between the Natarajan and Nguyen semi-empirical relationship for the dependence of capillary pressure on saturation and the empirical Leverett equation is that, over the range of saturation values, the capillary pressure determined by the former. is about two orders of magnitude smaller than that calculated using the Leverett equation. It is difficult to say what the cause of this discrepancy is, but it is probably related to the difference in the two materials for which the respective equations were determined. The Leverett function is based on a system of liquid water and sand, while the equation developed by Natarajan and Nguyen is based on fuel cell gas diffusion media, which may have much larger pores than a bed of packed sand thus leading to a lower overall capillary pressure over a range of saturation values.

Equation (3.23) does not contain an advective term since transport in the GDL is by capillary flow only. The source term and related switch function work the same way in the GDL as in the gas channel, with the exception that both evaporation and condensation are considered in the GDL. The diffusion coefficient was derived by assuming that the liquid velocity within the porous GDL can be calculated using the Darcy equation. This assumption requires that the flow velocity result from a pressure gradient, which in this case is the gradient of capillary pressure. Applying the chain rule to the capillary pressure gradient allows it to be written as the product of the derivative of capillary pressure with respect to saturation, as shown in Eq. (3.24a), and the derivative of saturation with respect to position. Using this definition, it is possible to represent the flow of liquid water as a diffusive process as indicated by Eq. (3.23). Figure 3.10 is a plot of Eq. (3.24b) for saturation values between 0 and 1. In fitting the model results to the experimental data, the procedure of Natarajan and Nguyen was followed; it was assumed that the shape of the curve shown in Figure 3.10 remained constant while the magnitude was allowed to vary. This amounts to changing the magnitude of the permeability of the GDL to liquid water, $K_L(s)$. Experimental data for the permeability of the GDL material is not currently available. For this reason it was thought that treating it as a fitting parameter was justified.

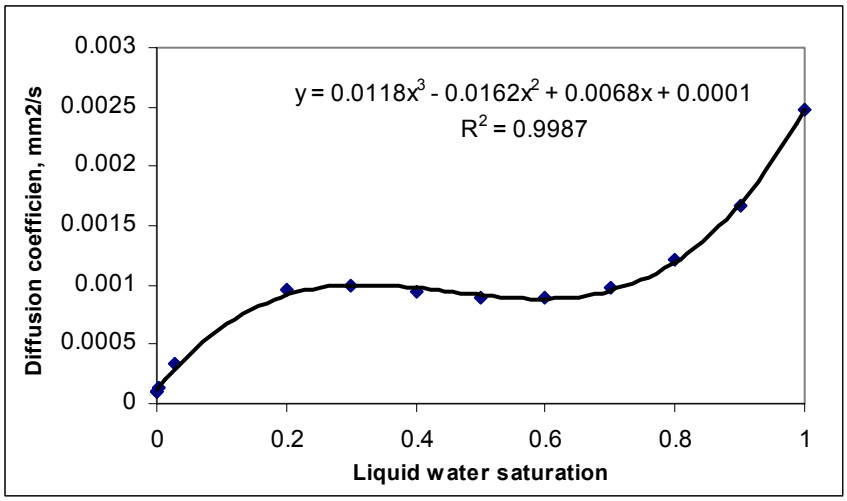

Figure 3.10 Diffusion coefficient for liquid water within the porous GDL based on the semi-empirical results presented by Natarajan and Nguyen [8]. The curve is based on fitting model results to experimental data.

The equation for thermal energy can have one of two forms, depending on whether the model is being solved in two dimensions or three. Eq. (3.26) is the form used for a three-dimensional model; Eq. (3.27) is for a two-dimensional model. Both equations include advective and diffusive terms accounting for energy transport via the gas phase as well as by liquid water. For a 2D geometry, the shoulders of the collector plates, which contact the GDL as shown in Figure 3.7 and provide a low resistance heat conduction pathway, are not explicitly included in the model. Instead, their effect on energy transport is included with a volumetric source term applied in the GDL. This term, Eq. (3.28), simulates the effect of the collector plate shoulders on energy transport by either adding heat to the cell or removing it depending on whether the cell temperature is lower or higher than the temperature at the external boundary of the collector plate. For a 3D geometry, the collector plate shoulders are explicitly included in the solution domain; an additional source term is unnecessary. The source term, S_{pc}, accounts for the energy associated with phase change.

$$(\rho^{g} c_{eff} \overline{u} + c_{WL} \rho_{WL} s \varepsilon_{gdl} D_{Wl}^{CP} \nabla s) \cdot \nabla T = \nabla \cdot (k_{eff} \nabla T) + S_{pc} \tag{3.26}$$

$$(\rho^{g} c_{eff} \overline{u} + c_{WL} \rho_{WL} s \varepsilon_{gdl} D_{Wl}^{CP} \nabla s) \cdot \nabla T = \nabla \cdot (k_{eff} \nabla T) + S_{pl} + S_{pc} \tag{3.27}$$

$$S_{pl} = \frac{(T_{pl} - T)}{t_{gdl}} \left(\frac{t_{gdl}}{k_{gdl}} + \frac{t_{pl}}{k_{pl}} \right)^{-1} \tag{3.28}$$

$$S_{pc} = -S_{LV} h_{fg}$$

The thermal conductivity of the GDL, Eq. (3.29a), includes contributions from the species in the gas phase, Eq. (3.29b), the solid carbon matrix, and the liquid water that may be present in the pores. The specific heat, Eq. (3.30a), includes contributions from liquid water and the gas species, Eq. (3.30b). The velocity of the liquid water in the GDL is assumed to be equal to that of the mass averaged gas velocity with respect to the convective term used in the energy equations.

$$k_{eff} = \varepsilon_{gdl}(1-s)k_g + \varepsilon_{gdl} s k_{WL} + (1-\varepsilon_{gdl})k_c \tag{3.29a}$$

$$k_g = \sum_k y_k^g k_k^g \tag{3.29b}$$

$$c_{eff} = c_g \varepsilon_{gdl}(1-s) + c_{WL} \varepsilon_{gdl} s \tag{3.30a}$$

$$c_g = \sum_k w_k^g c_k^g \tag{3.30b}$$

The transport equations for ionic charge as well as water dissolved in the polymer are solved in the GDL, but the diffusion coefficients of both equations are set to zero. This has the effect of imposing a zero flux condition for these equations at the interface between the GDL and catalyst layer as well as at the interface between the GDL and gas channel.

3.2.3 Boundary Conditions and Initial Conditions

As mentioned earlier, when solving the governing equations over a single solution domain, it is not necessary to specify interface conditions between the individual fuel cell components. For the GDL, only the boundaries on the dashed lines in Figure 3.11 require conditions to be specified. When solved in the GDL, all of the governing equations have zero flux conditions specified on these boundaries. In other words, no quantities are transported out of the solution domain through the GDL. Initial conditions are specified for the gas species only, and they are equal to those specified in the gas channels.

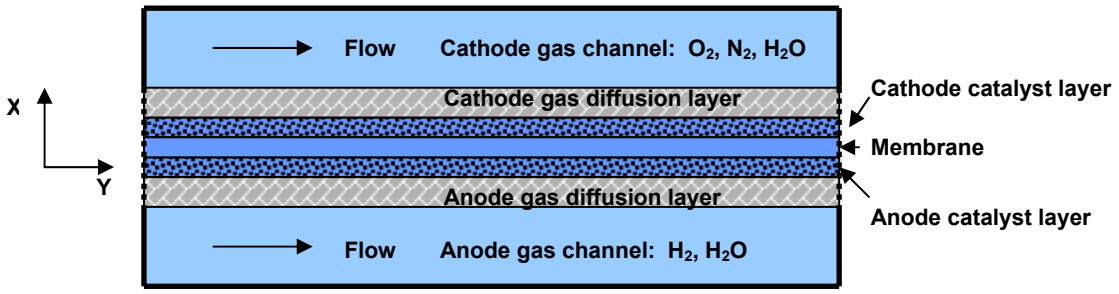

Figure 3.11 Zero-flux boundaries of the MEA (gas diffusion layers, catalyst layers, and membrane)

3.3 The Ion Exchange Membrane

The ion exchange membrane serves two purposes in a PEMFC: it conducts protons from the anode to the cathode catalyst layer and keeps the anode and cathode reactants separated. Typically, the ion exchange membrane, which will be referred to simply as the membrane, is made from a solid polymer material consisting of a backbone structure onto which are attached negatively charged side chains. These side chains are what allow the polymer to conduct positively charged protons. Figure 3.12 is an illustration of Nafion®, which is made by DuPont, and is the most commonly used membrane material. The backbone is very similar in composition to Teflon and the side chains include sulfonic acid groups. Dow Chemical also produces a membrane material that is very similar to Nafion®. It is shown in Figure 3.13. The backbone structure of both the Dow and Nafion® membranes are identical, the difference between the two materials being the composition of the sidechain.

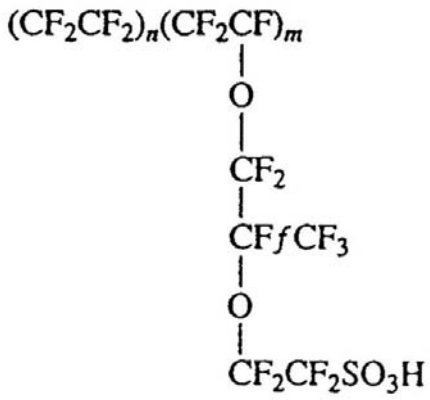

Figure 3.12 The chemical composition of Nafion®.

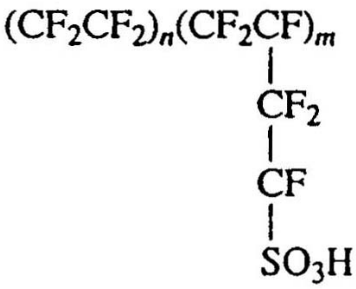

Figure 3.13 The chemical composition of Dow membrane material.

Various theories exist that seek to describe how protons are transported within the membrane material. One possibility is illustrated in Figure 3.14. In this case, protons are conducted through small, water filled pores within the membrane material by "hopping" from one sulfonic acid site to the next; the pores are essentially microscopic regions between the polymer fibers. A key element in this transport mechanism is the presence of water. Without exception, the ability of current polymer membrane materials to conduct protons is proportional to the level of hydration of the membrane. For this reason, the mechanisms by which water is transported within the membrane, as well as within the PEMFC in general, are of great practical interest.

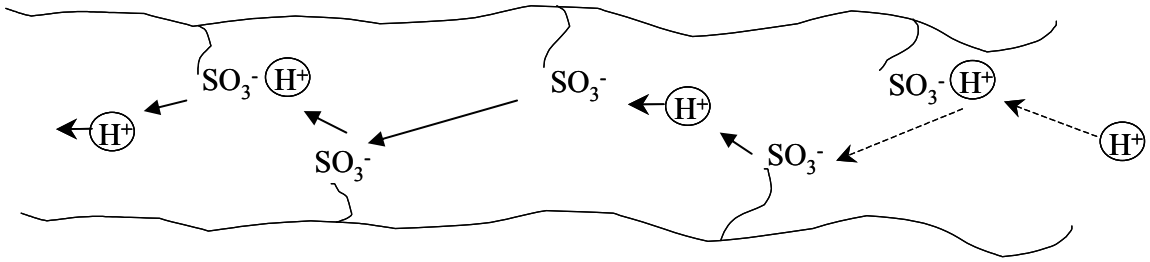

Figure 3.14 A conceptual diagram of proton transport through an ion conducting membrane [7].

3.3.1 Model Assumptions

The following assumptions apply to the model when solved in the membrane.

- Steady state
- Gas species mass fractions are numerically set to zero within the membrane; in addition, the membrane is assumed to be impermeable to the reactants.
- Water transport due to an applied pressure difference across the membrane is not considered.

3.3.2 Model equations

Only three quantities are transported within the membrane: protons, water dissolved within the polymer matrix, and energy. Consistent with the single domain approach, equations related to gas flow, including conservation of mass, conservation of momentum,

and the reactant species equations are solved in the membrane; the solutions are set to zero through numerical techniques that will be discussed in Section 5.

Transport of protons occurs by diffusion only as expressed by Eq. (3.31). The conductivity of Nafion® to protons is given as Eq. (3.32) and is a function of both the local temperature and membrane water content as determined by Springer, Zawodzinski, and Gottesfeld [1]. The current density can be calculated from the ionic conductivity and the ionic potential gradient as shown in Eq. (3.32b).

$$\nabla \cdot \left(\sigma_i \nabla \phi_i \right) = 0 \tag{3.31}$$

$$\sigma_i = (0.0005139\lambda - 0.000326) \exp\left[1268.0 \left(\frac{1}{303} - \frac{1}{T} \right) \right] \tag{3.32}$$

$$I_i = \sigma_i \nabla \phi_i \tag{3.32b}$$

Water dissolved within the polymer matrix can be transported by diffusion and by electro-osmotic drag (EOD). Diffusive transport of water can occur in either direction. In most cases, since the level of hydration is typically greater at the cathode, water will diffuse from the cathode to the anode. Electro-osmotic drag will always result in water transport from the anode to the cathode. The governing equation for dissolved water transport represents a balance between EOD and diffusion as shown in Eq. (3.33). The coefficient on the electro-osmotic drag term in Eq. (3.33) relates the number of water molecules dragged per proton moving from the anode to the cathode for a Nafion® membrane in contact with liquid water at 80 C (λ = 22). The diffusion coefficient is given as Eq. (3.34) and the membrane water content, or moles of water per mole of sulfonic acid, as Eq. (3.35). Both the form of the diffusion coefficient and the electro-osmotic drag coefficient were developed by Springer et al. [1] for Nafion® and are not applicable to other ion conducting polymers.

$$-\frac{2.5}{22F} \nabla \cdot \left(\lambda \sigma_i \nabla \phi_i \right) = \nabla \cdot \left(D^p_{WD} \nabla c^p_{WD} \right) \tag{3.33}$$

$$D^p_{WD} = 1.3 \text{x} 10^{-4} \exp\left[2416 \left(\frac{1}{303} - \frac{1}{T} \right) \right] \tag{3.34}$$

$$\lambda = c^p_{WD} M_p / \rho_p \tag{3.35}$$

Energy is transported through the membrane by conduction only as indicated by Eq. (3.36). The effective thermal conductivity is just the conductivity of the polymer material, Eq. (3.37).

$$\nabla \cdot \left(k_{eff} \nabla T \right) = 0 \tag{3.36}$$

$$k_{eff} = k_p \tag{3.37}$$

3.3.3 Boundary Conditions and Initial Conditions

Zero flux boundary conditions are specified for the membrane along the portions of its boundary touching the dashed line in Figure 3.15. Initially, the temperature in the membrane is set equal to the temperature along the boundaries of the gas channels. The initial value of the dissolved water concentration is set equal to that in the catalyst layers. The ionic potential is initially set equal to zero.

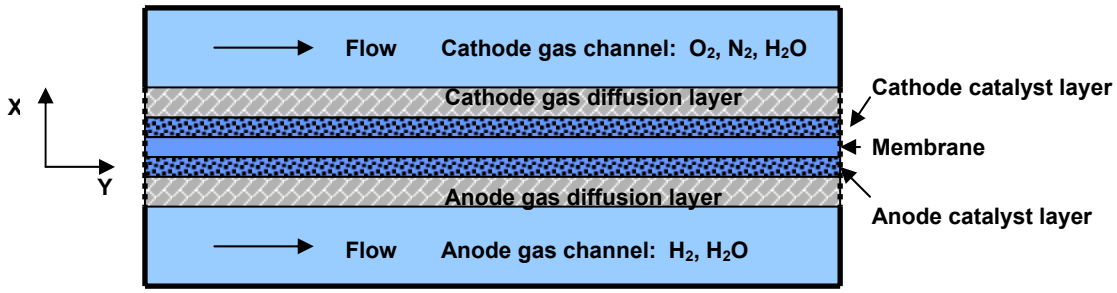

Figure 3.15 External zero flux boundaries for the membrane.

3.4 The Catalyst Layers

The catalyst layers are where the electrochemical reactions take place within a fuel cell. For a hydrogen / air PEMFC, both the anode and cathode layers are typically identical and consist of an ion conducting phase (recast Nafion®, for example), an electrically conductive phase (usually carbon particles), pores through which gaseous reactants are transported, and a noble metal catalyst (platinum is the most common) to facilitate the electrochemical reactions. Figure 3.16 is an illustration of a PEMFC catalyst layer.

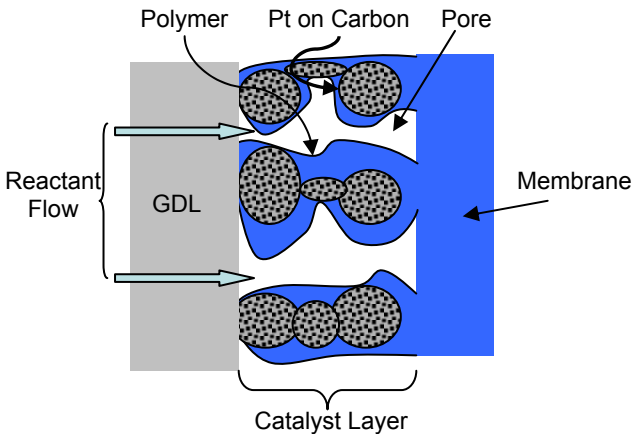

Figure 3.16 Close up view of a PEMFC catalyst layer.

Gaseous reactants enter the catalyst layer from the GDL and diffuse through the gas pores. To reach the platinum reaction sites, the reactants must dissolve into and diffuse through the polymer surrounding the carbon supported Pt catalyst. Thus, there are two diffusion pathways within the catalyst layer: one through the pores, and the other through the polymer. An increased resistance to diffusion along either of these pathways leads to a reduction in catalyst layer performance. The type of catalyst layer structure shown in Figure 3.16 is called an agglomerate structure, where the agglomerates are relatively non-porous regions consisting of carbon supported Pt catalyst encased in ion conducting polymer and separated from one another by gas pores.

It is possible to view the structural features of a fuel cell catalyst layer via examination with a scanning electron microscope (SEM). Figure 3.17 is a micrograph taken of a membrane electrode assembly (MEA) fabricated at Virginia Tech. The areas within the red border are the catalyst layers. In Figure 3.17, the thickness of both catalyst layers is about 29 microns. Typical layer thicknesses range from 3 – 100 microns and are largely dependent on the platinum loading as well as the weight ratio of platinum metal catalyst to carbon support particles. Figure 3.18 shows another micrograph of a catalyst layer at a magnification of 20,000 X. In this image, the agglomerates, one of which is circled in red, are clearly visible, as are the pores. The size of the agglomerates varies with the catalyst layer formulation and can also be determined using mercury porosimetry [25]. The pore size distribution as well as the porosity of the catalyst layer can be measured directly using

mercury porosimetry. Figure 3.19 is an image of the same catalyst layer as in Figure 3.18 but at a magnification of 100,000 X. In this image, the individual carbon support particles, which are spherical and nominally 30 – 50 nm in size, are clearly visible. Nafion® covers the particles and attaches them to one another. A transmission electron microscope (TEM) is used to take images of the catalyst layer at magnifications above 100,000X. Figure 3.20 is a micrograph of an agglomerate taken with a TEM at a magnification of 172,000X. The carbon support particles, Pt catalyst, and Nafion® ionomer are clearly visible in this image. The low number of pores (holes) indicates that, within an agglomerate, reactant transport can only occur by diffusion through the Nafion® ionomer surrounding the Pt catalyst sites. The Pt catalyst sites themselves are distributed somewhat non-uniformly on the support particles. "Clumping" of the catalyst leads to a reduction in the catalytic surface area available for reaction. The true platinum surface area can be measured experimentally using a technique called cyclic voltammetry, which will be discussed in Section 4.

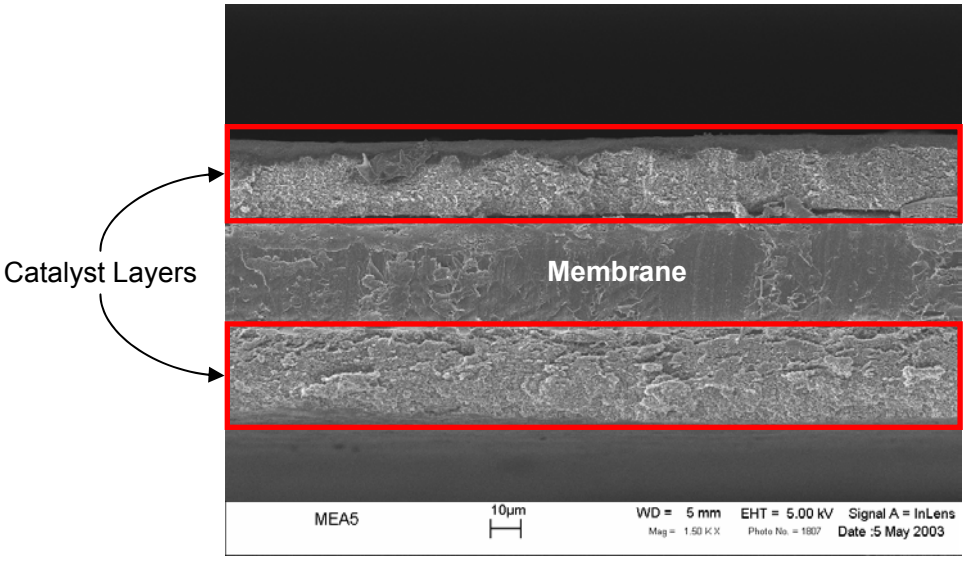

Figure 3.17 An SEM image of catalyst layers on a Nafion® 112 membrane. Magnification is 1.5 kX.

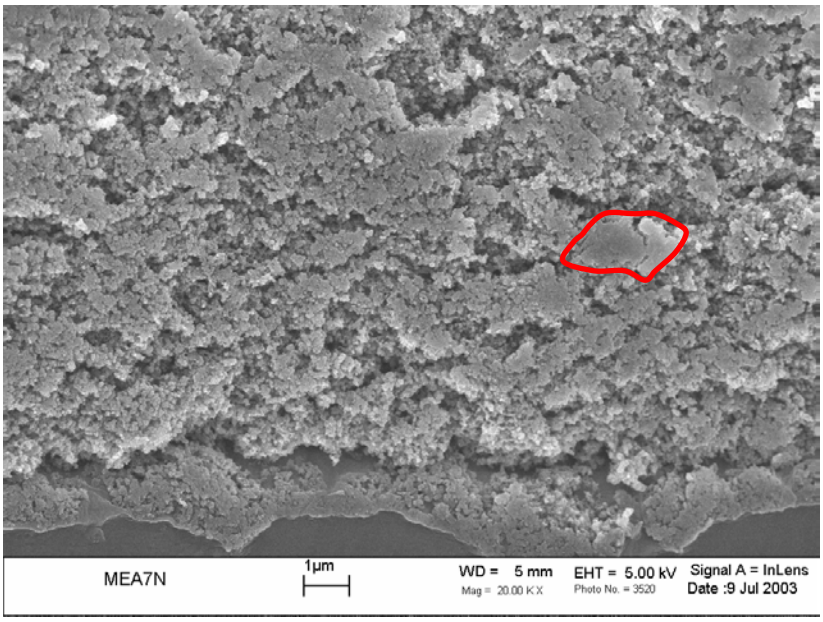

Figure 3.18 An SEM image of a catalyst layer at 20 kX with agglomerates and pores clearly visible.

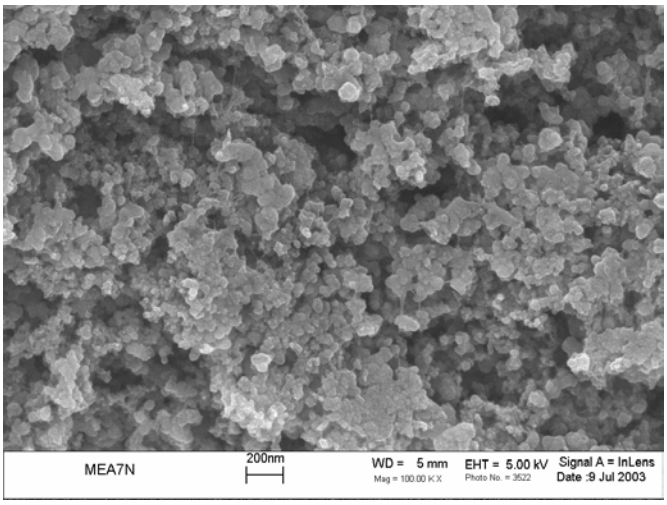

Figure 3.19 An SEM image of a catalyst layer at 100 kX with the carbon support particles clearly visible.

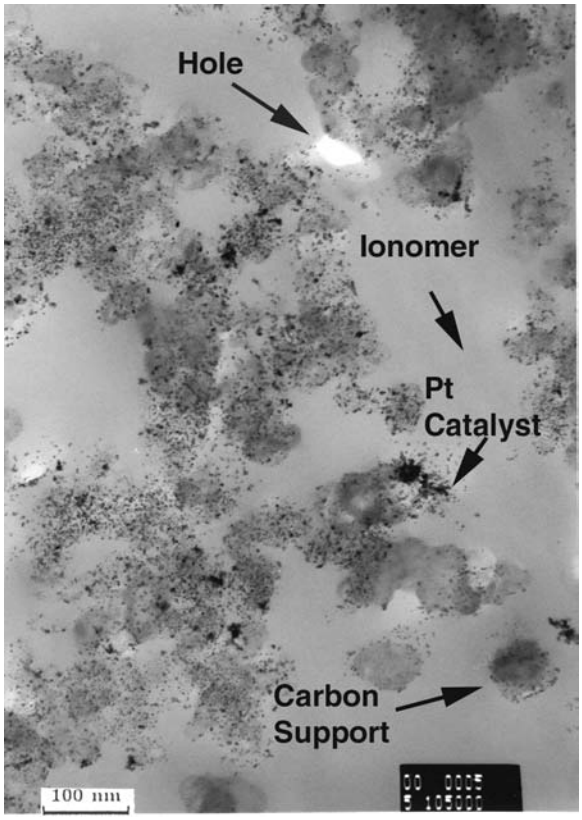

Figure 3.20 A TEM image of a catalyst agglomerate showing the principal components. Magnification is 172 kX.

3.4.1 Model Assumptions

The following assumptions apply to the model when solved in the anode and cathode catalyst layers:

- Steady state
- The catalyst layers are isotropic and homogenous.
- The momentum equations reduce to the Darcy equations.
- The gas flow is laminar and incompressible but not constant density.
- The viscosity of the gas mixture is constant and calculated from the inlet conditions.

- The thermal conductivity is based on the inlet gas species concentrations as well as the local liquid water saturation and solid composition of the catalyst layer; the thermal conductivity is allowed to vary with liquid water saturation.
- Liquid water within the pores is transported by capillary flow – this assumption requires that liquid water is able to wet the walls of the pores within the catalyst layer.
- Water taken up into the polymer phase of the catalyst layer comes from the vapor phase only; water released from the polymer phase is released into the liquid phase only.
- Water is produced by the electrochemical reaction in the cathode catalyst layer either in the liquid phase or in the vapor phase, depending on the local relative humidity.

3.4.2 Model equations

The conservation of mass equation for the gas phase is expressed as Eq. (3.38), which contains source terms for the consumption of hydrogen, Eq. (3.39) (applicable at the anode), the consumption of oxygen, Eq. (3.40) (applicable at the cathode), the production of water in the vapor phase, Eq. (3.41), the transfer of water between the liquid and vapor phases, Eq. (3.42), and the transfer of water between the dissolved and vapor phases, Eq. (3.43).

$$\nabla \cdot \left(\rho^{g} \bar{u}\right) = S_{H2} + S_{O2} + S_{LV} + S_{WP}\gamma_{LV} - S_{WD}\gamma_{WD} \tag{3.38}$$

$$S_{H2} = -\frac{M_{H2}}{2F}\left|R_{eff,a}\right| \tag{3.39}$$

$$S_{O2} = -\frac{M_{O2}}{4F}\left|R_{eff,c}\right| \tag{3.40}$$

$$S_{WP} = \frac{M_{W}}{2F}\left|R_{eff,c}\right| \tag{3.41}$$

$$S_{LV} = \psi s\gamma_{LV} - \psi(1-s)(1-\gamma_{LV}) \tag{3.42}$$

$$S_{WD} = h_{m}\left(\rho^{g}_{WV} - \rho^{p}_{WV}\right) \tag{3.43}$$

The source terms for oxygen and hydrogen consumption as well as water production are all functions of the effective reaction rate, Eq. (3.44). The effective reaction rate is based on the Butler-Volmer formulation, Eq. (3.45), and modified by an effectiveness term, Eq. (3.46), which is derived by considering steady state diffusion through a spherical shell with chemical reaction. Eq. (3.47) is Thiele's modulus. The reaction rate, as given by the Butler-Volmer formulation, is controlled by the reactant concentration in the polymer at the reaction site, the local activation overpotential given by ($\phi_{e,d}$ - ϕ_i), the exchange current density of the reaction (either the oxidation of hydrogen or the reduction of oxygen), as well as the catalytic surface area. It is also assumed that, as liquid water fills the pores within the catalyst layer, it blocks the access of reactants to the reaction sites, thus reducing the amount of catalytic area available for reaction and, thereby, the reaction rate [6]. The concentration of reactant in the polymer at the reaction site is determined by Henry's law, which specifies the dissolved concentration of a reactant at the gas interface, and the length of the diffusive path through the polymer. The length of the diffusive path is reflected by the effectiveness term, Eq. (3.46), which is a measure of how readily reactants diffuse through the polymer surrounding the spherical agglomerates that make up the catalyst layer. The expression itself is derived by considering conduction along the radius of a sphere. An effectiveness of 1.0 indicates that reactants diffusing through the agglomerates encounter no resistance. An effectiveness less than 1.0 indicates that the agglomerate offers resistance to reactant diffusion thereby limiting the reaction rate. The electrical potential is assumed to be constant over each electrode (catalyst and GDL). As indicated by Eq. (3.49), the electrical potential is set to zero on the anode side and to the negative of the total overpotential on the cathode side.

$$R_{eff,d} = R_d \eta_{aggl,d} \tag{3.44}$$

$$R_d = (1-s)A\ i_{o,k}\left(\frac{c_k^p}{c_{k,ref}}\right)^{\gamma}\left[e^{(\phi_{e,d}-\phi_i)\alpha_d\frac{n_d F}{RT}} - e^{-(\phi_{e,d}-\phi_i)\alpha_d\frac{n_d F}{RT}}\right] \tag{3.45}$$

$$\eta_{aggl,d} = \frac{3}{\beta_d}\left(\frac{1}{\mathrm{Tanh}(\beta_d)} - \frac{1}{\beta_d}\right) \tag{3.46}$$

$$\beta_d = L_{aggl,d}\sqrt{\frac{|R_d|}{c_k^p D_k^p n_d F}} \tag{3.47}$$

$$c_k^p = h_k^p c_k^g T \tag{3.48}$$

$$\begin{aligned} \phi_{e,a} &= 0 \\ \phi_{e,c} &= -\left(E_{th} - V_{cell}\right) \end{aligned} \tag{3.49}$$

As mentioned earlier, water is produced either in the liquid phase or in the vapor phase, depending on the local relative humidity. This is accomplished with the switch term given in Eq. (3.9b), the operation of which is discussed in Section 3.1.2. Mass exchange between the liquid and vapor phases, via Eq. (3.42), is taken into account in the same manner as in the gas channels and gas diffusion layers. Mass transfer from the vapor phase to the dissolved phase is taken into account with Eq. (3.43) which is modified by the switch term, γ_{WD}, given in Eq. (3.50). When the mass density of water vapor in equilibrium with the polymer, Eq. (3.51), is less than the local mass density of water vapor, Eq. (3.52), γ_{WD} is equal to 1, indicating that water can move from the vapor phase into the polymer (dissolved phase). Otherwise it is equal to 0. In this way water is allow to move from the vapor phase into the dissolved phase, but not vice versa. Water in the dissolved phase can be transferred to the liquid phase, and then transported as a liquid or evaporated. High values of the mass transfer coefficients used in the phase change source terms, Eq. (3.42) and Eq. (3.43), maintain equilibrium between the vapor, dissolved, and liquid phases. The mass density of water in equilibrium with the polymer is a function of the local vapor activity, which is given by Eq. (3.53).

$$\gamma_{WD} = \left(0.5 + \frac{\rho_{WV}^g - \rho_{WV}^p}{2\cdot\left|\rho_{WV}^g - \rho_{WV}^p\right|}\right) \tag{3.50}$$

$$\rho_{WV}^p = \rho_{sat}^g \cdot a \tag{3.51}$$

$$\rho_{WV}^g = w_{WV}\cdot\rho^g \tag{3.52}$$

$$a = 1.76e^{-6}\lambda^4 + 2.17e^{-4}\lambda^3 - 8.80e^{-3}\lambda^2 + 0.16\lambda - 0.12 \tag{3.53}$$

The conservation of linear momentum in three dimensions takes the form of the Darcy equation for flow in porous media, Eqs. (3.54a-c). The gas permeability of the catalyst layers is assumed to be the same as that of the GDL.

$$\frac{\partial P}{\partial x} = -\frac{\mu}{\kappa} u_x \tag{3.54a}$$

$$\frac{\partial P}{\partial y} = -\frac{\mu}{\kappa} u_y \tag{3.54b}$$

$$\frac{\partial P}{\partial z} = -\frac{\mu}{\kappa} u_z \tag{3.54c}$$

The species conservation equations for oxygen and water vapor are given as Eq. (3.55) and Eq. (3.56). In the catalyst layers, the diffusion coefficients for the individual species, Eq. (3.57), are modified with the Bruggeman correction to account for porosity and tortuosity, as well as an additional term that accounts for liquid water accumulation. The reason for using the Bruggeman correction in the catalyst layers, as opposed to separate porosity and tortuosity terms, is because, unlike in the gas diffusion layers, there is no experimental data for tortuosity. In addition, the Bruggeman correction has been shown to be an accurate representation of the coupling between porosity and tortuosity for porous media consisting of small spheres [29], which is characteristic of the catalyst layer.

$$\rho^g \bar{u} \cdot \nabla w_{O2} + w_{O2} \nabla \cdot \left(\rho^g \bar{u}\right) = \nabla \cdot \left(D_{O2}^g \rho^g \nabla w_{O2}\right) + S_{O2} \tag{3.55}$$

$$\rho^g \bar{u} \cdot \nabla w_{WV} + w_{WV} \nabla \cdot \left(\rho^g \bar{u}\right) = \nabla \cdot \left(D_{WV}^g \rho^g \nabla w_{WV}\right) + S_{LV} + S_{WP}\gamma_{LV} - S_{WD}\gamma_{WD} \tag{3.56}$$

$$D_{eff,k}^g = D_k^g \left[\varepsilon_{gdl}(1-s)\right]^{1.5} \tag{3.57}$$

The conservation equation for oxygen contains a source term that accounts for the consumption of oxygen via reaction at the cathode, Eq. (3.40). The water vapor species equation has source terms for the production of water in the vapor phase, Eq. (3.41), mass transport of water between the vapor and liquid, Eq. (3.42), and mass transport of water between the vapor and dissolved phases, Eq. (3.43).

The hydrogen and nitrogen mass fractions are calculated from the solutions of the oxygen, Eq. (3.55), and water vapor, Eq. (3.56), species equations as well as from the solution of the equation for overall conservation of mass in the gas phase, Eq. (3.38).

The equation for the transport of liquid water (saturation) within the pores of the catalyst layer is given by Eq. (3.58). The principle mechanism of transport is the same as in the GDL, namely, capillary flow. Advection is neglected and source terms are included to account for mass transfer between the liquid and vapor, and liquid and dissolved phases, as well as water production via the electrochemical reaction. The term representing mass transfer between the liquid and the vapor phases, Eq. (3.59), toggles between evaporation, when the local relative humidity is less than 98%, and condensation when the local relative humidity is greater than 98%. This is accomplished with the switch term, γ_{LV}, which is discussed in Section 3.1.2. Consistent with the approach used with the conservation of mass in the catalyst layer, the term representing mass transfer from the dissolved to the liquid phase, Eq. (3.60), allows mass transfer in only one direction – from dissolved to liquid; water can then move to the vapor phase through evaporation based on the local equilibrium conditions. Water production, governed by Eq. (3.61), takes place in the liquid phase when the relative humidity is greater than 98%, and in the vapor phase otherwise. All of the source terms in the liquid water transport equation are divided by the density of liquid water so that the units are consistent.

$$\nabla \cdot \left(D_{WL}^{cp} \nabla s\right) - S_{LV}/\rho_{WL} + S_{WP}\left(1-\gamma_{LV}\right)/\rho_{WL} - S_{WD}\left(1-\gamma_{WD}\right)/\rho_{WL} = 0 \tag{3.58}$$

$$S_{LV} = \psi s \gamma_{LV} - \psi(1-s)(1-\gamma_{LV}) \tag{3.59}$$

$$S_{WD} = h_m\left(\rho_{WV}^{g} - \rho_{WV}^{p}\right) \tag{3.60}$$

$$S_{WP} = \frac{M_W}{2F}\left|R_{eff,c}\right| \tag{3.61}$$

Dissolved water transport is governed by Eq. (3.62). Water is transported within the polymer phase of the catalyst layers by electro-osmotic drag, the only term on the left side, and by diffusion, the first term on the right side. A source term, Eq. (3.63), is needed to account for water exchange with the vapor and liquid phases within the catalyst layers. Equation (3.63) is similar in form to Eq. (3.43) and Eq. (3.60), used in the water vapor and liquid water transport equations, respectively. The membrane water content, λ, is defined by

Eq. (3.33). The effective dissolved water diffusion coefficient is expressed as Eq. (3.64), where D_{WD}^{P} is defined by Eq. (3.32).

$$-\frac{2.5}{22F}\nabla\cdot\left(\lambda\sigma_i\nabla\phi_i\right)=\nabla\cdot\left(D_{WD,eff}^{p}\nabla c_{WD}^{p}\right)+S_{WD}/M_W \tag{3.62}$$

$$\frac{S_{WD}}{M_W}=\frac{h_m}{M_W}\left(\rho_{WV}^{g}-\rho_{WV}^{p}\right) \tag{3.63}$$

$$D_{WD,eff}^{P}=D_{WD}^{P}\cdot\varepsilon_P \tag{3.64}$$

Ionic transport, or the transport of protons through the polymer phase of the catalyst layers, is governed by Eq. (3.65). Transport occurs by diffusion along the direction of a decreasing potential gradient (from anode to cathode in this model). The source term, Eq. (3.66), accounts for the rate of production of protons in the anode and consumption in the cathode. In the anode catalyst layer, the sign of the term S_i is positive; in the cathode catalyst layer, it is negative. The magnitude of the integral of S_i across each catalyst layer is the same. The physical meaning of this is that whatever protons are produced at the anode must be consumed at the cathode.

$$\nabla\cdot\left(\sigma_{i,eff}\nabla\phi_i\right)+S_i=0 \tag{3.65}$$

$$S_i=R_{eff} \tag{3.66}$$

The ionic conductivity of the polymer is expressed as Eq. (3.67). It is a function of membrane water content, λ, and the local temperature. The volume fraction of polymer within the catalyst layer has an effect on conductivity. This necessitates the use of an effective conductivity, expressed as Eq. (3.68). The local current density can be calculated using Eq. (3.69). The current density changes through the thickness of the catalyst layers as protons are produced and consumed, as well as down the channel, as reactants are depleted.

$$\sigma_i=(0.0005139\lambda-0.000326)\exp\left[1268.0\left(\frac{1}{303}-\frac{1}{T}\right)\right] \tag{3.67}$$

$$\sigma_{i,eff}=\sigma_i\varepsilon_P \tag{3.68}$$

$$I_i = \sigma_{i,eff} \nabla \phi_i \tag{3.69}$$

Energy is transported within the catalyst layers via conduction through the polymer electrolyte, carbon supported catalyst, reactant gases, and liquid water as well as by convection. The equation governing energy transport is Eq. (3.70). It is similar to the energy equation as it appears in the GDL with regard to the advective and diffusive components. A significant fraction of the chemical energy input to a fuel cell is lost due to the inefficiencies of the various processes taking place within the cell. These energy losses show up as thermal sources. The thermal sources in the energy equation that are associated with losses in the cell are ohmic resistance, Eq.(3.71), reversible heat transfer, Eq. (3.72), and activation energy, Eq.(3.73). In addition to these sources, an additional term that can be either an energy source or sink is needed to account for the phase change of water within the catalyst layers, Eq. (3.74). In the absence of other information, it is assumed that the enthalpy of the dissolved water is equal to the enthalpy of liquid water.

$$(\rho^g c_{eff} \bar{u} + c_{WL} \rho_{WL} s \varepsilon_{gdl} D_{Wl}^{CP} \nabla s) \cdot \nabla T = \nabla \cdot (k_{eff} \nabla T) + S_\Omega + S_{rev} + S_{act} + S_{pc} \tag{3.70}$$

$$S_\Omega = \sigma_{i,eff} (\nabla \phi_i \cdot \nabla \phi_i) \tag{3.71}$$

$$S_{rev} = \frac{R_{eff,k} T}{n_k F} \sum_{p-r} s_f^o \tag{3.72}$$

$$S_{act} = (\phi_e - \phi_i) R_{eff} \tag{3.73}$$

$$S_{pc} = (-S_{LV} + S_{DW} \gamma_{DW}) h_{fg} \tag{3.74}$$

Equation (3.71) is ohms law for heating due to charge flow through a conductor, in this case, protons through an ion conducting polymer. There is also a small amount of heat produced by the flow of electrons through the carbon portion of the catalyst layers; however, this is neglected given that it is insignificant compared to the other thermal sources. Equation (3.72) accounts for the heat associated with the entropy change during the electrochemical reactions themselves. It is the difference between the enthalpy of reaction and the Gibbs free energy of reaction. Equation (3.73) is the thermal source resulting from the activation losses associated with the hydrogen oxidation and oxygen reduction reactions.

It is a function of the reaction rate and the potential difference between the ion conducting and electron conducting phases of the catalyst layers. As with the gas diffusion layers, the potential in the electrically conductive phase of the catalyst layers is assumed constant and equal to zero at the anode and the negative of the total cell overpotential at the cathode. As in the GDL, energy is transported via conduction and advection by both the gas phase and liquid water. The solid carbon portion of the catalyst layer, as well as the polymer portion, also transports energy by conduction. The expression for the effective thermal conductivity is given as Eq. (3.75). The effective specific heat of the gas phase is given by Eq. (3.77).

$$k_{eff} = \varepsilon_{cat}(1-s)k_g + \varepsilon_{cat} s k_{WL} + \varepsilon_{cat}^{C} k_c + \varepsilon_{cat}^{p} k_p \tag{3.75}$$

$$k_g = \sum_k y_k^g k_k^g \tag{3.76}$$

$$c_{eff} = c_g \varepsilon_{gdl}(1-s) + c_{WL}\varepsilon_{gdl} s \tag{3.77}$$

$$c_g = \sum_k w_k^g c_k^g \tag{3.78}$$

3.4.3 Boundary Conditions and Initial Conditions

Boundary conditions for the catalyst layers are specified only on the external boundaries, those along the dashed lines in Figure 3.21. A zero flux condition is specified at the external boundaries for each of the governing equations. The initial conditions for the transport equations are:

- Gas species - Mass fractions are set equal to the gas channel inlet values.
- Liquid water – The level of liquid water saturation is set to zero.
- Dissolved water – The concentration of dissolved water is set such that the mass density of water vapor in equilibrium with the dissolved water is equal to the mass density of water vapor in the bulk gas. This makes the source term, S_{WD} / M_W, very small at the start of the simulation.
- Ionic charge - Ionic potential is set to zero within both the anode and cathode catalyst layers.

- Energy – The temperature within the catalyst layers is set equal to the cell temperature as specified along the sides of the gas channels.

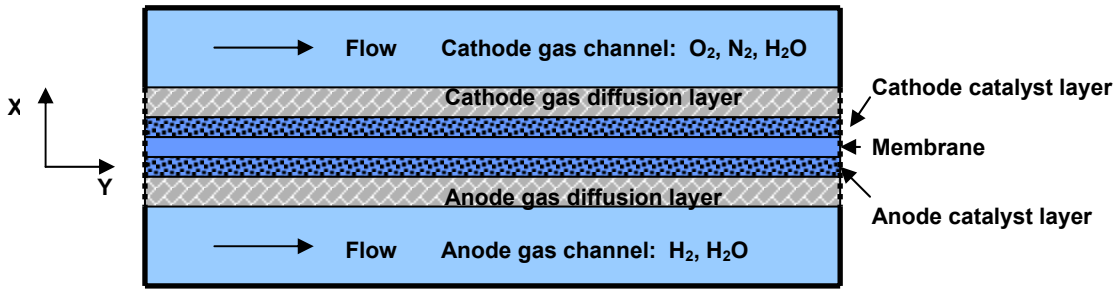

Figure 3.21 External zero flux boundaries of the catalyst layers.

3.5 The Collector Plates

In addition to providing a medium into which the gas channels can be set, the collector plates also transfer electrical current between the individual fuel cells comprising a stack as well as provide a means by which the cells may be cooled (through integrated cooling circuits). The collector plates are typically made out of graphite or another material with good electrical and thermal conductivity.

3.5.1 Model Assumptions

The following assumptions apply to the model in the anode and cathode collector plates:

- The collector plates (shoulders in particular) are explicitly included only in the 3D model. In the 2D model, the geometry represents a section of the fuel cell that does not include the collector plate shoulders.
- Because of the high thermal conductivity of the collector plate material, the temperature distribution in the collector plates is constant and set to the cell temperature.
- The electrical potential distribution is constant within the collector plates due to the high electrical conductivity of the collector plate material.

3.5.2 Model Equations

Only energy and electrical current are transported within the collector plates. Since the distribution of both of these quantities has been assumed constant, it is not necessary to solve any transport equations within the collector plates. The presence of the collector plates in the 3D model allows for the inclusion of mass transport effects associated with the presence of the collector plate shoulders in the solution domain. An illustration of the 3D model is shown in Figure 3.22. The collector plates may be thought of as being impermeable to all transported quantities except energy and electrical charge.

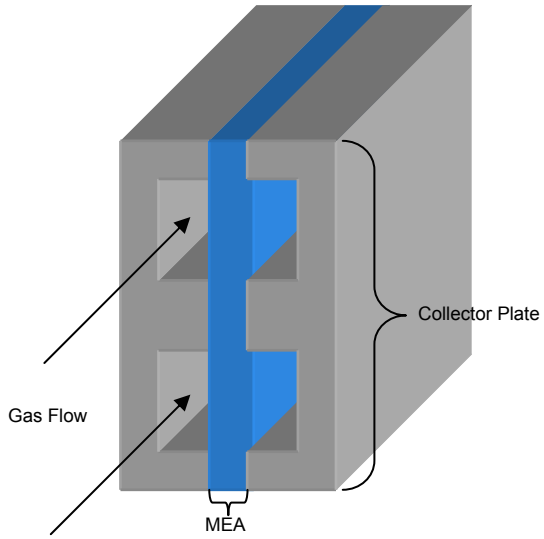

Figure 3.22 Three-dimensional geometry showing the collector plates.

4 Physical Property Evaluation

The accuracy and utility of a computational model is dependent not only on the mathematical formulation on which it is based, but also on the many physical properties needed to fully describe each of the fuel cell components. Some of these properties are available in the literature, others can be readily determined in the lab, and still others are not presently available in any form and must be estimated. In this section, the physical properties that have the greatest impact on the results of a given simulation are introduced and discussed. Properties involving catalyst layer microstructure, reactant transport through the polymer phase of the catalyst layer, electrochemistry, and liquid water transport in the porous gas diffusion and catalyst layers all fall into this category.

4.1 Catalyst layer structure

The catalyst layer may be thought of as a porous composite of two materials, ion conducting polymer and carbon supported catalyst. Changes in the amount of polymer, carbon supported catalyst, or void volume will affect the performance of the catalyst layer by altering transport mechanisms and / or electrochemical performance. A conceptual illustration of the structure of the catalyst layer is shown in Figure 4.1. This type of catalyst layer is said to have an agglomerate structure given that the carbon supported Pt catalyst sites are arranged in relatively non-porous groups called agglomerates. The carbon support particles that form the foundation of an agglomerate are held together by ionomer. The agglomerates themselves are separated from one another by voids. When modeling an agglomerate catalyst layer, it is important to know the following structural properties:

- Total pore volume fraction (porosity)
- Pore size distribution
- Ionomer volume fraction
- Carbon support and Pt volume fractions
- Layer thickness
- Tortuosity of the layer

- Information regarding how the layer is deformed when the complete PEMFC is assembled.

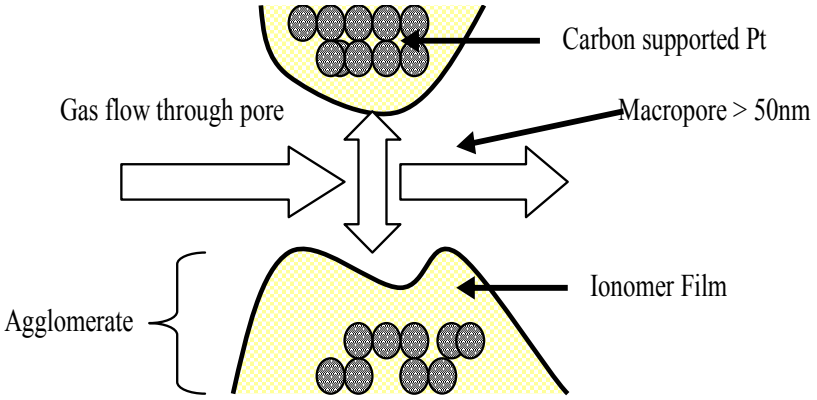

Figure 4.1 A catalyst layer with an agglomerate structure.

Within the catalyst layer, both gaseous reactants and liquid water are transported within the voids, or pores, between the agglomerates. With regard to the gaseous reactants, the principle transport mechanism is diffusion. The diffusive flux of gaseous reactants through the catalyst layer is influenced by the porosity, tortuosity, and layer thickness and is expressed by Eq. (4.1). Due to the absence of empirical data concerning the tortuosity of the catalyst layer, an alternate expression is used that combines the tortuosity and porosity terms. This is known as the Bruggeman correction; the alternate expression is given as Eq. (4.2). It is believed that the Bruggeman correction, which is typically used for structures consisting of spherical particles (such as an agglomerate catalyst layer), allows for a good approximation of the effects of tortuosity and porosity on gas diffusivity within the pores of the catalyst layer.

$$N_{k,D}^{g} = -\frac{\varepsilon_{cat}}{\tau_{cat}\Delta t_{cat}}\rho^{g} D_{k}^{g} \Delta w_{k}^{g} \tag{4.1}$$

$$N_{k,D}^{g} = -\frac{(\varepsilon_{cat})^{1.5}}{\Delta t_{cat}}\rho^{g} D_{k}^{g} \Delta w_{k}^{g} \tag{4.2}$$

The porosity of the catalyst layer can be determined using mercury porosimetry or by comparing the solid catalyst layer volume to the total catalyst layer volume. The latter technique involves evaluating the solid volume of the catalyst layer based on its mass and composition and the total volume of the catalyst layer based on its thickness (determined using an SEM). The mass of the catalyst layer is determined by weighing the catalyst layer after it has been painted onto a Teflon decal and dried to remove all of the solvent. The solid volume of the catalyst layer, V_s, is then calculated using Eq. (4.3).

$$V_s = \frac{m_{cat} x_p}{\rho_p} + \frac{m_{cat} x_C x_{Pt}}{\rho_{Pt}} + \frac{m_{cat} x_C (1 - x_{Pt})}{\rho_C} \tag{4.3}$$

m_{cat} is the mass of the catalyst layer, x_p is the mass fraction of polymer in the catalyst layer, x_C is the mass fraction of carbon supported catalyst, x_{Pt} is the mass fraction of platinum on the carbon supported catalyst, ρ_p is the density of the polymer, ρ_C is the density of the carbon support, ρ_{Pt} is the density of platinum. The total volume of the catalyst layer including the pores, V_{tot}, can be estimated from thickness measurements taken with an SEM. Figure 4.2 shows the image used to measure the thickness of the catalyst layers for the test MEA on which the physical properties for the computational model are based. From these two volumes the porosity, ε_{cat}, which is the volume fraction of pores in the catalyst layer relative to the total layer volume, can be calculated using Eq. (4.4).

$$\varepsilon_{cat} = \frac{V_{tot} - V_s}{V_{tot}} \tag{4.4}$$

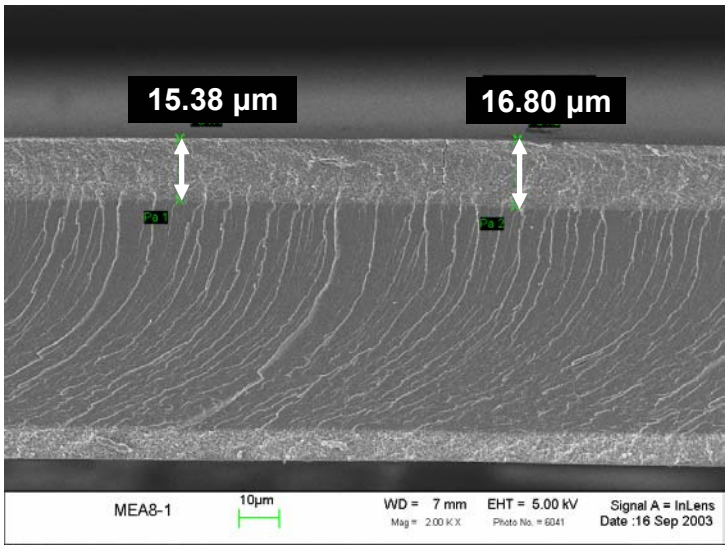

Figure 4.2 An SEM micrograph of the test MEA showing catalyst layer thickness.

Advective transport of gaseous reactants within the catalyst layer is also influenced by the physical structure of the layer through its permeability to gas flow. However, as with the tortuosity, data is not available for the permeability of the catalyst layer. An alternative approach involves using the Carmen-Kozeny equation to calculate the permeability from the porosity and mean particle diameter; the mean particle diameter is related to the pore size distribution, which can be measured using mercury porosimmetry. Like the Bruggeman correction, the Carmen-Kozeny equation is valid for porous media consisting of small spheres and is expressed by Eq. (4.5) [31]. The permeability, K_{abs}, calculated by the Carmen-Kozeny equation is the absolute permeability of the catalyst layer. The permeability to gases involves a modification of K_{abs} to account for the presence of liquid water within the pores. With this modification, the permeability of the catalyst layer to gases is given by Eq. (4.6). The advective mass flux of gaseous species within the catalyst layer can then be calculated with Eq. (4.7).

$$K_{Abs} = \frac{\varepsilon_{cat}^3}{180(1-\varepsilon_{cat})^2} d_{agg}^2 \tag{4.5}$$

$$\kappa = K_{Abs}(1-s) \tag{4.6}$$

$$N_{k,Adv}^{g} = \rho^{g} \bar{u}(\kappa) w_k \tag{4.7}$$

The ionomer content of the catalyst layer is readily determined from the composition of the layer. It affects performance principally through its influence on the ionic conductivity of the layer. Simply put, a greater volume fraction of ionomer, ε^{p}_{cat} , within the catalyst layer leads to an increased ionic conductivity, as shown in Eq. (4.8). Depending on how the catalyst layer is constructed, an increase in the volume fraction of ionomer may come at the cost of a decrease in porosity or an increase in layer thickness, both of which have implications related to gas transport. This results from the fact that, as more polymer is added to the catalyst layer, the polymer must either displace another catalyst layer component (pores) or the total volume of the catalyst layer must increase.

$$\sigma_{i,eff} = \sigma_i \varepsilon^{p}_{cat} \tag{4.8}$$

The volume fraction of the carbon support particles within the catalyst layer, ε^{c}_{cat}, affects performance through its influence on electrical conductivity [24, 32]. As a rule, there must be a sufficient amount of carbon within the catalyst layer to provide an electrically conductive pathway from the reaction sites to the GDL. In addition, the amount of carbon within the catalyst layer is typically the determining factor in the thickness of the catalyst layer. The volume fraction of carbon can be determined from the catalyst layer composition.

In current PEMFC models [13, 15, 17], the catalyst layer is assumed to be uniform in structure. In particular, the thickness of the catalyst layer over the entire surface of the MEA is assumed to be constant. This, however, is only an approximate representation of the structure of the catalyst layer once it has been assembled in a fuel cell. During assembly, the entire fuel cell is compressed to minimize interfacial resistances (thermal, electrical) between the components. One effect of this is that the GDL is extruded into the catalyst layer. Figure 4.3 shows a catalyst layer before assembly; it exhibits a very uniform thickness. Figure 4.4 shows a catalyst layer after assembly; the layer thickness is highly non-uniform and appears to be related to the size and shape of the fiber bundles comprising the GDL, which is ELAT™ in this case. Depending on the severity of the non-uniformity of the catalyst layer, neglecting the thickness variation may have implications for diffusive processes such as reactant

transport and liquid water transport. Currently, the model does not include effects related to a non-uniform catalyst layer structure.

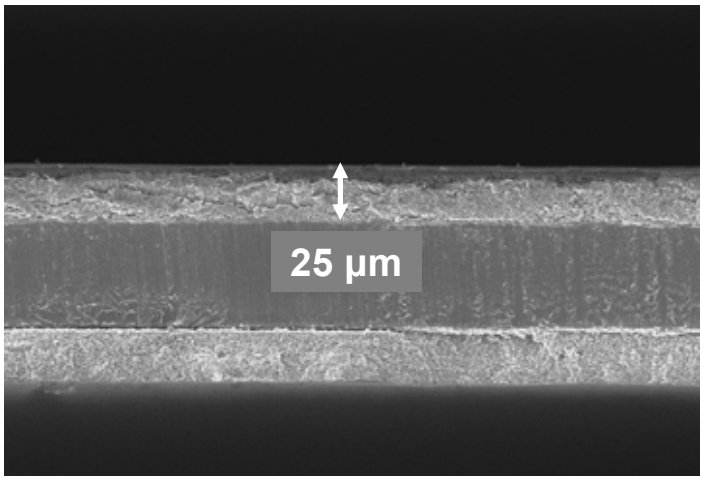

Figure 4.3 Catalyst layer before assembly in the fuel cell (1500 X).

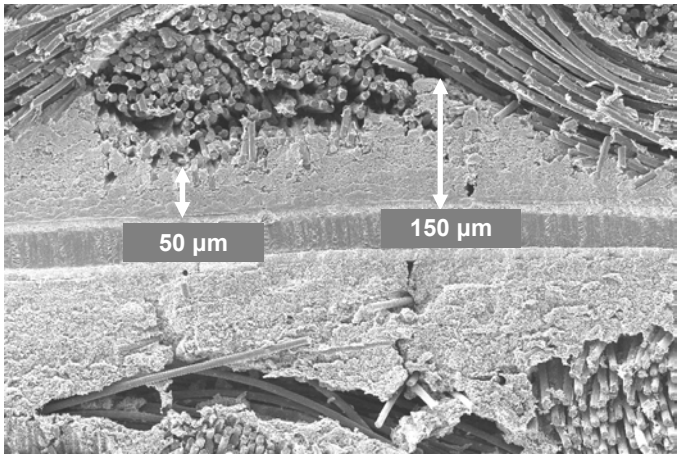

Figure 4.4 Catalyst layer after assembly in the fuel cell (500X).

4.1.1 Additional structural information needed to improve model accuracy

While the assumptions used for structural properties in this work are based on the best currently available data, computational models of PEMFCs can be improved by collecting the following information related to the physical structure of the catalyst layer:

- Tortuosity of the catalyst layer – which allows for the use of the more explicit Eq. (4.1) in place of Eq. (4.2), which relies on the Bruggeman correction.
- The absolute permeability of the catalyst layer and the dependence of permeability on liquid water saturation - This would eliminate the need to rely on the Carmen-Kozeny relation to calculate the absolute permeability. In addition, the dependence of liquid water permeability on saturation is required to more accurately model liquid water transport in the catalyst layer.
- Effect of non-uniformities in layer thickness on transport and performance.

4.2 Reactant Transport through the Polymer Phase of the Catalyst Layer

As mentioned in Section 3, there are two parallel reactant mass transport pathways through the catalyst layer: transport in the gas phase through the catalyst layer pores and transport through the ionomer to the catalyst sites. Transport of reactant species through the ionomer is not explicitly modeled as a diffusive flux. Instead, it is taken into account with an effectiveness parameter that operates on the reaction rate. The specifics are discussed in Section 3. The effectiveness and related expressions are presented again, for clarity, as Eqs. (4.9-4.11). Thiele's modulus, β_d, has been reformulated, as Eq. (4.10), to isolate the physical properties associated with reactant transport through the ionomer. These properties are listed as follows:

- The characteristic length of the agglomerate, $L_{aggl,d}$.
- The dissolved concentration of a given reactant (hydrogen or oxygen) at the surface of an agglomerate, c_k^p - This can be found using Henry's law which requires the specification of a solubility coefficient, h_k^p, for each of the reactants in the ionomer (Nafion® 1100 series).
- The diffusion coefficient of a given reactant (hydrogen or oxygen) in the ionomer, D_k^p.

It is clear from Eqs. (4.10) and (4.11) that an increase in the characteristic length of the agglomerate, which amounts to increasing the length of the diffusive pathway, will result in a decrease in effectiveness; on the other hand, an increase in dissolved reactant concentration

(solubility) or dissolved reactant diffusion coefficient will lead to an increase in effectiveness.

$$\eta_{aggl,d} = \frac{3}{\beta_d}\left(\frac{1}{\mathrm{Tanh}(\beta_d)} - \frac{1}{\beta_d}\right) \tag{4.9}$$

$$\beta_d = \frac{L_{aggl,d}}{\sqrt{c_k^p D_k^p}}\sqrt{\frac{|R_d|}{n_d F}} \tag{4.10}$$

$$c_k^p = h_k^p c_k^g T \tag{4.11}$$

The characteristic length of the agglomerates can be calculated using mercury porosimmetry and by assuming a spherical geometry [25]. The reactant solubility and diffusion coefficient can be determined using chronoamperometry [22]. Data is available in the literature for the solubility and diffusion coefficient of oxygen in Nafion® film over a range of temperatures while in equilibrium with fully humidified oxygen gas at 1 atm [22] and 5 atm [19]. Unfortunately, it is not possible to accurately calculate a solubility coefficient, h_k^p, from these two sources since the concentration of oxygen dissolved in Nafion® film appears to approach saturation at an oxygen partial pressure lower than those reported, as illustrated in Figure 4.5. For this reason the solubility coefficient used in this model is based on the data in Zhang, Ma, and Muckerjee [22] that was taken at the lower pressure and is assumed to be closer to the true value, which is unknown. The diffusion coefficient of oxygen in Nafion® film may also be a function of pressure, but there is insufficient data to make the case either way. Data for hydrogen solubility and diffusivity was taken from the work of Bernardi and Verbrugge [12]. They present equations for the diffusion coefficient and solubility of hydrogen in Nafion® 1200. The present model is based on Nafion® 1100, which is a slightly different polymer and may have different properties with regard to dissolved reactant transport. At present, data for the solubility and diffusion coefficient of hydrogen in 1100 series Nafion® is unavailable. It has been shown that the diffusive properties of recast Nafion® differ somewhat from Nafion® films [25]. For this reason, the diffusion coefficient of oxygen used in the model is less than that presented by Zhang, Ma, and Muckerjee, which was experimentally determined for Nafion® film.

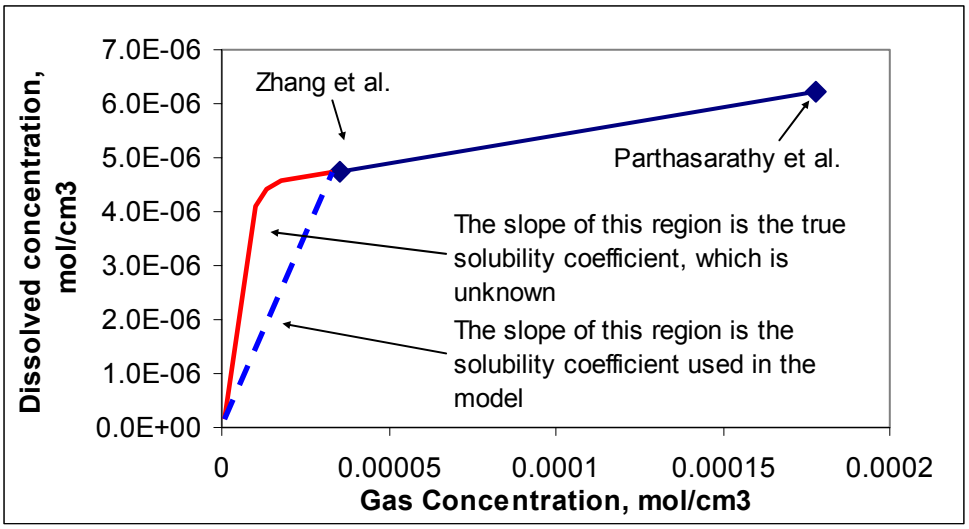

Figure 4.5 Existing data for oxygen solubility in Nafion® 1100 does not extend into the region necessary for calculating the solubility coefficient, h_k^p.

4.2.1 Additional information needed related to reactant transport within the ionomer phase of the catalyst layer

The physical properties used for solubility and reactant transport in current computational models are based on experimental conditions, with regard to temperature, pressure, and polymer water content that are not always in agreement with the conditions input to the model. The following properties related to the transport of reactants through the polymer phase of the catalyst layer are needed to improve the accuracy of existing computational models:

- Hydrogen and oxygen solubility in recast polymer as a function of temperature, applied gas pressure, and polymer water content for recast polymer - Recast polymer, Nafion® in particular, has been shown to have different properties than Nafion® film [25].
- The diffusion coefficient of hydrogen and oxygen in recast polymer as a function of temperature, pressure, and polymer water content.
- More detailed information regarding the size, and particularly the shape, of the agglomerates in the catalyst layer.

4.3 Electrochemistry

The electrochemical reactions taking place within the catalyst layers are what drive the fuel cell. Modeling of these reactions, and associated effects, in both the anode and cathode catalyst layers requires the specification of the following physical properties:

- The amount platinum catalyst surface area that is available to participate in the reactions - This differs from the theoretical maximum amount of surface area as determined from the catalyst loading.
- The exchange current density for both the oxygen reduction and hydrogen oxidation reactions.
- The charge transfer coefficient (related to the Tafel slope) for both reactions.

The maximum amount of platinum catalyst surface area available to participate in the electrochemical reactions can be calculated from the layer composition. For the test MEA used in this work, each catalyst layer nominally contains 1.625 mg of platinum catalyst (0.325 mg/cm^2) with a weight fraction of platinum to carbon support of 20%. Table 4.1 shows the maximum possible surface area of platinum per gram of carbon supported catalyst for a variety of different catalyst formulations [5]. The catalyst type used in fabricating the test MEA is highlighted.

Table 4.1 Platinum surface area for different carbon supported catalyst formulations from E-tek®.

Catalyst type[1]	Surface area / Pt mass, m^2/g
10% Pt on carbon black	140
20% Pt on carbon black	112
30% Pt on carbon black	88
40% Pt on carbon black	72
60% Pt on carbon black	32
80% Pt on carbon black	11
Pt black	28

[1] Carbon support is Vulcan XC-72

The maximum possible platinum surface area in each catalyst layer, for the test MEA, is calculated from the layer composition and the information in Table 4.1 to be 182,000 mm^2.

Since the Pt catalyst deposition is non-uniform, as shown in Figure 3.18, the true platinum surface area will be somewhat less than the maximum. The true surface area of Pt is found using cyclic voltammetry.

Cyclic voltammetry is an electrochemical technique that allows for the measurement of the charge associated with the adsorbtion and desorbtion of hydrogen from the platinum catalyst [33]. The amount of charge transfer as hydrogen is adsorbed or desorbed can be related to the platinum area as shown by Eq. (4.12)

$$A_{act} = \frac{Q_A}{Q_{Pt}} \tag{4.12}$$

where Q_A is the amount of charge (μC) transferred during adsorption (or desorption) and Q_{Pt} is the charge per unit area transferred during the adsorption of a monolayer of hydrogen on atomically smooth platinum (210 μC/cm^2). Figure 4.6 shows a voltammagram for the test MEA.

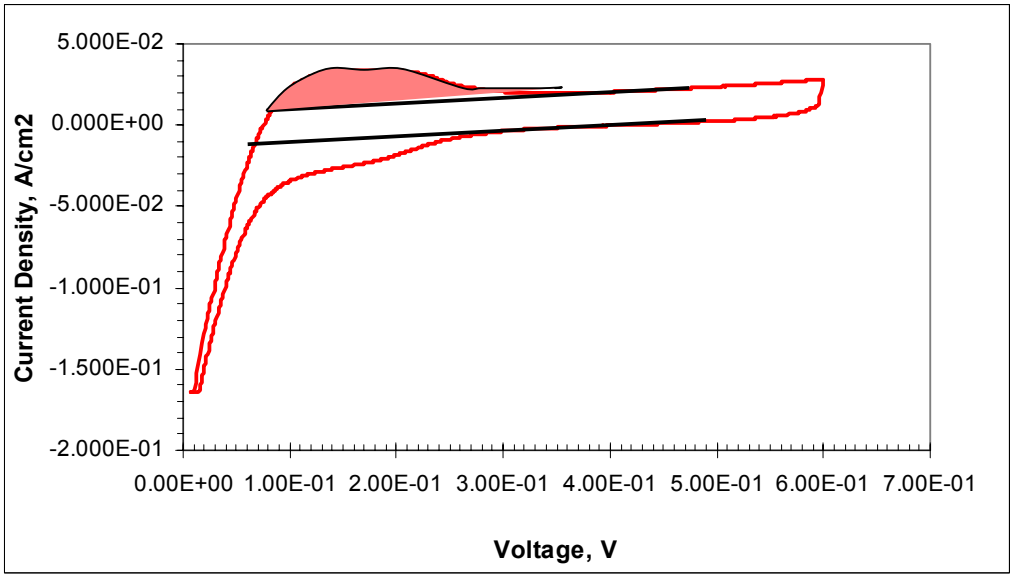

Figure 4.6 The platinum surface area is calculated from the shaded region shown in the voltammagram.

The platinum surface area for the test MEA is 22,700 mm^2. Comparing this value to the maximum of 182,000 mm^2 shows that about 13% of the platinum catalyst is being

utilized. The remaining catalyst is not active because it is blocked by adjacent particles or because it is not in contact with ionomer and ,thus, cannot participate in the electrochemical reactions.

The reference exchange current density for the oxygen reduction reaction at the cathode, as well as the corresponding reference oxygen concentration, is based on data presented by Zhang, Ma, and Muckerjee [22]. The reference exchange current density is temperature dependent. For the hydrogen oxidation reaction taking place at the anode, the reference exchange current density is estimated based on information presented by Larminie and Dicks [34]. They suggest using a reference exchange current density for the anode reaction that is at most 10^5 times larger than that at the cathode. The reference hydrogen concentration is assumed to correspond to fully humidified hydrogen at the cell temperature and 1 atm of total pressure. The dependence of the exchange current density on reactant concentration at the catalyst surface, for both the anode and cathode reactions, is assumed to be first order. It should be noted that both Zhang et al. [22] and Parthasarathy et al. [19] present data showing a jump in the reference exchange current density when the overvoltage exceeds ~300 mV. This accompanies an increase in the Tafel slope, and both effects are thought to result from the surface of the Pt catalyst making a transition from an oxide covered to an oxide free state as the current density is increased. Neither effect is included in the model because a suitable mathematical formulation for these phenomena has not yet been developed.

The charge transfer coefficient, α, appears in the exponential terms in the Butler-Volmer formulation for reaction rate, Eq. (3.45), and is related to the Tafel slope as shown in Eq. (4.13). Parthasarathy et al. [19] present data for the charge transfer coefficient associated with the oxygen reduction reaction over a range of temperatures. Their results indicate that the charge transfer coefficient increases slightly with temperature. However, the change with temperature is nearly constant. For this reason the exponential terms of the Butler-Volmer formulation for reaction rate, as solved in the cathode catalyst layer, are considered to be temperature independent. The charge transfer coefficient for the hydrogen reduction reaction was taken from Larminie and Dicks [34]. It is also assumed to vary only slightly with temperature, resulting in constant Bulter-Volmer exponential terms for the hydrogen reduction reaction in the anode catalyst layer.

$$\alpha_d = \frac{S_{tafel}}{R \cdot T} nF \tag{4.13}$$

4.3.1 Additional information needed related to electrochemistry

There is some amount of uncertainty involved with determining the values of the electrochemical parameters required by fuel cell models. The following information is needed to increase the accuracy of existing computational models:

- The variation of exchange current density with reactant concentration, temperature, and ionomer water content - These data would allow for increased model accuracy as local conditions vary within the fuel cell.
- The variation of platinum catalyst surface area with ionomer water content.
- The variation of exchange current density and charge transfer coefficient with cell overvoltage or cell current density and temperature - Ideally this would result in a mathematical formulation for the change in reference exchange current density and charge transfer coefficient due to the transition of the platinum catalyst surface from oxide covered to oxide free.

4.4 Liquid water transport

Liquid water transport through the catalyst layer and gas diffusion layer, which is assumed to result from capillary flow, is modeled as a diffusive process that is a function of the change in capillary pressure with liquid water saturation and the permeability of the layer to liquid water. The diffusive velocity of liquid water, through either the catalyst layer or the gas diffusion layer, is expressed by Eq. (4.14), with the permeability to liquid water given by Eq. (4.15), which is assumed to be a first order function of saturation. As with the absolute permeability, the change in capillary pressure with saturation is also a function of the pore size distribution [28]. Unfortunately, an exact relation linking pore size distribution to the change in capillary pressure with saturation for PEMFC components has not yet been experimentally determined. For this reason it is necessary to estimate the capillary pressure dependence on saturation as discussed in Section 3. To reiterate, the relationship between the change in capillary pressure and saturation used in this model was developed by Natarajan

and Nguyen [8] through a process of fitting their liquid water transport model to PEMFC test data. The same functional relationship is used in both the gas diffusion and catalyst layers. The permeability of both the catalyst layer and gas diffusion layer to liquid water is assumed to vary with saturation as given by Eq. (4.15).

$$D_{WL}^{cp} = -\frac{\rho_{WL} g}{\mu_{WL}} K_L \frac{\partial P_c}{\partial s} \nabla s \tag{4.14}$$

$$K_L = K_{Abs} s \tag{4.15}$$

It is possible that the assumption that liquid water transport occurs by capillary flow in both the gas diffusion and catalyst layer is incorrect. Recalling the discussion of capillary flow given in Section 3, the direction of the flow of the wetting phase (liquid water for a hydrophilic pore) is towards the non-wetting phase (gas). It is likely that this accurately describes the transport mechanism within the catalyst layer, as the pores are lined with hydrophilic ionomer. However, the gas diffusion layer is typically treated with a hydrophobic material, like Teflon, to repel water. In the case of a hydrophobic pore, the liquid water does not wet the solid surface, which is the reverse of the situation shown in Figure 3.8 of Section 3, repeated here for clarity. Figure 4.8 illustrates the interaction between the gas and liquid in a hydrophobic pore.

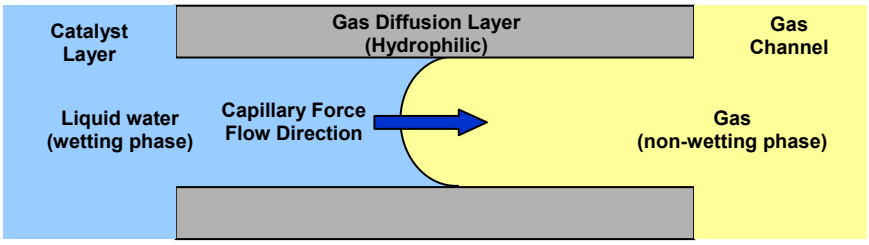

Figure 4.7 Capillary flow in a hydrophilic pore such as in the catalyst layer.

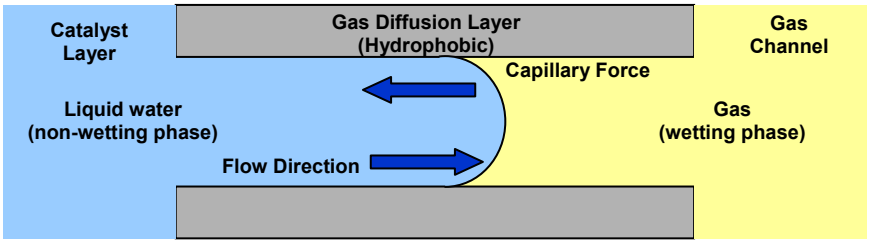

Figure 4.8 Capillary flow in a hydrophobic pore such as in the GDL.

In the case of the hydrophobic pore, capillary pressure causes the liquid to be forced back toward the catalyst layer. The net result is that the capillary force opposes the flow and the liquid pressure must exceed the capillary pressure in order for the liquid water to flow toward the GDL. This is a different transport mechanism than that taking place in the hydrophilic pore of Figure 4.7 where the capillary force drives the flow of liquid toward the GDL. Currently, both the catalyst layer and the GDL are assumed to be composed of hydrophilic material.

Modeling results presented in this work, in Section 6, indicate that liquid water transport is temperature dependent, i.e. the transport rate of liquid water out of the porous media and into the gas channels decreases with temperature. Natarajan and Nguyen [8] also present modeling results supporting this trend but only for a *local relative humidity less than 100%*. They reason that the performance, with regard to limiting current, drops off at lower temperatures because the cathode gas stream cannot hold as much water as at higher temperatures, meaning that evaporation rates will be lower and more liquid water will accumulate in the porous GDL. It has been observed experimentally that there is a decrease in limiting current (and overall performance) with temperature when the local vapor is *fully saturated*. Under these conditions, the model of Natarjan and Nguyen will not predict a change in limiting current since the rate of evaporation no longer changes with temperature. The model presented in this work can be used to model the shift in performance with temperature at fully saturated conditions, but doing so requires a modification of the liquid water diffusion coefficient, Eq. (4.14), which is a function of temperature through the viscosity, density, and surface tension (which is part of the capillary pressure). The changes in density and surface tension with temperature offset each other. The change in viscosity, which for liquid water decreases with temperature, is likely a cause of the reduced liquid

water transport rate at lower temperature. There may, however, be additional temperature effects that are not taken into account through the liquid water transport equations used in the model presented in this work. One of these has to do with liquid water transport in the gas channels.

Liquid water present in the non-porous gas channels is modeled as consisting of droplets of negligible volume moving at the bulk flow velocity. When modeled in this fashion, the level of saturation at the GDL / gas channel interface is effectively zero along the entire length of the fuel cell. It has been suggested by others [8, 35] that liquid water is actually transported as a film that travels along the gas channel / GDL interface. Assuming that this mode of liquid water transport exists in the cell, it is possible to show a coupling between the liquid water removal rate from the cell and temperature. Experimental data, taken as part of this work and presented in Figure 4.9, show that the limiting current increases with temperature under fully saturated conditions, for a constant mass flow rate of reactants. As the temperature of the flow stream is increased, its density decreases which, through conservation of mass, requires a corresponding increase in flow velocity. Increased flow velocity causes the liquid film to be more readily transported through the gas channels and out of the cell, thereby reducing the overall level of saturation within the porous media and enhancing reactant transport through the porous media. The result is the increase in the limiting current with temperature shown in Figure 4.9.

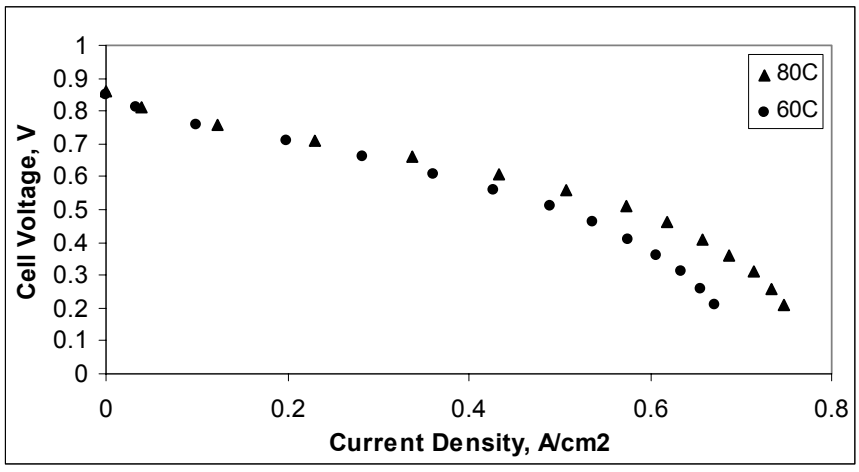

Figure 4.9 Increase in limiting current with temperature at a constant mass flow rate. The cell temperature is equal to the reactant temperature. Reactants are fully humidified.

4.4.1 Additional information needed related to liquid water transport

The transport of liquid water within both the porous and non-porous regions of the fuel cell is not a well understood phenomenon. Currently, the convention is to model liquid water transport in the porous media as being driven by capillary action. This may or may not be the case, and additional experimental and analytical work is needed. Liquid water existing in the non-porous gas channels is, in this work, assumed to be in the form of droplets of negligible volume moving with the bulk flow. It may be that a different transport mechanism exists; perhaps water is transported as a film along the GDL / gas channel interface. Currently, there are few, if any, computational codes that can model two-phase flow with the degree of accuracy needed to explore liquid water transport in the gas channels. This is another area where additional work, both analytical and experimental, is needed. The following information is needed to increase the accuracy of existing computational models with regard to liquid water transport:

- Clarification of the dominant liquid water transport mechanism in the porous media - This is likely dependent on the hydrophobicity / hydrophilicity of the porous media (GDL or catalyst layer).
- A more accurate description of the variation of capillary pressure with saturation in the catalyst layer and gas diffusion media.
- The variation of the permeability of the catalyst layer and gas diffusion layer to liquid water as a function of saturation.
- Clarification of the liquid water transport mechanism within the gas channels.

5 Numerical Modeling Techniques

In this section, the finite element model geometry for both the two-dimensional and three-dimensional models is introduced along with a discussion of the finite element mesh. Numerical considerations related to the computational solution of the set of mathematical equations describing a hydrogen / air PEMFC are also discussed including: the solution method employed by the solver, the required form of the equations (specific to the CFD solver), numerical manipulation of the equations in accordance with the single solution domain approach, techniques for controlling numerical instabilities, and solution time.

5.1 Model Geometry

5.1.1 Three-dimensional geometry

Figure 5.1 shows the three-dimensional geometry used in the computational model. The dimensions of each of the components for the base case are listed in Table 5.1. In addition to the components one would expect to see in a PEMFC, there are two additional components referred to in Table 5.1 as the anode and cathode special regions (regions J and K in Figure 5.1). These are actually thin sections of the polymer membrane and have unique properties with respect to the liquid water and gas species transport equations. The role of the special regions is related to the numerical characteristics of the single solution domain formulation used in the model and will be discussed in detail in the next section. The collector plates are included in the geometry but not actually meshed.

The base case model geometry is based on the test fixture and the test MEA used for model validation. The test fixture was manufactured by Fuel Cell Technologies, Inc., the gas diffusion layers are single sided ELAT^{TM} manufactured by De Nora, the membrane is Nafion$^{®}$ 112 manufactured by du Pont, and the catalyst layers were made at Virginia Tech using carbon supported catalyst purchased from De Nora (E-Tek).

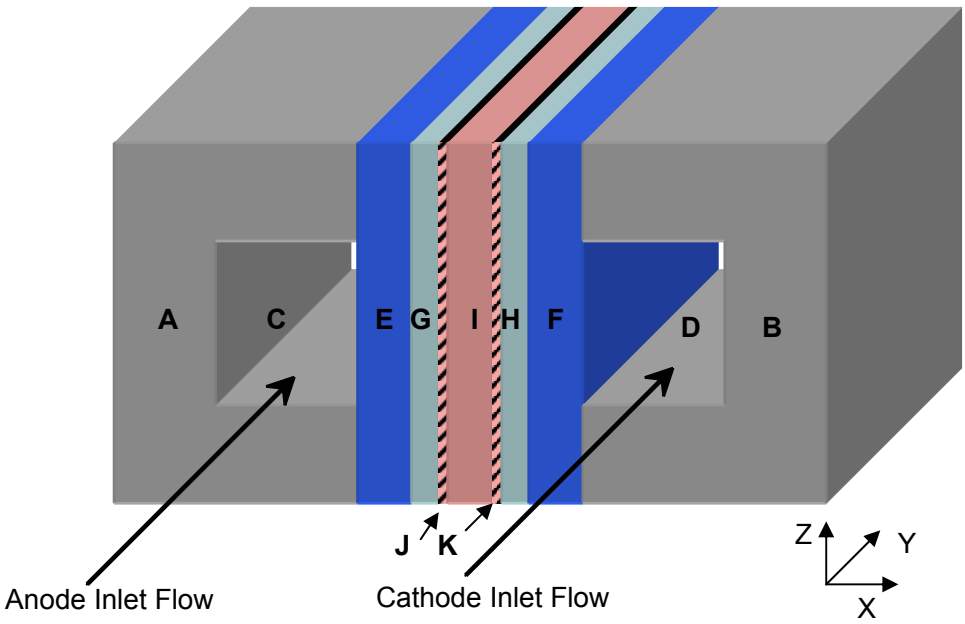

Figure 5.1 The three-dimensional model geometry (components not to scale).

Table 5.1 Geometric information for each component of the base case PEMFC model.

Component		X length, mm	Y length, mm	Z length, mm
Anode collector plate	A	15	60	2
Cathode collector plate	B	15	60	2
Anode gas channel	C	1	60	1
Cathode gas channel	D	1	60	1
Anode GDL	E	0.254	60	2
Cathode GDL	F	0.254	60	2
Anode catalyst layer	G	0.013	60	2
Cathode catalyst layer	H	0.013	60	2
Membrane	I	0.051	60	2
Anode special region	J	0.001	60	2
Cathode special region	K	0.001	60	2
Total	-	2.587	60	2

The finite element mesh for the 3D geometry consists of a total of 101,000 eight-node hexahedral elements (109,252 nodes). Table 5.2 details the mesh structure of each of the fuel cell components. Biased meshing is used in regions where large gradients in the solution variable are likely to exist, such as within the catalyst layers. The geometry and finite element mesh were created using FEMAP pre and post-processing software from EDS [35].

Table 5.2 Details of the mesh structure for each component of the base case PEMFC model.

Component		X direction	Y direction	Z direction
Anode collector plate	A	-	-	-
Cathode collector plate	B	-	-	-
Anode gas channel	C	20	25	20
Cathode gas channel	D	20	25	20
Anode GDL	E	17	25	40
Cathode GDL	F	17	25	40
Anode catalyst layer	G	12	25	40
Cathode catalyst layer	H	12	25	40
Membrane	I	15	25	40
Anode special region	J	4	25	40
Cathode special region	K	4	25	40
Total	-		101,000	

5.1.2 The Two-Dimensional Model Geometry

The two-dimensional geometry is a cross section of the three-dimensional geometry and is illustrated in Figure 5.2 and Figure 5.3. As mentioned in Section 3, the collector plates are not explicitly included in the 2D model. The details of the geometry are identical to those of the 3D model in the X and Y directions as given in Table 5.1. The mesh for the 2D model uses 4-node quadrilateral elements. The details of the 2D model mesh for the base case are identical to those of the 3D model in the X and Y directions as given in Table 5.2.

A mesh independence study was performed on the 2D model to determine the minimum number of elements required for the model to accurately solve the individual equations over the solution domain (not violate any conservation laws). This study involved creating and solving a base model containing relatively few elements. Another model with double the number of elements was then solved, and the solutions compared. This was done until the solution changed by less than 2% when the number of elements was doubled. At this point the model was assumed to be mesh independent. The minimum number of elements determined with the mesh independence study was a factor in constructing the mesh for both the 2D and 3D geometries.

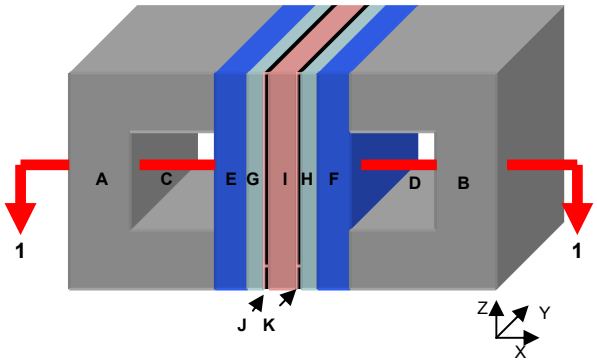

Figure 5.2 The 3D geometry showing the section used for the 2D geometry.

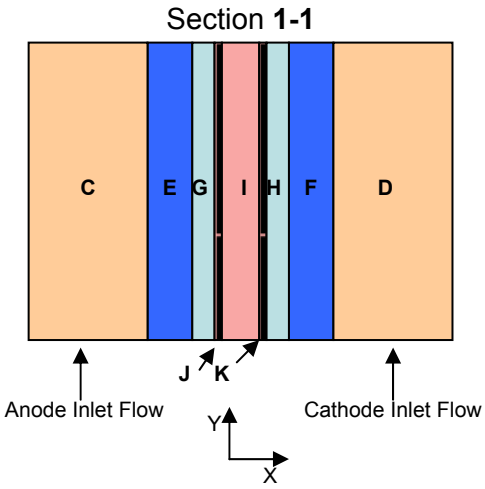

Figure 5.3 The 2D PEMFC model geometry.

5.2 Numerical Techniques

5.2.1 Solution procedure

The set of governing equations is solved with the computational fluid dynamics solver CFDesign™ [36], which is based on the finite element method. The solution process takes place as follows and is illustrated in Figure 5.4:

- The geometry, boundary conditions, initial conditions, and solution control data are read. Properties and closure relations are calculated based on the initial values specified for the solution variables.
- Each of the equations governing transport in a PEMFC, defined as partial differential equations in Section 3, is converted into a set of algebraic equations defined at every node in the model.
- The set of algebraic equations for each transport equation is rearranged into a matrix formulation as given by Eq. (5.1).
- A matrix solver executes a preset number of *internal* iterations to calculate the value of each solution variable (dependent variable of the transport equation) at every node. This is done sequentially, one equation at a time.
- Once a solution has been calculated for all of the transport equations, the solver recalculates property values and closure relations based on this solution and then proceeds to the next global iteration. The process then repeats for the specified number of global iterations. The number of global iterations is set to ensure convergence of all of the solution variables. The number of global iterations required for convergence is determined from a prior analysis, the sole purpose of which is to determine the number of iterations needed for each of the solution variables to converge. For the model presented in this work, 2,000 global iterations are needed to reach a converged solution; a converged solution being one that changes by less than 1% over the span of 500 iterations.
- Once all of the global iterations have been completed, the final solution is output to the postprocessor.

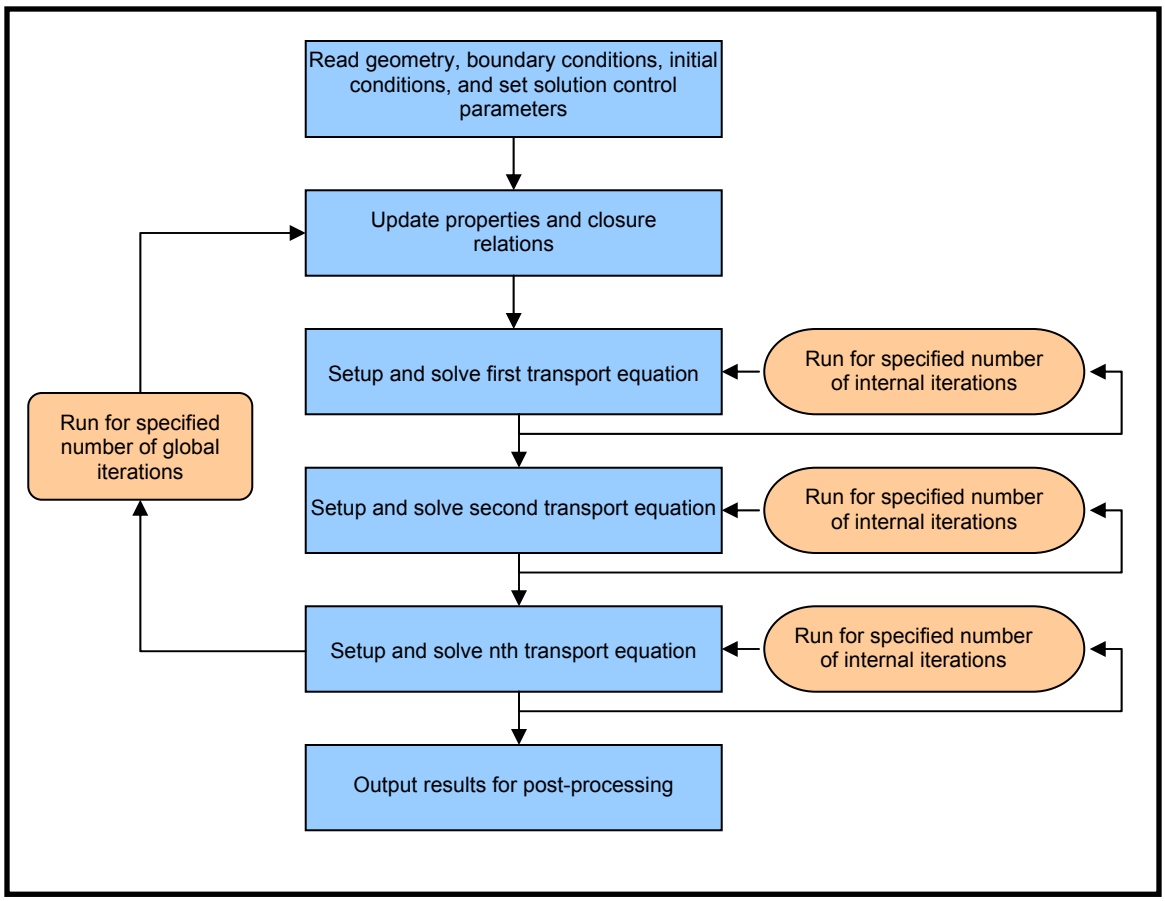

Figure 5.4 The computational solution process.

The matrix formulation of a given transport equation over all of the nodes in the solution domain is expressed as

$$A_{ii}\varphi_i + \sum_{i \neq j} A_{ij}\varphi_j = F_i \tag{5.1}$$

where A_{ij} is the matrix of coefficients (diffusive and advective terms), φ, is the value of the dependent variable at any given node i on the diagonal and j otherwise, and F_i is the load vector, which contains the source terms and boundary conditions [36]. The governing equations are input to the CFD solver in the form given by Eq. (5.2).

$$\rho u_x \frac{\partial \varphi}{\partial x} + \rho u_y \frac{\partial \varphi}{\partial y} + \rho u_z \frac{\partial \varphi}{\partial z} = \frac{\partial}{\partial x}\left(D_\varphi \frac{\partial \varphi}{\partial x}\right) + \frac{\partial}{\partial y}\left(D_\phi \frac{\partial \varphi}{\partial y}\right) + \frac{\partial}{\partial z}\left(D_\varphi \frac{\partial \varphi}{\partial z}\right) + S_\varphi \tag{5.2}$$

In Eq. (5.2), φ is the dependent variable. The group of terms on the left side accounts for transport by advection. The first three terms on the right side account for transport by

diffusion. Any term that cannot be written in the form of an advective or diffusive term is considered to be a source term, S_φ. All user-specified transport equations (all equations except for the conservation of mass and momentum) must be input in the form shown in Eq. (5.2) in order to be recognized by the CFD solver.

5.2.2 The single solution domain

The computational model of a PEMFC presented in this work is based on the solution of the governing transport equations over a single solution domain. The choice of the single solution domain allows for all of the equations to be solved at once over the entire model, as opposed to dividing the model into sub-domains, which would require the specification of interface conditions. One of the requirements of the single domain formulation is that all of the transport equations are solved in every component of the PEMFC, even if the transported quantity does not physically exist in that component. For instance, the equation for the transport of water dissolved in the polymer phase of the catalyst layers, special regions, and membrane is also solved in the gas diffusion layers where there is no polymer phase and, therefore, dissolved water cannot physically exist. The challenge is to solve each transport equation in every component and still retain a model that is physically realistic and does not violate mass conservation. This is accomplished by controlling certain aspects of the numerical formulation of the model.

Figure 5.5 is an illustration of where, within the PEMFC solution domain, each of the transported quantities physically exists. From Figure 5.5 it is evident that dissolved water exists only in the catalyst layers and the membrane. To conserve mass, dissolved water must only be transported within the catalyst layers, special regions, and membrane; it must not be transported through the neighboring gas diffusion layers. In general, an effective way to prevent a quantity from being transported *through* a component where it does not physically exist, e.g. dissolved water in the gas diffusion layers, is to prevent the quantity from being transported *into* the component. This is done by eliminating the flux of the quantity, both advective and diffusive, across the boundary into the component where it does not physically exist. To eliminate the diffusive flux into a component, the diffusion coefficient of the

transported quantity within the component is set either to a very small value (~1 x 10^{-20}) or to zero [37]. Likewise, the advective flux can be eliminated by creating a variable that multiplies the advective term in the transport equation by zero within the component(s) where the quantity is not physically valid. Another approach, which has the same result, is to mesh any components where advection is not desired with solid finite elements. The CFD solver outputs a velocity of zero within solid elements by default, hence eliminating transport by advection.

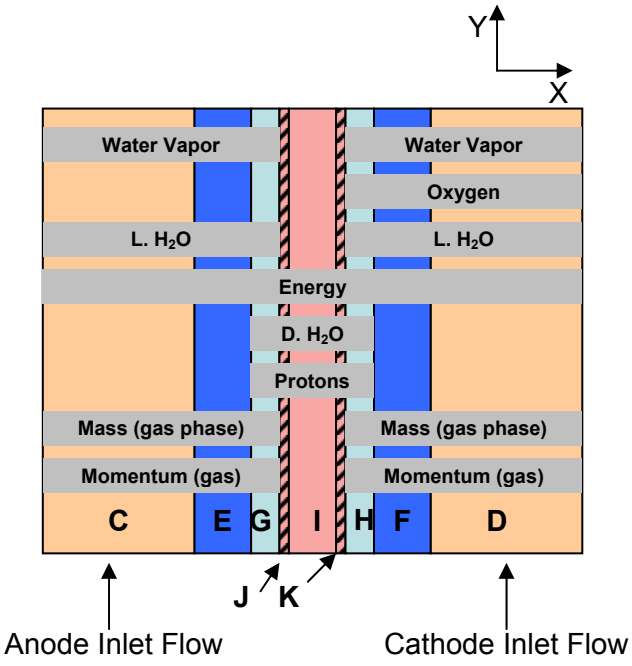

Figure 5.5 Components in which the transported quantities physically exist.

Care must be taken to ensure that, once the flux of a quantity into a region where it is not physically valid is eliminated, that the numerical value of the quantity is forced to zero. For example, it is possible to eliminate the flux of oxygen into the membrane, but that does not necessarily mean that the solution to the oxygen equation will be zero. This results from the fact that the solution at any given node in the finite element model is dependent on the solution at the neighboring nodes; if a node on the boundary of the cathode catalyst layer and the cathode special region has a non-zero value for the oxygen mass fraction, it stands to reason that some of the nodes in the special region will have a non-zero oxygen mass fraction even though there is no flux of oxygen into the special region. A large source term (1 x 10^{30})

added to the diagonal of the matrix of coefficients, $A_{ij,}$ in Eq. (5.1) is used to force a quantity to have a value of zero in the region(s) where it does not physically exist [37]. The only requirement for this method to be effective is that the value added to the diagonal is much larger than any of the other values on the diagonal and also much larger than the values in the load vector, F_i.

With regard to specific equations, from Figure 5.5 it is evident that the gas species equations as well as the liquid water transport equation are not valid in the special regions or in the membrane components of the PEMFC. From the discussion above, it follows that the flux due to diffusion and advection associated with these quantities must be eliminated at the boundary of the catalyst layers and special regions. The advection of gas species into the special regions is prevented by defining the finite elements within these regions to be solid, with regard to their interaction with the flow solver. The flow solver used in CFDesign™ will output a zero value for velocity within regions that have been meshed with elements defined in the GUI to be solids. This results in the elimination of the advective *gas* flux into these regions. The advection of *liquid* water is prevented by creating a variable that multiplies the advective term in the liquid water transport equation by zero in the special regions and in the membrane. Elimination of the diffusion of both the gas species and liquid water into the special regions is accomplished by setting the diffusion coefficients for the appropriate transport equations to a value near zero within the special regions. The sole purpose of the special regions is to provide a region where both the advective and diffusive terms (for gas and liquid species) can be forced to zero; they are identical to the membrane with respect to the transport of protons and dissolved water. Within the membrane, a large source term is added to the diagonals of the gas species and liquid water transport equations, forcing the values of those quantities to zero.

Water dissolved in the polymer phase of the catalyst layers and in the membrane as well as protons physically exist only within the catalyst layer and membrane. Neither of the transport equations for these quantities have advective terms, so it is not necessary to eliminate the advective flux at the boundaries between the catalyst layers and the gas diffusion layers. Transport of dissolved water by electro-osmotic drag does not occur in the gas diffusion layers or gas channels since the ionic conductivity and membrane water content are both zero in these regions. The diffusion coefficients for both dissolved water and

protons, within the gas diffusion layers, are set to a near zero value; the solutions are forced to zero within the gas channels.

The solution of the energy equation is physically valid in all components of the PEMFC.

5.2.3 Controlling numerical instabilities

The numerical solution of a set of coupled, non-linear partial differential equations inevitably requires that consideration be given to numerical instabilities, which are defined as numerical aspects of the model that hinder the solution process or prevent convergence of the solution. For this work, there are two general types of instabilities: those associated with the solution of the momentum equations and those associated with solution of the ionic charge transport equation. Both types of instabilities are dealt with using numerical techniques including inertial relaxation and iteration-based relaxation of source terms.

Numerical instabilities associated with the momentum equations result primarily from the sensitivity of these equations to any variation in the gas mixture density. In particular, if the rate of change of the gas density is too high, it is likely that the momentum equations will diverge. Changes in the gas density are caused by the consumption or production of gas species via electrochemical reaction and by phase change (liquid – vapor and dissolved – vapor). The rate at which gas species are consumed or produced is primarily dependent on the reaction rate, Eq. (3.45). The reaction rate can be controlled in two ways: by inertial relaxation of the equation for the transport of ionic charge, Eq. (3.65), and by direct, iteration-based relaxation of the reaction rate source term, R_{eff}, which is common to the source terms in the ionic charge equation as well as the gas species equations, Eqs. (3.55-3.56).

The inertial relaxation of a given transport equation is accomplished by modifying the diagonal of the coefficient matrix and the load vector in a manner that slows the change in the solution variable between global iterations. The effect is similar to that of the transient term on a non-steady state equation [36]. Equation (5.3) shows the matrix formulation for a transport equation with inertial relaxation applied.

$$\left[A_{ii} + \Delta t_{inertial}\right]\varphi_i + \sum_{i \neq j} A_{ij}\varphi_j = F_i + \Delta t_{inertial}\varphi_i^{old} \tag{5.3}$$

The relaxation term is $\Delta t_{inertial}$, and φ_i^{old} is the value of the solution variable from the previous global iteration. As the magnitude of the relaxation term is increased, the weight of the old solution on the current solution is increased, thus reducing the rate at which the solution changes between global iterations. As the solution approaches convergence, φ_i approaches φ_i^{old}, and the relaxation term has no effect on the final solution.

Iteration-based relaxation of source terms involves coupling the magnitude of the source term to the global iteration number, i.e. the magnitude of the source term increases from a small fraction of its true value to 100% of this value as the number of global iterations increases. This is accomplished by multiplying the source term in Eq. (5.4) by a relaxation variable, R_{Iter}, which is based on the hyperbolic tangent as shown in Eq. (5.5). The relaxation variable can be constructed in such a way as to change from an initial, near zero value, to a value of unity over a specified number of iterations. Figure 5.6 is a plot of the relaxation function that is applied to the reaction rate equation. The rate of approach to the final value of 1 can be controlled through the constants C_1 and C_2.

$$\rho u_x \frac{\partial \varphi}{\partial x} + \rho u_y \frac{\partial \varphi}{\partial y} + \rho u_z \frac{\partial \varphi}{\partial z} = \frac{\partial}{\partial x}\left(D_\varphi \frac{\partial \varphi}{\partial x} \right) + \frac{\partial}{\partial y}\left(D_\phi \frac{\partial \varphi}{\partial y} \right) + \frac{\partial}{\partial z}\left(D_\varphi \frac{\partial \varphi}{\partial z} \right) + R_{Iter} S_\varphi \quad (5.4)$$

$$R_{Iter} = 0.5\left[1.0 + \mathrm{Tanh}\left(C_1 N_{Iter} - C_2\right)\right] \quad (5.5)$$

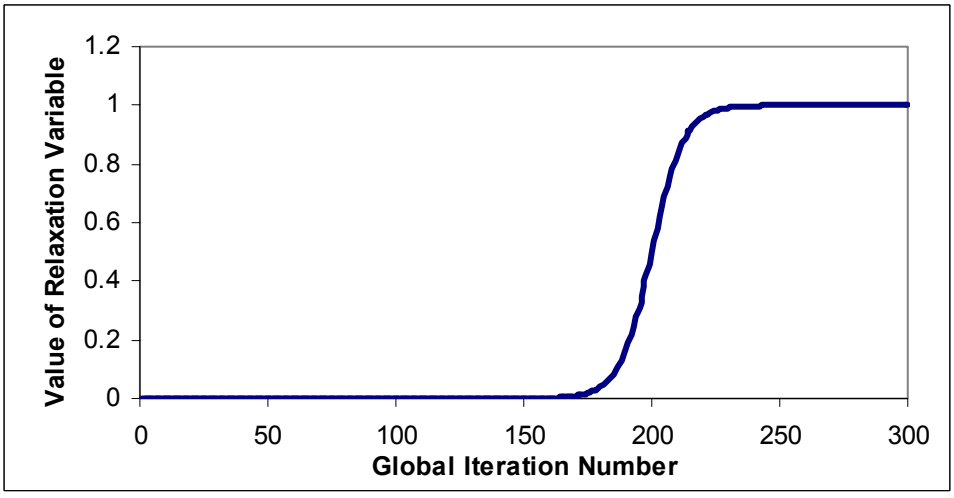

Figure 5.6 Hyperbolic, iteration-based relaxation function

In the case of Figure 5.6 (C_1=0.08 and C_2=16.0), the relaxation function starts at a value of 1.5 x 10^{-14} and converges to a value of 1.0. This particular relaxation function is used only on analyses having a total number of global iterations in excess of 1,500 to ensure that the reaction rate variable will be at its true magnitude for the majority of the iterations.

One additional level of control has to do with the modification of the mass transfer coefficients that govern the rate at which water is transferred between the vapor and dissolved phases and the vapor and liquid phases. As mentioned in Section 3, equilibrium is assumed and enforced between all three phases. This implies that all of the mass transfer processes occur very quickly. Equilibrium is achieved by making the mass transfer coefficient for the dissolved-vapor phase change, h_m, and the liquid-vapor phase change, ψ, large. Care must be taken in setting the values for both of these coefficients; if they are made too large it is possible to create large, rapid changes in the gas density, and the solution will become unstable. Equilibrium between the phases as well as solution stability can only be achieved by proper selection of both of these coefficients, which involves an iterative process.

Instabilities associated with the ionic charge transport equation occur when the reaction rate changes too rapidly, and also when the reaction rate itself varies by a large amount across the relatively thin catalyst layers. Instabilities resulting from a rapid change in reaction rate can best be controlled by iteration-based relaxation of the reaction rate source term as well as inertial relaxation of the ionic charge transport equation. Instabilities resulting from a large change in the reaction rate across the catalyst layer typically occur when the cell is running either at high current density or with a low polymer volume fraction within the catalyst layer, both of which cause an increase in the ionic potential drop across the catalyst layers. Ionic potential, φ_i, appears in the exponential term of the reaction rate equation, Eq. (3.45). Due to its placement in the exponential term, a small variation in ionic potential across the catalyst layer can result in a large variation in reaction rate, which causes the solution to become unstable. This instability is controlled by increasing the number of elements within the catalyst layer and / or by varying the mesh structure (adding more elements near the boundaries of the catalyst layer). Inertial relaxation of the ionic charge transport equation is also helpful.

5.2.4 Generating a polarization curve

In the model presented in this work, the total cell overpotential (theoretical open circuit minus the cell voltage) is specified and the current produced by the cell as well as the current distribution are calculated by the model. To generate a polarization curve, the value of the total cell overpotential is increased in steps. This causes a corresponding increase in the amount of current produced by the cell. Each step increase in overpotential requires a total of 2000 iterations in order to reach a converged solution, and that is assuming that the steps are made within the same analysis, i.e. the CFD solver is not stopped and restarted but allowed to run continuously through all of the steps. If the solver is stopped and restarted between steps, it will require increased relaxation leading to an increase in the number of iterations required to reach convergence, thus taking longer to solve.

In this work, a total of seven steps are used to generate a complete polarization curve. Each step corresponds to a specific value of total cell overpotential and, through the definition of total overpotential, a specific cell voltage. The values of total overpotential and cell voltage used in each of the steps are listed in Table 5.3.

Table 5.3 Voltage steps used to generate polarization curves.

Total overpotential, V	Cell voltage, V[1]
0.3	0.88
0.4	0.78
0.6	0.58
0.8	0.38
0.85	0.33
0.9	0.28
0.95	0.23

[1] The cell voltage is calculated for basecase conditions where the theoretical open circuit voltage is 1.18 V. The theoretical open circuit voltage is recalculated as operating conditions change.

To generate a complete polarization curve with seven steps requiring 2,000 iterations each, the model must run for a total of 14,000 iterations. During the analysis, the overpotential is changed using a ramping function similar to the hyperbolic relaxation function described in Section 5.2.3. This function allows the value of the overpotential to be

ramped up from the previous value to the new value over a span of roughly 400 iterations. The solution is converged after 2,000 iterations. The ramping function is shown in Figure 5.7.

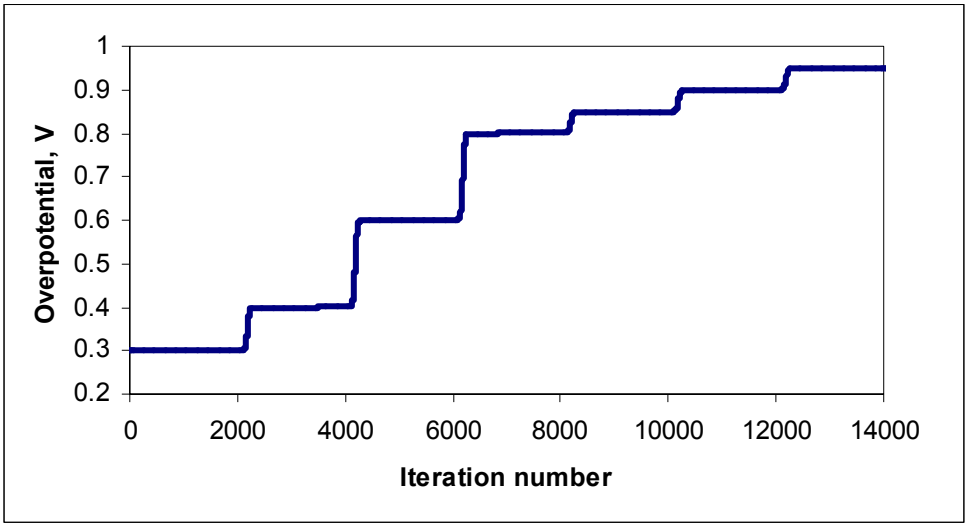

Figure 5.7 Ramping function used to adjust the total cell overpotential.

5.2.5 Solution time

The following factors determine the solution time.

- The number of equations being solved
- The degree of coupling between the equations in the model - The solution of two coupled equations can proceed no faster than the solution of the slower of the two. When relaxation is used on an equation to which all of the other equations are coupled, such as the ionic charge transport equation, the solution to the entire set of equations slows accordingly.
- The number of nodes in the solution domain
- The convergence criteria (how small the change in the solution value between iterations must be in order to achieve convergence)
- The matrix solver chosen for a given equation
- The speed of the computer

Reducing the solution time involves an adjustment of one or more of the factors listed above. The number of equations being solved in the model is more or less set and cannot be

altered without changing the nature of the model itself. Likewise, the degree of coupling among the equations cannot be altered. The minimum number of nodes is set such that the solution is stable and satisfies all of the conservation laws, principally conservation of mass. The convergence criteria has a maximum value for each equation, about three orders of magnitude less than the value of the solution variable itself, which limits its usefulness in reducing solution time.

Proper selection of the matrix solver significantly reduces the solution time. CFDesign™ has a total of seven matrix solvers to choose from. They may be categorized according to the type of matrices that they can be used to solve: symmetric, non-symmetric, or both. The two solvers currently used to solve the governing equations are the tri-diagonal matrix algorithm (TDMA) and symmeterized preconditioned conjugate gradient (SPCCG) solvers. Both can be used to solve symmetric and non-symmetric equations. The process of determining which solver is best for a given equation involves an iterative process that is outlined below:

- The model is set up first with only those transport equations required for the model to function at a minimal level. These are the mass, momentum, charge transport, and species equations.
- The species and charge transport equations are given the same solver, usually one that handles non-symmetric equations such as TDMA or SPCCG. The mass and momentum equations use the default solvers, which are not changed. A solution is attempted.
- If the solution fails (diverges), a new solver is used for either the species or charge transport equations. A solution is attempted. This process is repeated until a solver is found that works for the species and charge transport equations. At this point the number of internal iterations is adjusted to minimize convergence time while still maintaining an accurate solution.
- Once the set of equations is running well, additional equations such as dissolved water transport or energy transport are added, and the entire process is repeated.
- The process must also be repeated when changing the dimensionality of the solution domain (going from 1D to 2D or 3D).

Perhaps the most effective way to reduce solution time is to simply increase the speed of the computer used to solve the model. Currently, a single processor computer with a 2.66 GHz Pentium® 4 CPU is used to solve both the 2D and 3D models. Details related to the solution of both the 2D and 3D models are presented in Table 5.4. CFDesign™ does support parallel processing, provided that all of the processors share the same system memory. This requires that all of the processors reside in the same computer, preventing the use of a computer cluster (the term computer cluster as defined here refers to multiple computers connected together in parallel, each with its own system memory).

Table 5.4 Details of the numerical solution of the 2D and 3D models using a 2.66 GHz Pentium® 4 computer.

	2D Model	3D Model
Number of Nodes	7,808	109,252
Ram used / Ram available	169 MB/523MB	~500/532 MB
Average time per iteration, s	4.58	830.20
Average single point solution time (2,000 iterations), hours	2.54	461.22 (19 days)[1]
Time for one polarization curve (7 pts), hours	17.82	3,228.56 (133 days)[1]

[1] Estimated

Details of the solution on a slower computer, based on a 2.00 GHz Pentium 4 processor, are presented in Table 5.5. Comparing the information in Tables 5.3 and 5.4 indicates that the decrease in solution time due to an increase in processor speed is nearly linear.

Table 5.5 Details of the numerical solution of the 2D model using a 2.00 GHz Pentium® 4 computer.

	2D Model
Number of Nodes	7,808
Ram used / Ram available	169 MB/523MB
Average time per iteration, s	5.71
Average single solution time (2000 iterations), hours	3.17
Time for one polarization curve (6 pts), hours	22.20

6 Results and Discussion

In this section, the validation of the computational model with experimental data is discussed. In addition, results are presented for simulations based on both the two-dimensional and three-dimensional model geometries. Parametric studies are also presented and show, among other things, the importance of water transport with regard to fuel cell performance and the sensitivity of the model to variations in certain parameters.

6.1 Model Validation

Model validation involves the comparison of model results with experimental data, primarily for the purpose of establishing confidence in the model. Once the model is shown to be able to adequately predict the performance of the experimental fuel cell, given the same operating conditions, the model is assumed to be fundamentally accurate. The process of model validation involves the following steps.

- Create and characterize the test fuel cell (MEA). This process is discussed in Section 4.
- Construct the experimental test setup including: reactant supply, humidifiers, electronic load, data acquisition, etc.
- Gather experimental data for the test cell over a range of operating conditions.
- Input identical conditions to the model and compare the results with the experimental data. This step involves an iterative process, called tuning, where some of the model parameters are varied in order to bring the model results into closer agreement with the experimental data. The parameters that are varied are those for which sufficient empirical data is not available, thus causing their actual numerical values to be uncertain.

6.1.1 Experimental test setup

A schematic of the experimental test setup is shown in Figure 6.1. The entire apparatus consists of the following components:

- Reactant gas supply and mass flow controllers
- Dew point humidifiers
- Heated lines leading from the humidifiers to the test fuel cell
- A fuel cell test fixture with an active area of 5 cm^2
- Back pressure valves and water traps attached to the test fixture exhaust
- An electronic load
- A data acquisition and electronic control system / interface
- Temperature controllers

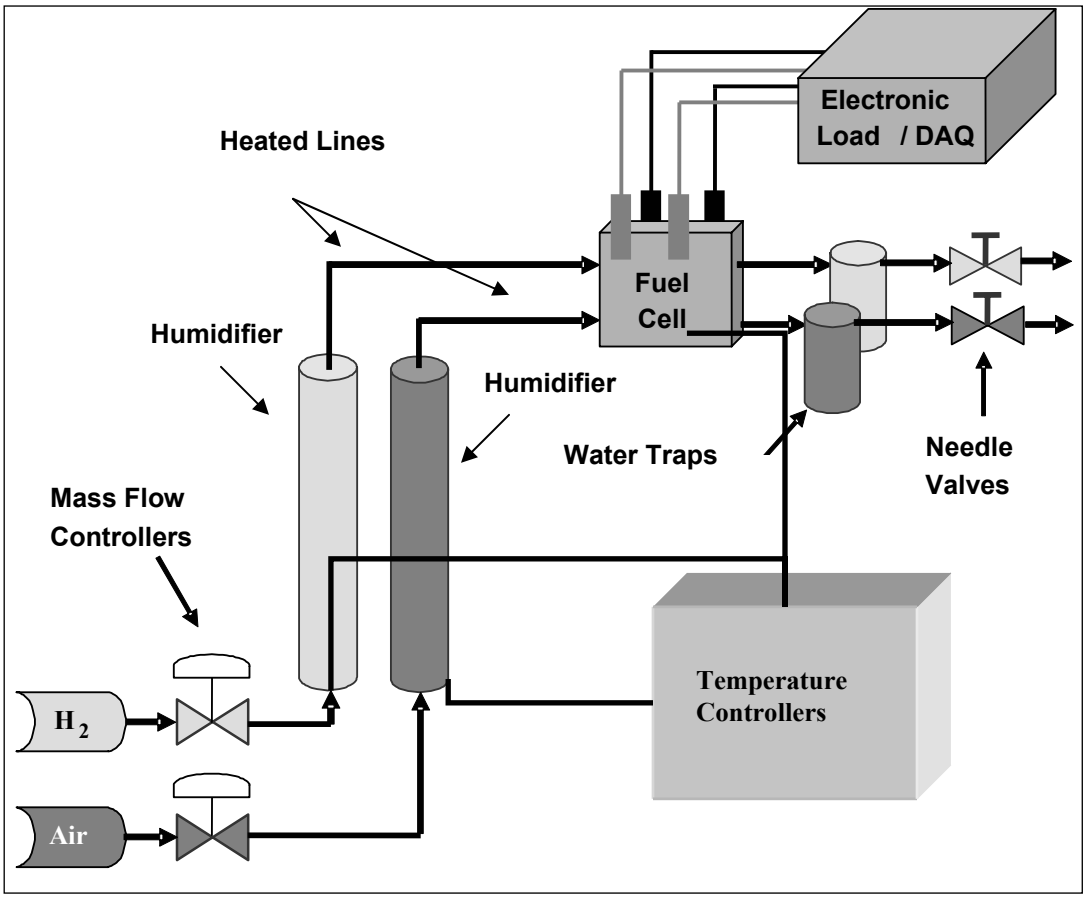

Figure 6.1 Test setup schematic [32].

Reactants (humid hydrogen and air) enter the system through the mass flow controllers, which are electronically controlled using LabView™. The reactants then flow through the humidifiers. The reactants emerge from the humidifiers fully saturated at the humidifier temperature. The heated lines are set to a temperature higher than that of the humidifiers, to prevent condensation of water from the reactant streams. The cell temperature is also electronically controlled and, along with the temperature of the humidifiers, can be used to control reactant relative humidity. The loading of the cell is controlled by a DynaLoad™ variable electronic load. Typically, a voltage is imposed on the cell and the load varied to maintain it. The LabView™ based data acquisition system can be used to automatically generate fuel cell polarization curves as well as perform current interrupt testing, with the addition of an external oscilloscope. The back pressure valves are not true back pressure regulators but rather needle valves that are manually set to achieve a given back pressure on the cell. The water traps are purged manually.

6.1.2 Fuel cell testing

All of the fuel cell testing was performed on a single MEA, fabricated at Virginia Tech, the properties of which are discussed in Section 4. Before beginning the tests, the MEA was assembled into the fuel cell test fixture and conditioned for 48 hours. The conditioning procedure involved running the cell at 80 C with fully humidified reactants at ambient exhaust pressure, while imposing a cell voltage of 0.5 V. The stoichiometric ratio for both reactant streams was maintained at about 5 (relative to a current density of 1 A/cm^2). The duration of the conditioning period is set by the amount of time required for the current produced by the cell at 0.5 V to reach a steady state value. Testing can begin only when the cell is fully conditioned.

The tests performed for model validation involved varying certain cell operating conditions and then recording a polarization curve. The following tests were performed, and the results can be found in Appendix B:

- Variable inlet pressure - Data was taken at nominal anode and cathode inlet pressures of 0, 10, 20, and 30 psig.

- Variable cell temperature - Data was taken at cell temperatures of 40, 60, and 80 C.
- Variable anode relative humidity - Data was taken at anode relative humidity values of 50%, 75%, and 100%.
- Variable cathode stoichiometric ratio - Data was taken at cathode stoichiometric ratios of 2.0, 3.0, and 5.0.
- Variable anode stoichiometric ratio - Data was taken at anode stoichiometric ratios of 1.3, 3.0, and 5.0.

The best performance achieved by the test cell was under fully humidified conditions at a temperature of 80 C. The inlet pressure for both the hydrogen and air was 30 psig, and the stoichiometric ratio for both reactant streams was 5.0. The baseline test data was taken under identical conditions with the exception of inlet pressure, which was set to 5.92 psig on the cathode and 0.79 psig on the anode (the exhaust was at ambient pressure). Polarization curves for both operating points are shown in Figure 6.2.

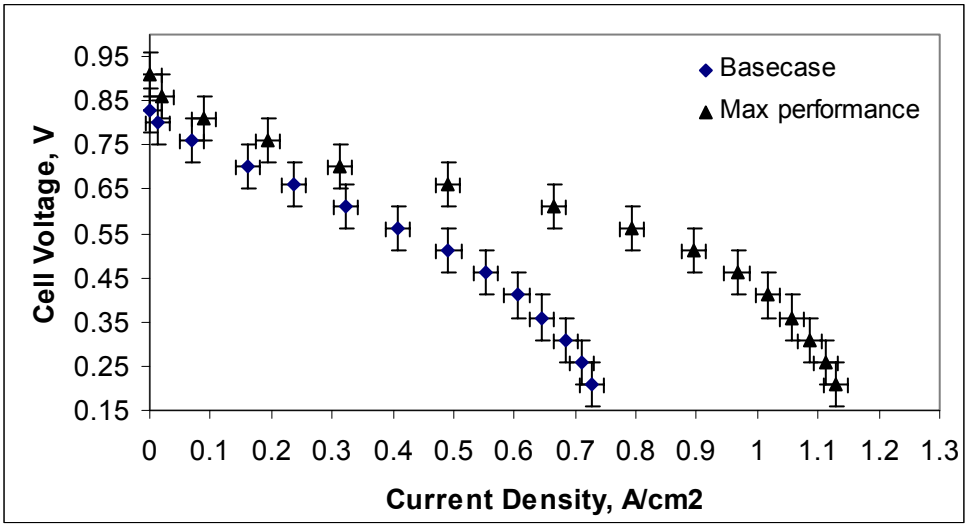

Figure 6.2 Polarization curves for the test cell at basecase conditions and maximum performance conditions. Error bars are shown indicating the uncertainty associated with the voltage and current measurements.

6.1.3 Tuning the model

When the model is first run under the same conditions as the test, it is possible that the results output from the model, usually in the form of a polarization curve, will not match the data from the test. This discrepancy is due mainly to the fact that some of the parameters on which the model is based have considerable uncertainty. For instance, the exact value of the exchange current density of the test cell is not known. It must be estimated from published experimental work. Typically, the value implemented in the model is estimated from a range of possible values for this parameter reported in the literature. By varying the value used for exchange current density, along with other estimated parameters, the model results can be brought into closer agreement with the test data. This process is called tuning the model. When tuning the model, *only those parameters for which the true values are uncertain are varied, and values are maintained within ranges reported in the literature*. Any experimental work that can be done to more closely estimate the value of a given parameter increases the accuracy of the model.

The process of tuning can require a large number of iterations, in order to bring the model results into agreement with the test data. To facilitate this process, a one-dimensional model is used, which although is not as comprehensive as the two dimensional model formulation, does include the transport phenomena thought to have the greatest impact on fuel cell performance, i.e. the transport of liquid water, gas species, and ionic charge. The principle benefit of the 1D model is that, due to the fact that it has relatively few finite elements, it can be solved very quickly in comparison with the 2D and 3D models. The one-dimensional model geometry is shown in Figure 6.3. It can be thought of as a slice across the 2D model discussed in Section 5.1. The geometry consists of 81 elements in the x direction and 1 element in the y direction. The 1D model does not include the gas channels.

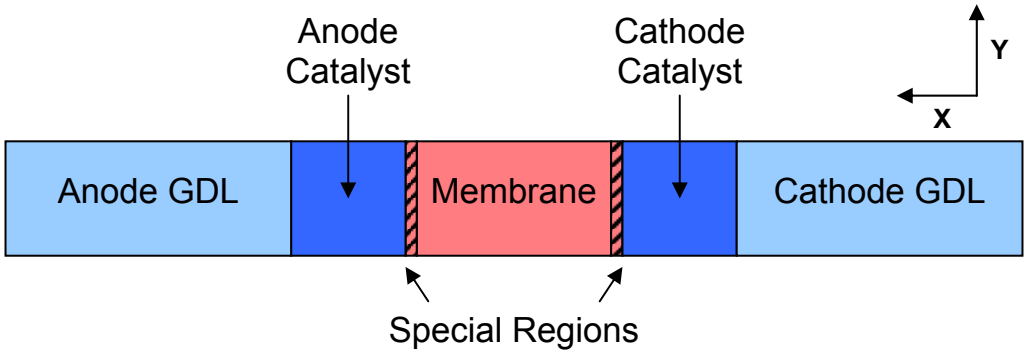

Figure 6.3 One-dimensional model geometry used for model tuning.

The governing equations included in the formulation for the one-dimensional model are: the transport of oxygen, hydrogen, and water vapor, the transport of liquid water, and ionic charge transport. The energy equation and the dissolved water equation are omitted, and the model operates at a constant temperature and membrane water content. Although the dissolved water transport equation is not included, the effect of electro-osmotic drag on water accumulation at the cathode is included via a source term in the liquid water transport equation.

6.1.4 Model validation at base case conditions

The parameters that are adjusted in the tuning process are given in Table 6.1 along with the range over which they may be varied. This range is based on data available in the literature for each of the parameters. Table 6.2 contains a listing of the boundary conditions and initial conditions included in the base case model. Once tuning is completed with the 1D model, i.e. the model results are in close agreement with the experimental data, the "tuned" parameters are input to the 2D model and a polarization curve is generated. Often, the curve generated with the 2D model is in close agreement with the results generated using the 1D model, although this is not always the case. In some cases the 2D model results, predicted with parameters tuned using the 1D model, will not be in agreement with the experimental results, thus requiring additional iterations of the tuning process. In general, the 1D model is most useful not in predicting what the actual output of the 2D model will be, but rather in predicting how changing a given parameter will affect the overall trend seen in a polarization curve. For example, Figure 6.4 presents results from the 1D model showing how a change

in the agglomerate characteristic length affects cell performance. Figure 6.5 presents 1D results showing how a change in the tortuosity of the GDL affects cell performance.

Table 6.1 Parameters that are varied to tune the model.

Parameter	Range	Base Case Value
Cathode exchange Current density	$5.0\ E^{-10} – 6.0\ E^{-9}$ A/mm^2	$4.0\ E^{-9}$ A/mm^2
Charge transfer coefficient for oxygen reduction reaction	0.53 – 0.64	0.64
Pt surface area per catalyst layer volume	3000 – 10000 mm^2/mm^3	7000 mm^2/mm^3
Tortuosity of the GDL	4.0-12.0	8.0
Agglomerate characteristic length	0.2 μm – 1.0 μm	1.0 μm
Diffusion coefficient for oxygen in Nafion®	$1.0\ E^{-4} – 4.0\ E^{-4}$ mm^2/s	$2.0\ E^{-4}$ mm^2/s
Magnitude of the liquid water diffusion coefficient[1]	0.0014 – 0.00042 mm^2/s	0.0007 mm^2/s

[1]The range given for the liquid water diffusion coefficient corresponds to the average value of the coefficient for saturation values ranging from zero to one.

Table 6.2 Boundary and initial conditions for the base case model[1].

Variable	Boundary condition	Initial condition	Point of application
Velocity at the cathode	8,932 mm/s	N/A	Gas channel inlet
Velocity at the anode	6,100 mm/s	N/A	Gas channel inlet
Pressure	5.92 psig	0.69 psig	Outlet of gas channels
Oxygen mass fraction	0.18	0.18	Cathode gas channel inlet
Water vapor mass fraction on the anode	0.88	0.88	Anode gas channel inlet
Water vapor mass fraction on the cathode	0.24	0.24	Cathode gas channel inlet
Liquid water saturation	0	0	Anode and cathode gas channel inlets
Dissolved water concentration	3.54E-5 mol/mm^3	3.54E-5 mol/mm^3	Catalyst layers and membrane
Ionic potential	Zero flux	0 V	Outer boundary
Temperature	353 K	353 K	All external boundaries and gas channel inlets

[1]The external model boundary, with the exception of flow inlets and outlets, is considered to have a zero flux boundary condition for all transported quantities except for energy.

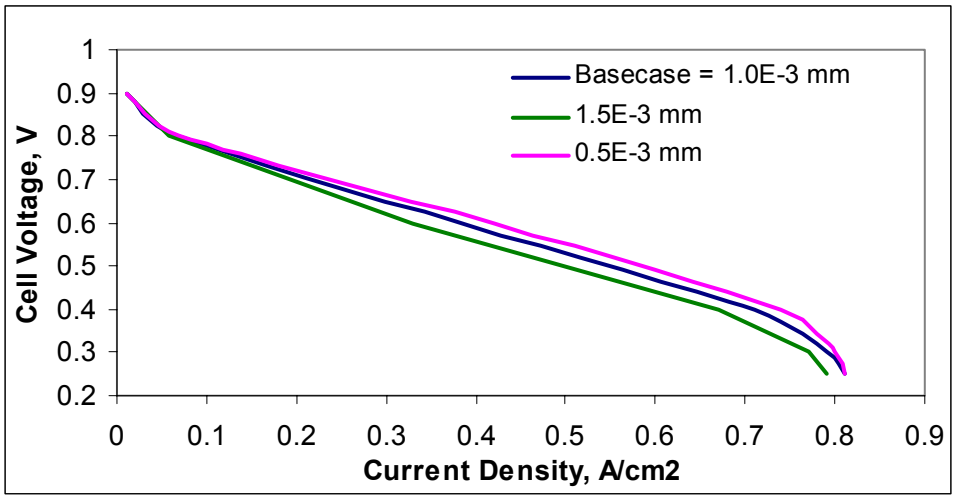

Figure 6.4 Decreasing the characteristic length of the agglomerates lowers diffusive resistance within the catalyst and allows more current to be produced at a given voltage. It does not affect the limiting current significantly (results from the 1D model).

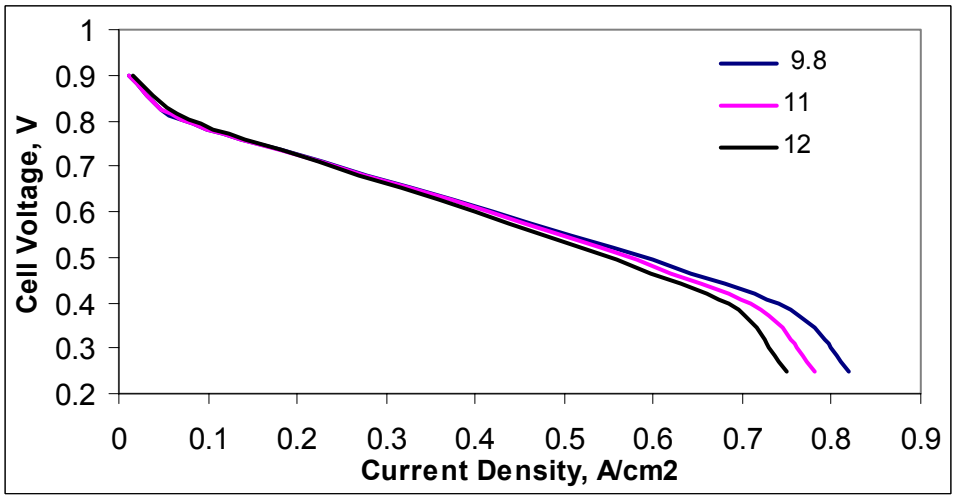

Figure 6.5 Increasing the tortuosity of the GDL causes the limiting current to decrease due to increased resistance to reactant diffusion. It does not affect performance significantly outside of the mass transport limited regime (results from the 1D model).

Both the agglomerate characteristic length and the GDL tortuosity are linked to species transport through the cell. However, the way in which each of these parameters influences performance differs somewhat. A change in tortuosity will cause a shift in the limiting current and not have much of an effect anywhere else along the polarization curve. A change in the agglomerate characteristic length will not affect the limiting current but will

change the amount of current produced at a given voltage in the activation and ohmic regimes. In performing these studies with the 1D model it is possible to determine how a change in any given parameter will affect the overall shape of the polarization curve. This is useful information when considering that the objective of the tuning process is to fit the shape of a polarization curve generated with the model to that defined by the experimental data. Although the results predicted by the 1D model may not always be in close numerical agreement with those predicted by the 2D and 3D models, the qualitative information is still applicable.

The best possible result of the tuning process is that the results predicted by the model agree with experimental data taken over a range of conditions, without re-tuning the model, when the conditions are varied. For instance, the model is typically tuned to closely match the experimental data at basecase conditions. The best possible outcome would be if the results generated by the model matched not only the basecase data, but also any additional data taken at conditions other than basecase. Unfortunately, this is not always the case. The models presented in this work are tuned to basecase conditions, and may need re-tuning when the conditions are changed for reasons that are discussed later in this section. Figure 6.6 shows the model results tuned to match experimental data at basecase conditions. It should be noted that the curve generated by the model was shifted slightly to the left along the current density axis to match the experimental value for the open circuit voltage. The shift, which was 12.5 mA/cm^2 at basecase, was used to account for fuel crossover effects. Fuel crossover decreases the open circuit voltage of a cell and is not explicitly included in the model.

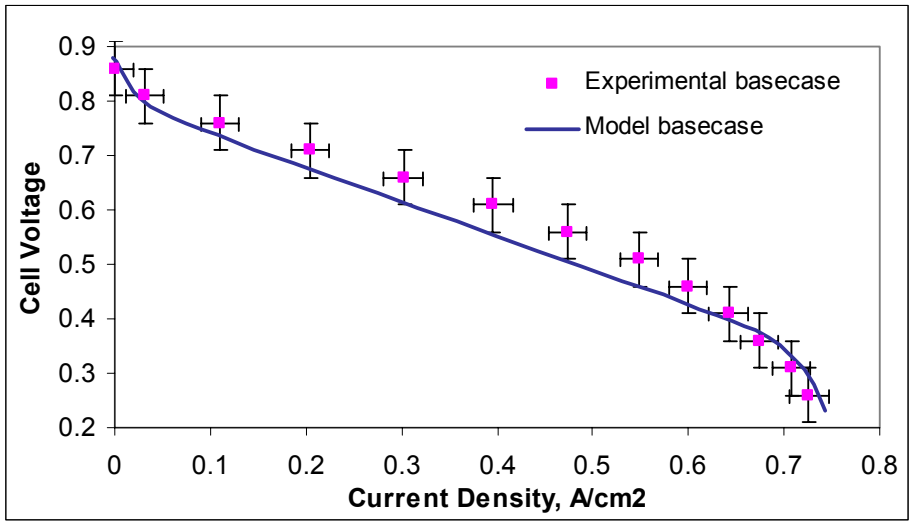

Figure 6.6 Comparison of experimental data and 2D model results at basecase conditions

The experimental data shown in Figure 6.6 include error bars that indicate the amount of uncertainty associated with both the voltage and current density measurements. It is evident that the modeling results and the experimental data are in general, but not exact, agreement over the entire load range.

6.1.5 Model validation at low anode relative humidity

Figure 6.7 shows cell performance predicted by the model *without re-tuning or adjustment of parameters*, as well as experimental data, for an anode reactant relative humidity of 50% at the gas channel inlet. Basecase conditions of 100% relative humidity are also shown. The experimental data show a slight decrease in performance over the entire operating range when the anode relative humidity is low. The model predicts that, although performance decreases in the ohmic region with low relative humidity, the limiting current should be greater. The model results make sense because at lower anode relative humidity there is less water available to hydrate the membrane, which leads to increased ohmic losses. In addition, the amount of water dragged across the MEA from the anode to cathode is reduced at low anode relative humidity, resulting in a lower liquid water saturation level at the cathode and a corresponding increase in the limiting current.

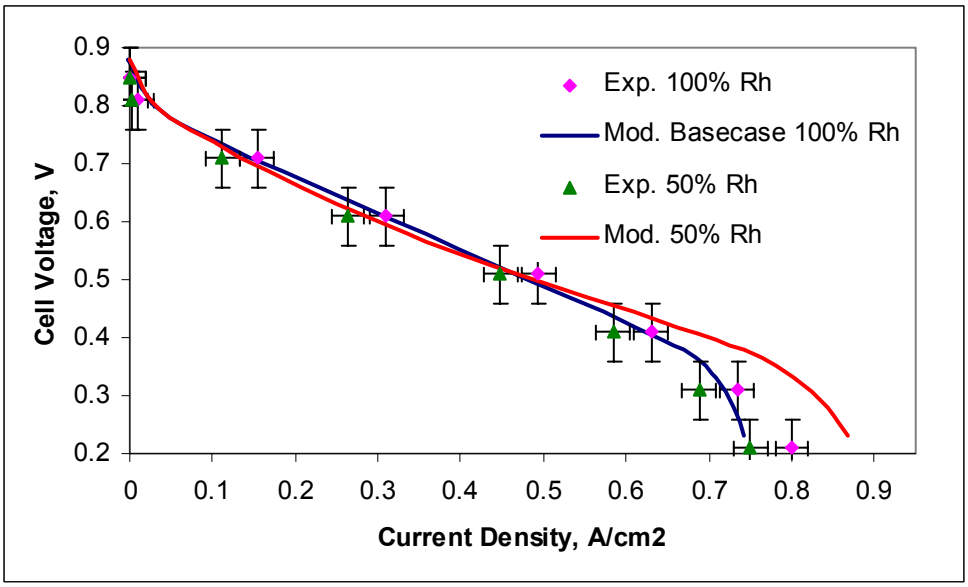

Figure 6.7 Cell performance variation with anode relative humidity.

The trends predicted by the model are consistent with other data in the literature [23] but not with the data from our experiments. This suggests two possibilities: Either the experimental data are incorrect at low voltage, or the specification of certain physical properties at low anode relative humidity is incomplete. With regard to the experimental data at low voltage, it is difficult for the electronic load used in testing to achieve high current with a very low voltage difference across the cell. Resistances in the wiring and within the load can lead to erratic operation including load faults in the low voltage region of the polarization curve. This may cause the current to be understated and prevent observation of the trend predicted by the computational model and by others [23].

With regard to the specification of physical properties, some of the properties used in the model, in particular the variation of the solubility and diffusion coefficient of hydrogen in Nafion® with a change in anode relative humidity, may be responsible for the difference between the trend seen in the data and that predicted by the model. As the relative humidity at the anode is lowered, the polymer within the anode catalyst layer is dehydrated. This may lead to a reduction in the hydrogen solubility and the hydrogen diffusion coefficient within the polymer portion of the anode catalyst layer. The result would be a reduction in the rate of transport of hydrogen through the anode agglomerates and thus a reduction in the limiting

current at low anode relative humidity. Currently, there is no experimental data available dealing with the variation of hydrogen solubility and diffusion through Nafion as a function of relative humidity or polymer water content. For this reason, both the solubility and diffusion coefficient values are assumed to be constants in the model formulation. Because these values are treated as constants, the model is not able to predict mass-transport effects related to changes in the polymer water content due to low relative humidity. It is also possible that the manner in which liquid water transport is modeled contributes to the difference in the model results and the experimental data. This possibility is discussed in more detail in the following section.

6.1.6 Model validation at low temperature

Figure 6.8 shows a comparison between the results predicted by the model and experimental data for the test cell operating at a temperature of 60 C (basecase is 80 C). The change in performance with temperature, as predicted by the model, is shown in Figure 6.9. *The model results are presented for values of the tuning parameters that are identical to the basecase values, except for the liquid water diffusion coefficient*. The capillary flow of water in the GDL is described by a diffusion model in which the diffusion coefficient is given by Eq. (3.24), repeated here for clarity. The viscosity of liquid water is 25% greater at 60 C than at 80 C and thus, as indicated by Eq. (3.24), the diffusion coefficient of liquid water is 25% less. The change in viscosity alone is not sufficient to fully account for the reduction in limiting current as temperature decreases. The diffusion coefficient is decreased by an additional 25% (a total reduction of 50% from basecase) to account for the decrease in the water removal rate from the gas channels as cell temperature is reduced. This coupling between cell temperature, cell performance, and liquid water transport is an effect that has not yet been addressed in the literature.

$$D_{WL}^{cp} = \frac{\rho_{WL} g}{\mu_{WL}} K(s) \frac{\partial P_c}{\partial s} \qquad (3.24)$$

The model predicts a decrease in performance with temperature over the entire load range, including a reduction in the limiting current. The decrease in performance in the

activation regime is attributed to a reduction in the magnitude of the exchange current density. The increased slope in the ohmic region is caused by the drop in the ionic conductivity of the polymer in the catalyst layers and membrane with temperature. The reduction in the limiting current at 60 C is indicative of increased mass transport resistance in the gas phase and is discussed in Section 4.4.

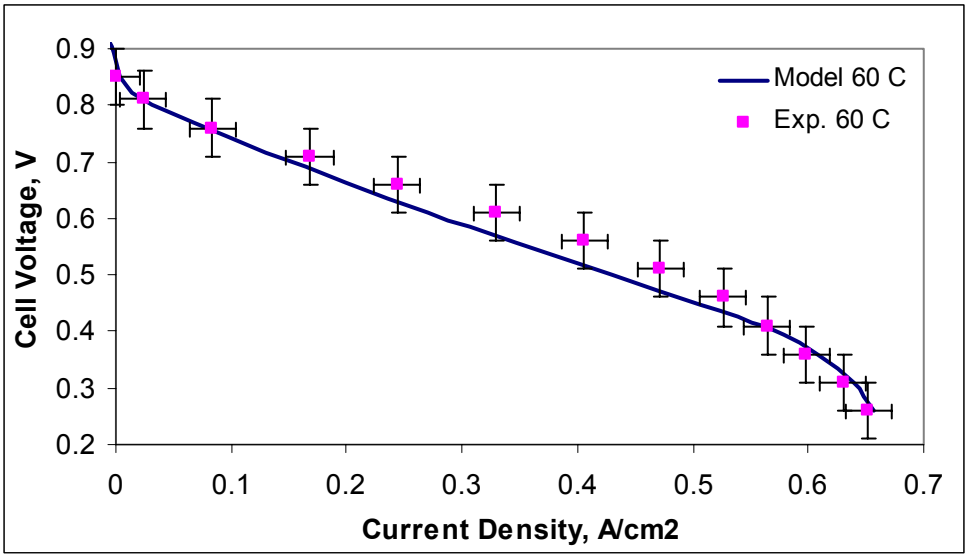

Figure 6.8 Comparison of model results and experimental data for cell performance at 60 C.

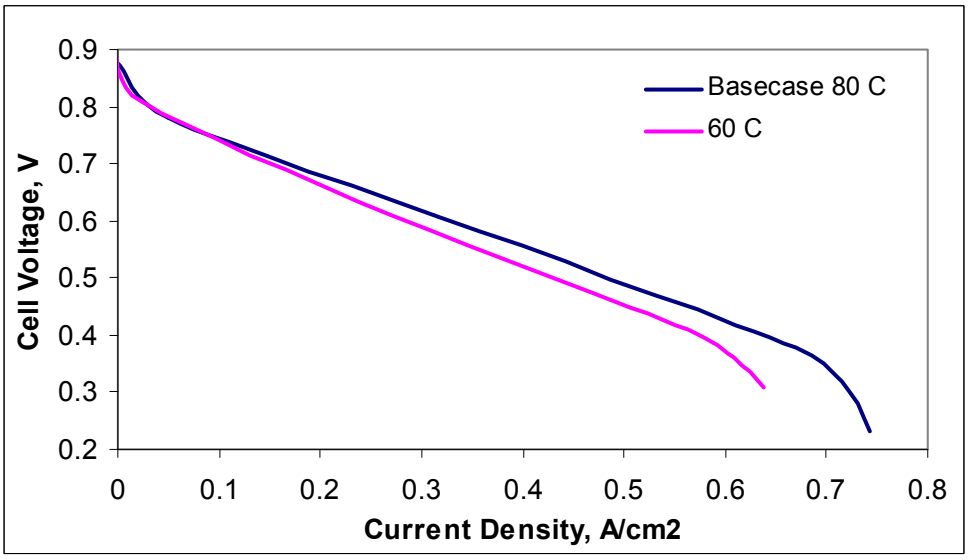

Figure 6.9 Influence of cell operating temperature on performance.

As mentioned in Section 4.4, it is likely that the increase in mass transport resistance at lower temperature is linked to how liquid water is transported through the gas channels; as the temperature is decreased, the velocity in the gas channels is reduced. This in turn leads to a decrease in the rate of water removal from the cell, which leads to more liquid water accumulation within the catalyst and gas diffusion layers and an increase in mass transport resistance. In the model presented in this work, there is currently no provision to account, explicitly, for an increase in the rate of liquid water removal from the cell with temperature. Instead, the liquid water diffusion coefficient is adjusted to simulate this effect. In the absence of this adjustment, the model correctly predicts the performance trends in the activation and ohmic regimes, but fails to predict a reduction in limiting current at 60 C.

6.1.7 Resolving differences between modeling results and experimental data

It is evident from the preceding discussion that the results predicted by the computational model are in general, but not exact, agreement with experimental data. Differences between the model results and the experimental data may be attributed to a variety of causes, including the following:

- Errors made during the experimental work - These may include reading errors on the part of the operator, equipment malfunction, erroneous recording of experimental data and test conditions. For instance, it is relatively common to misread a temperature output on a screen that displays five separate temperature readouts. Errors in the experimental procedure are also possible. The experimental data showing the variation in cell performance with anode relative humidity, Figure 6.7, was taken twice. It was found that, in the first data set, insufficient time was given to allow for re-equilibration of the cell following the change in relative humidity. The experimental procedure was modified accordingly and the test redone.
- Improper specification of the conditions for which the model results are generated - It is important that the input to the model with regard to boundary conditions such as reactant concentration, cell temperature, stoichiometric ratio, etc. be as close to the experimental conditions as possible.

- Incomplete specification of physical properties - Many of the properties used in the model must be estimated based on limited data from the literature. Often, physical property data is available for only one set of experimental conditions, which may be significantly different than the conditions of the fuel cell test. An example of this is the solubility of oxygen in Nafion®. Data can be readily obtained that shows how solubility varies with temperature at a set oxygen pressure and membrane hydration level. In a fuel cell, however, both pressure and membrane water content vary. It then becomes necessary to either extrapolate how the oxygen solubility is affected by these two parameters or to assume that oxygen solubility is constant.
- Errors made in the formulation of the mathematical model - Two types of errors are possible: unintentional errors that may include entering a mathematical relation incorrectly in the code and errors involving incorrect assumptions with regard to the physics of fuel cell operation. Unintentional errors are common, and the frequency of incidence increases as the model becomes more complex and the code more lengthy. However, debugging can eliminate these errors. Errors in the description of the governing physics of fuel cell operation can be resolved as more is learned about fuel cell operation.
- Errors associated with the numerical solution of the model - The most common of these is a model solution that has not yet converged. Results taken from such a solution will not accurately represent the physics defined in the mathematical formulation. Proper monitoring of solution progress and the specification of a sufficient number of global iterations can eliminate this type of error.

With regard to Figure 6.6, it is most likely that the differences between the model results and the experimental data result from uncertainty in the experimental data, as indicated by the error bars, as well as uncertainty associated with some of the physical properties. In addition, the results could likely be improved by a more complete description of liquid water transport, particularly within the gas channels. The diffusion coefficient for liquid water used in this model was taken from the work of Natarjan and Nguyen [8]. They determined the form of the diffusion coefficient of liquid water for a specific test cell that is physically different from the one used in this work. In order to more accurately model liquid

water transport, a relationship for the liquid water diffusion coefficient similar to that of Natarajan and Nguyen derived specifically for the test cell used in this work, is needed. Moreover, the flow of liquid water in the gas channels only insures conservation of mass. No attempt is made to describe the two-phase flow in the gas channels. Since the nature of the flow in the gas channels influences the boundaries with the porous GDL, a better description of liquid water in the gas channels would improve the model with regard to the water distribution in the GDL and catalyst layer.

6.2 Effect of transport processes on fuel cell performance

In addition to generating polarization curves, the two-dimensional computational model can be used to generate results that are helpful in investigating transport processes within the fuel cell. In particular, the results generated using the computational model(s) illustrate, much more clearly than possible with strictly experimental methods, the phenomena behind observable trends in fuel cell behavior. In this section, modeling results are presented that illustrate the connection between certain transported quantities (oxygen, water in the dissolved phase, and water in the liquid phase) and fuel cell performance.

6.2.1 Transport of oxygen

The manner in which oxygen is transported through the cell has a strong influence on overall performance. In particular, the availability of oxygen at the cathode catalyst sites influences performance across all operating regimes. In the activation regime, the local concentration of oxygen within the catalyst layers not only influences the open circuit voltage but is also a factor in determining the reaction rate itself through the exchange current density, which is concentration dependent [23]. In the ohmic and mass-transport regimes, the flow of oxygen in gaseous form to the catalyst layer and in dissolved form through the catalyst agglomerates has a significant impact on the current produced by the cell. During the normal operation of a hydrogen / air PEMFC, the limiting current is typically a function solely of the ability (or inability) of oxygen to reach the catalyst sites.

Significant resistance to oxygen flow occurs in two regions of the fuel cell: the gas diffusion layers and the catalyst layers. Figure 6.10 shows normalized oxygen mass fraction

profiles across the cathode (gas channel, GDL, and catalyst layer) at a position midway down the gas channel of the cell for three different levels of current density. The profiles have been normalized relative to the oxygen mass fraction at the interface of the GDL and gas channel. The largest drop in oxygen mass fraction occurs across the gas diffusion layer. By comparison, the drop in oxygen mass fraction across the catalyst layer, normalized relative to the oxygen mass fraction at the GDL/gas channel interface and shown in Figure 6.11, is small except at high current density. In either case, since oxygen transport across these regions is largely diffusive, the drop in mass fraction can be reduced by making the layers thinner, reducing tortuosity, increasing porosity, or facilitating the rate of liquid water removal.

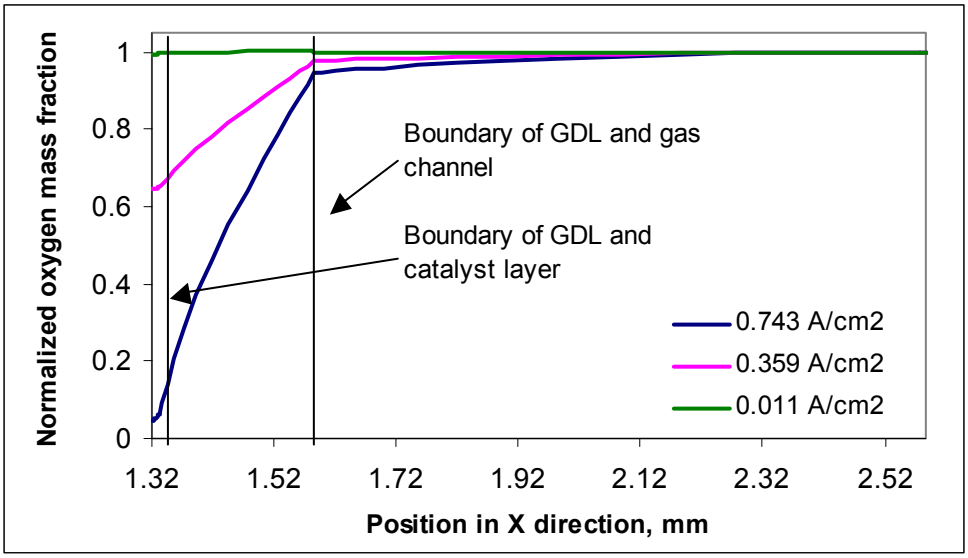

Figure 6.10 Variation in oxygen mass fraction across the cathode at basecase conditions (oxygen mass fraction normalized by the mass fraction at the GDL / gas channel interface).

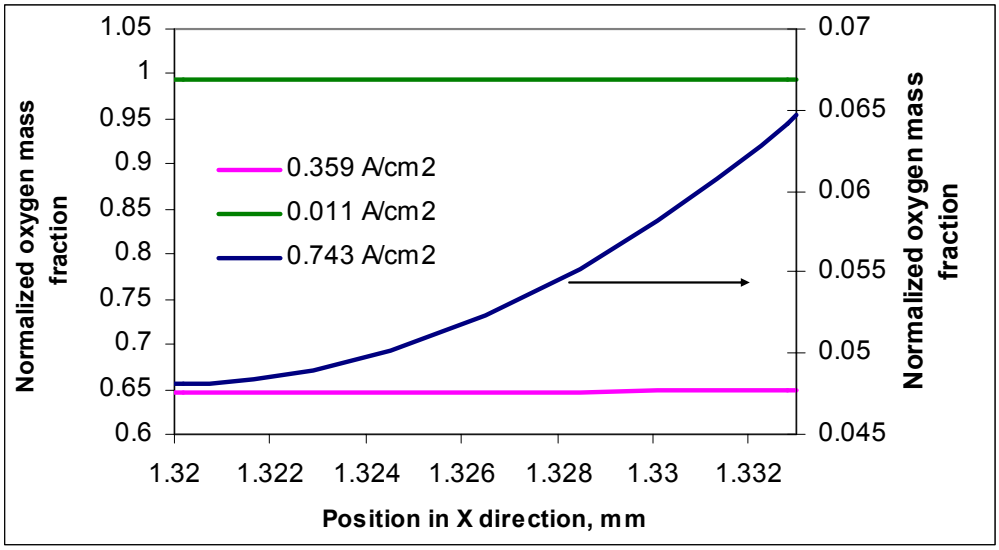

Figure 6.11 Variation in oxygen mass fraction across the cathode catalyst layer at basecase conditions (oxygen mass fraction normalized by the mass fraction at the GDL / gas channel interface).

In addition to a resistance to oxygen transport in the gas phase, the catalyst layer also adds a resistance to oxygen transport as it diffuses in dissolved form through the polymer surrounding the catalyst sites within the agglomerate structure. Although the diffusion of oxygen through the dissolved phase is not modeled explicitly, an effectiveness relation, Eq. (3.46), is used to account for its effect on the reaction rate. Similarly, at the anode, an effectiveness relationship is used to account for the effect of hydrogen diffusion through the agglomerates on reaction rate. This is discussed in Section 3.42. The transport of both hydrogen and oxygen through the polymer is principally a function of the diffusive path length (agglomerate size) and the local reactant concentration, which is a function of the gas phase concentration and the solubility of the reactant in the polymer portion of the catalyst layer. Figure 6.12 shows the variation of effectiveness through both the cathode and anode catalyst layers at a position midway down the channel. The effectiveness in the anode catalyst layer is two orders of magnitude greater than that in the cathode catalyst layer. This results from the fact that hydrogen is more soluble in and diffuses more readily through Nafion® than does oxygen. In addition, the cathode catalyst layer has a greater liquid water saturation level, which indirectly leads to a reduction in effectiveness by reducing the equilibrium concentration of oxygen at the agglomerate surface.

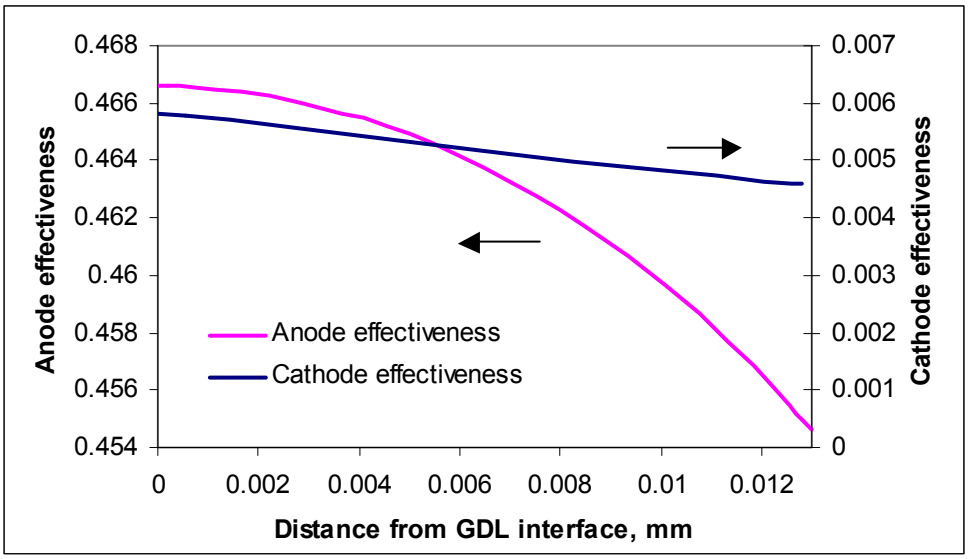

Figure 6.12 Effectiveness profiles in the anode and cathode catalyst layers for basecase conditions.

Another important aspect of oxygen transport is the drop in oxygen concentration as it flows through the fuel cell gas channels. Typically, experimental cells are run at high stoichiometric ratios on the cathode side to minimize this effect. However, even at high stoichiometries, if the current density is large enough, oxygen will be depleted enough to reduce performance down the channel. Figure 6.13 shows the oxygen variation down the channel for four different inlet stoichiometries at a cell voltage of 0.58 V. The stoichiometric ratio in each case is based on the amount of reactant, both hydrogen and air, required by a cell operating at 1 A/cm^2. The cell limiting current (which occurs at a voltage of 0.23 V) is shown in Figure 6.14 and approaches an asymptotic maximum of about 0.8 A/cm^2 as the cathode inlet stoichiometry is increased.

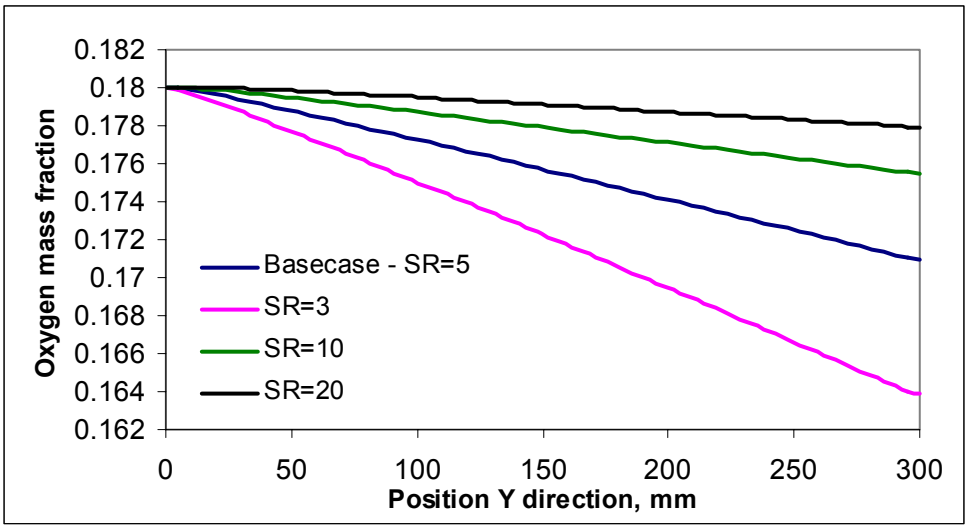

Figure 6.13 Variation of the oxygen mass fraction down the channel with inlet stoichiometric ratio. Results are evaluated at a position in the middle of the cathode gas channel (results taken at basecase conditions except for the SR). The SR is 1 at 1 A/cm^2.

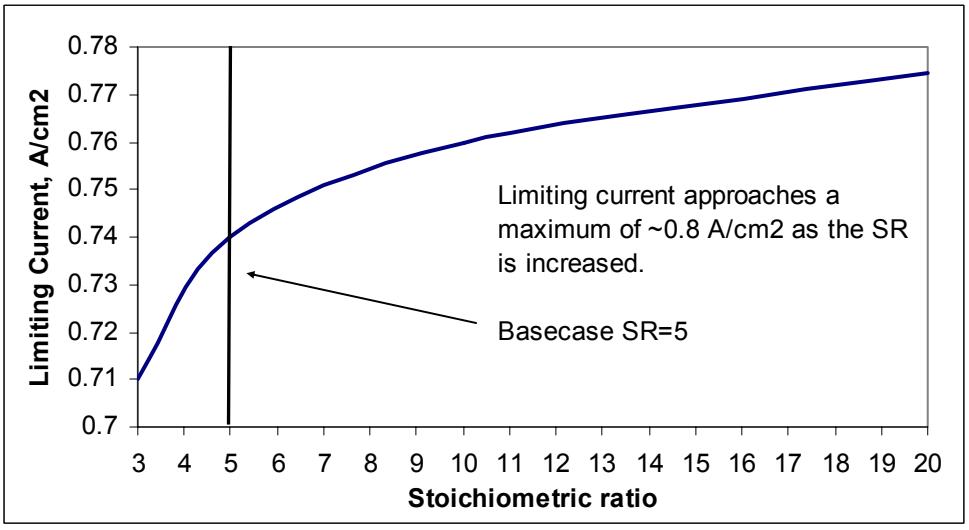

Figure 6.14 Increase in limiting current with the stoichiometric ratio (results taken at basecase conditions except for the SR). The SR is 1 at 1 A/cm^2.

6.2.2 Transport of Dissolved Water

Dissolved water transport influences the performance of a fuel cell in two principal ways: by causing variations in the ionic conductivity of the polymer portions of the catalyst layer and membrane and by moving water from the anode to the cathode, where it may

appear as liquid water and contribute to cell flooding. In the model presented in this work, water can be transported in dissolved form through the polymer by diffusion and electro-osmotic drag. In most cases, especially when the relative humidity of the reactant stream on the anode is equal to that on the cathode, electro-osmotic drag will be the dominant transport mechanism, and water will move from the anode to the cathode. This causes a decrease in the polymer water content at the anode and an increase at the cathode, leading to a corresponding decrease in ionic conductivity at the anode and an increase at the cathode. Figure 6.15 shows the distribution of polymer water content across the MEA for three levels of current density at basecase conditions. Figure 6.16 shows the corresponding ionic conductivity distribution. The ohmic losses in a fuel cell are a function of the local current density as well as the local ionic conductivity. The discontinuity in the ionic conductivity, as shown in Figure 6.16, results from the change in polymer volume fraction across the boundary between the catalyst layers and the membrane. In the catalyst layers, at base case conditions, the volume fraction of polymer is 0.24; in the membrane it is always equal to 1.0.

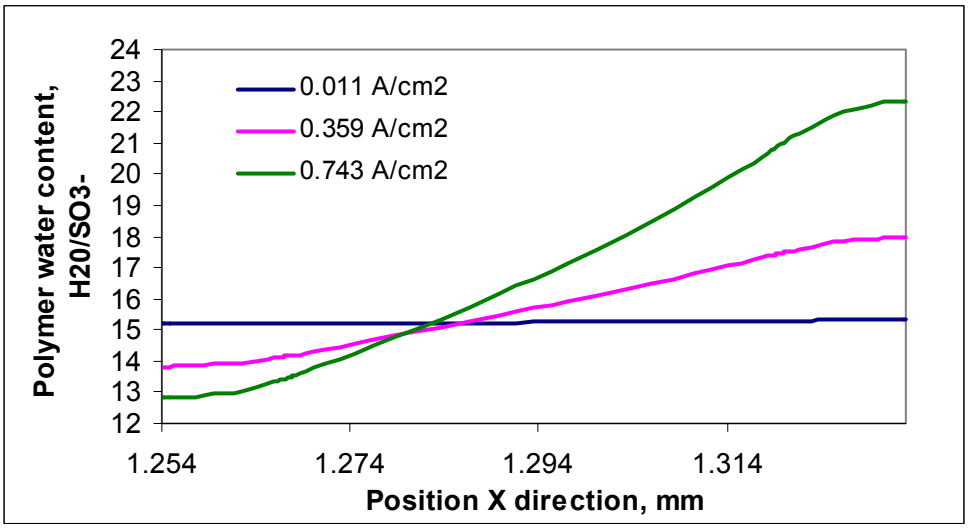

Figure 6.15 Polymer water content profiles across the catalyst layers and membrane at a position midway down the channel for basecase conditions.

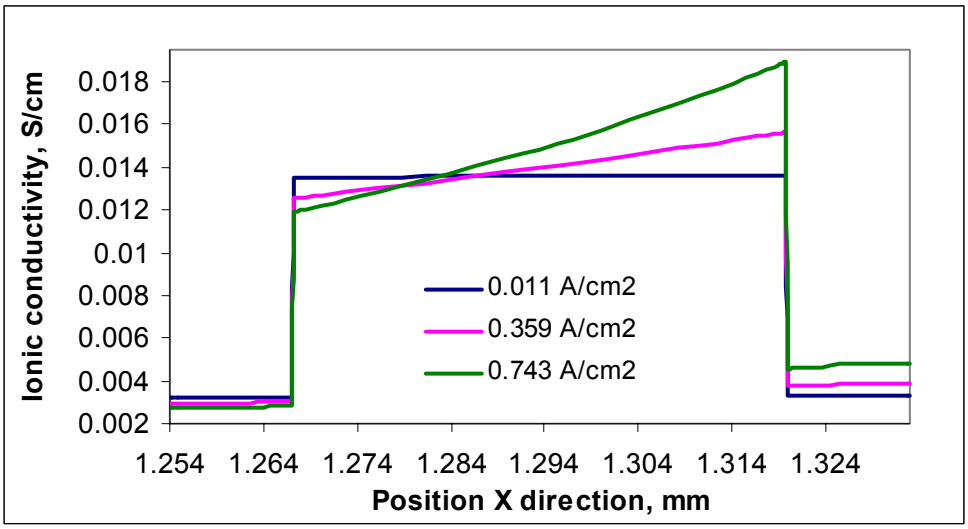

Figure 6.16 Ionic conductivity of the catalyst layers and membrane at a position midway down the channel.

Since fuel cells are typically run at high relative humidity on both the anode and cathode sides, any water that is dragged from the anode to the cathode will be unable to evaporate and will appear as liquid water in the pores of the catalyst layer and GDL. Figure 6.17 shows the magnitude of the source terms on the cathode accounting for liquid water production via electrochemical reaction as well as from dissolved water transport at mid-channel for a current density of 0.73 A/cm^2. On average, electro-osmotic drag is responsible for about 50% of the liquid water accumulation at the cathode when the cathode gas stream is fully saturated and the cell is run at low pressure. In the context of the present work, liquid water accumulation is a phrase used to denote the level of liquid water saturation within the porous media. Since the model is steady state, the rate at which water is generated anywhere in the fuel cell (by way of production or electro-osmotic drag) must equal the rate at which it is removed. Liquid water accumulation is indicative of the steady state liquid water saturation.

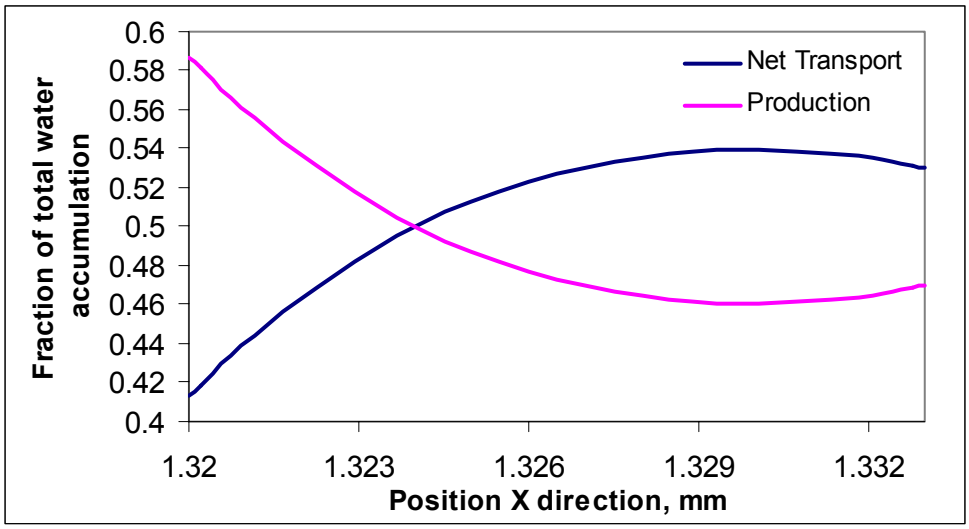

Figure 6.17 Comparison of the two principal sources of liquid water accumulation at the cathode for basecase conditions.

6.2.3 Transport of Liquid Water

The transport of liquid water within a fuel cell is one of the most important, yet least understood of the physical processes governing fuel cell performance. In this model, liquid water transport is assumed to occur by capillary action within the porous GDL and catalyst layer. Within the gas channels, liquid water is modeled as if it were transported by advection, as droplets of negligible volume. The presence of liquid water within the cell affects performance in two principal ways: liquid water accumulation within the porous GDL and catalyst layer leads to an increased resistance to gas phase reactant transport and the reaction rate is influenced by the presence of liquid water as it is assumed that water prevents reactant access to the catalyst sites. Of these two effects, the increased resistance to reactant diffusion has the most profound influence on performance, particularly at high current densities; this is illustrated in Figure 6.18 and Figure 6.19. Figure 6.18 shows three polarization curves. One of the curves, labeled "No liquid water effects", shows the cell performance if liquid water effects are omitted. The curve labeled "Mass transport effects" shows cell performance when the only effect of liquid water accumulation is an increased resistance to gas phase reactant transport (the effect of liquid water on access to catalyst sites is omitted). In Figure 6.19, the curve labeled "Catalyst blockage effects" shows cell

performance when the only effect of liquid water is the occlusion of reaction sites within the cathode catalyst layer by liquid water (mass transport effects are omitted). The curve labeled "Basecase" in both Figure 6.18 and Figure 6.19 shows cell performance when liquid water accumulation affects both the reactant transport and access to the catalyst reaction sites. Comparison of the results presented in the two figures shows that liquid water accumulation affects performance primarily by increasing the resistance to gas phase reactant transport.

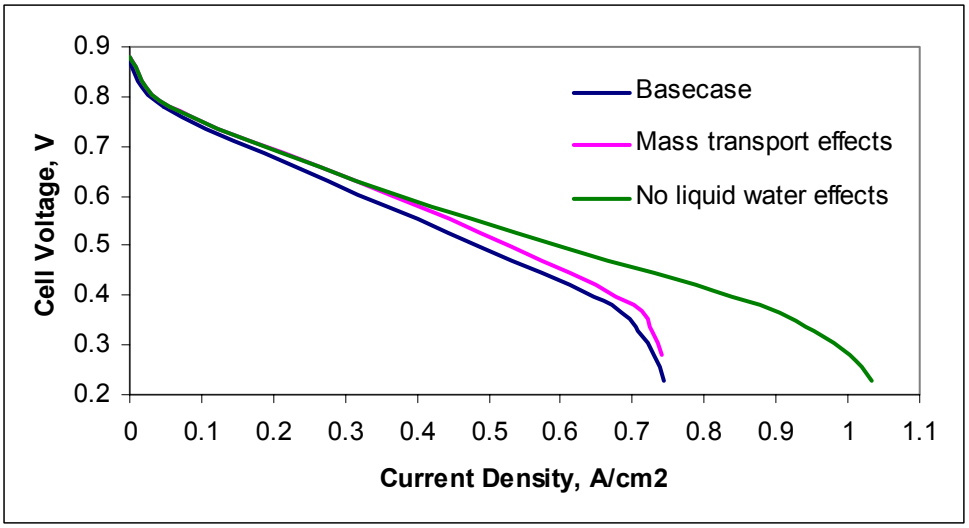

Figure 6.18 Variation in performance resulting from the effect of liquid water accumulation on reactant transport.

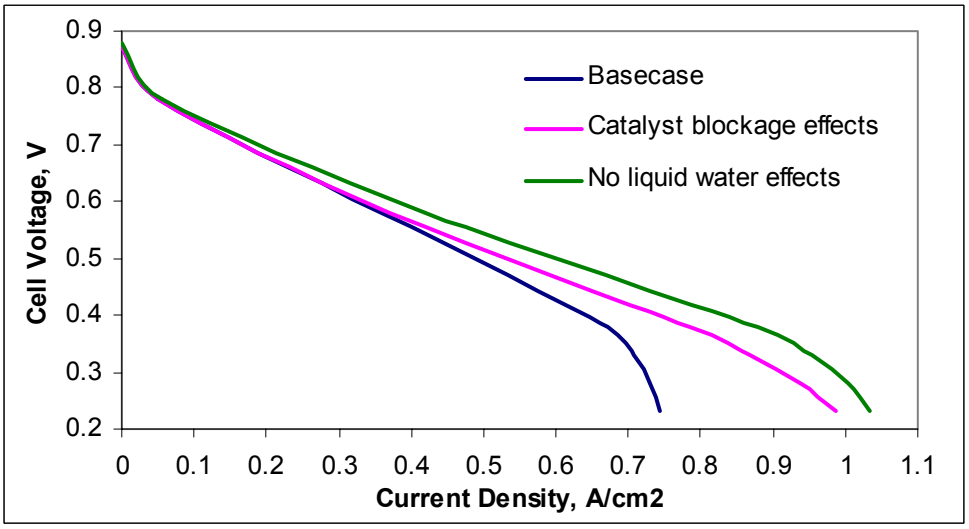

Figure 6.19 Performance variation resulting from the effect of liquid water accumulation on the available catalyst area.

Figure 6.20 is a contour plot showing the model results for the distribution of liquid water within the GDL and catalyst layer near the limiting current density for the test cell (0.74 A/cm^2). Since the transport process is diffusive, a gradient in liquid water saturation exists between the catalyst layer, where the water is produced, and the gas channel where it is removed from the cell. The model results show that the magnitude of liquid water saturation is highest near the inlet and drops as the flow moves down the channel. This results primarily from the fact that the reaction rate and water production rate are highest at the inlet where the oxygen concentration is the greatest. A more detailed model of liquid water transport, with attention given to transport in the gas channels, may show that liquid water saturation rises down the channel, since water may be transported as a film along the interface of the GDL and gas channel rather than as finely dispersed droplets.

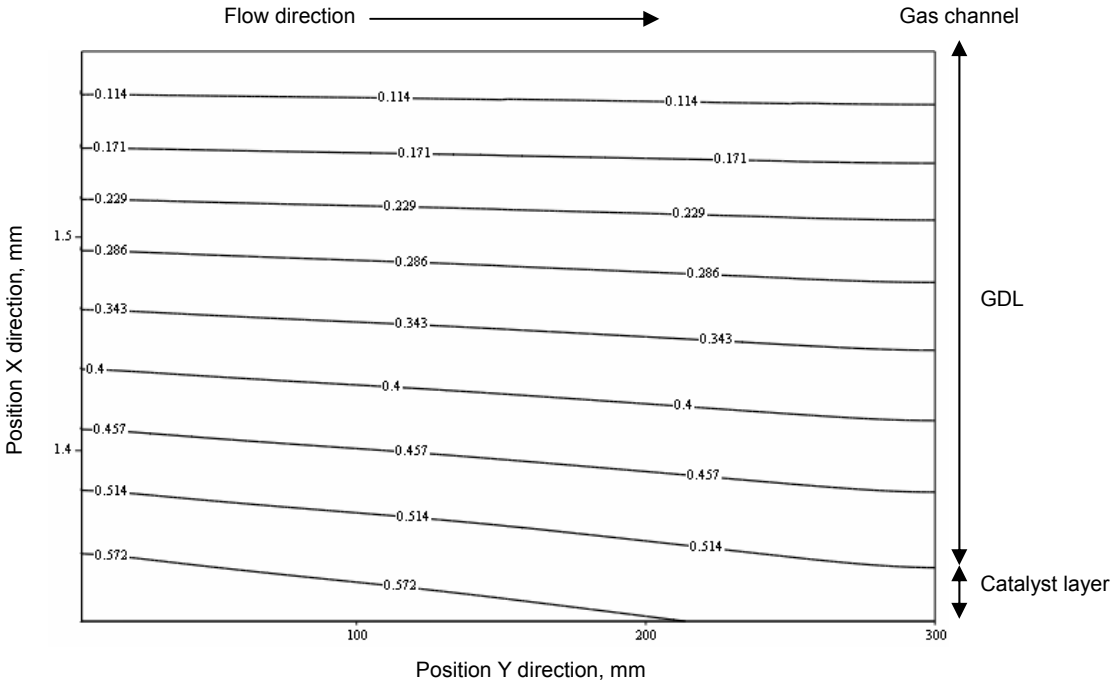

Figure 6.20 Liquid water saturation profile in the cathode catalyst layer and GDL at basecase conditions.

6.3 Three-Dimensional Transport Effects

The three-dimensional model improves on the accuracy of a simulation, relative to the two-dimensional model, by allowing for the inclusion of transport effects associated with the presence of the collector plate shoulders. In particular, these effects involve the transport of reactants and liquid water within the cell. Figure 6.21 shows a cross section of the three-dimensional model. The cross-hatched regions under the shoulders are of particular interest as they may be thought of as "dead spots" or areas where the resistance to the diffusive transport of reactants and products is significantly increased relative to the regions directly under the gas channels. The increased transport resistance results not only from an increased diffusion path length but also to a reduction in the porosity of the GDL due to crushing during the assembly process.

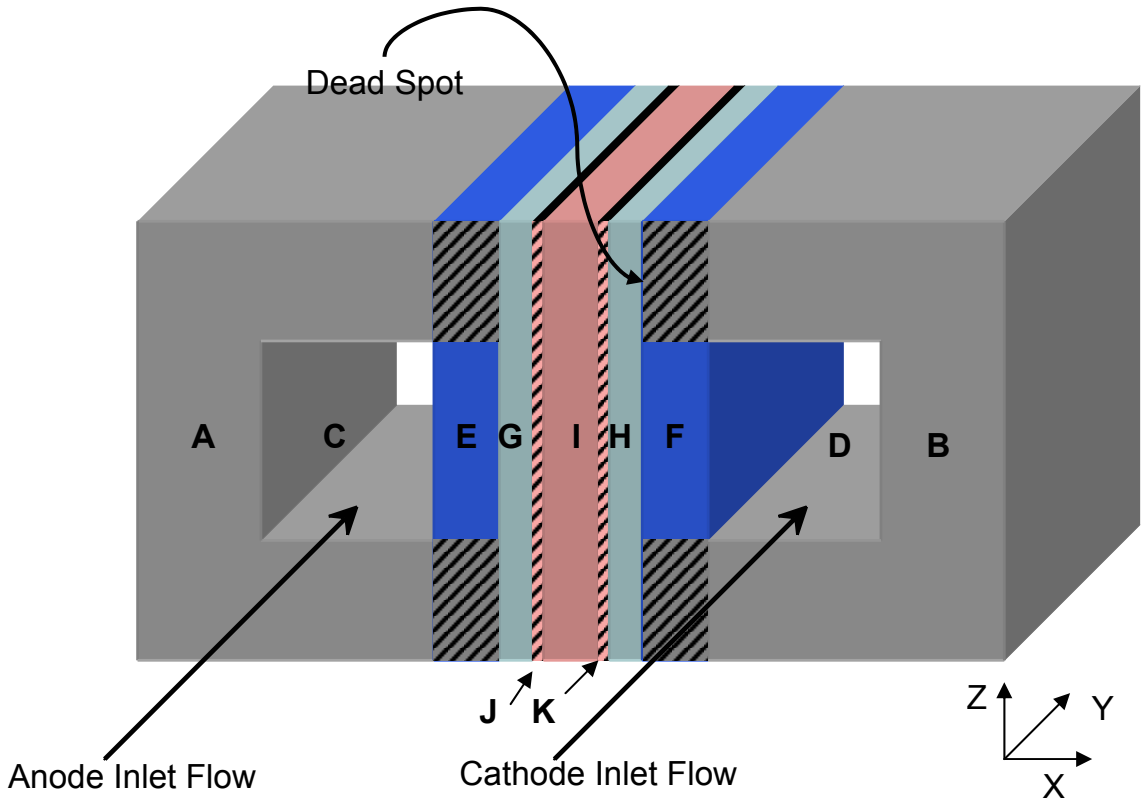

Figure 6.21 Cross section of the 3D model geometry showing "dead spots" beneath the collector plate shoulders.

Figure 6.22 shows a contour plot of the oxygen mass fraction at a position 3 cm down the channel from the fuel cell inlet. The results shown in the plot were generated using the three-dimensional model. The model formulation does not include the dissolved water or energy transport equations. Instead, a constant temperature is imposed over the entire solution domain; the polymer water content is set in the catalyst layers and in the polymer membrane based on results from the 2D model. Dissolved water transport from the anode to the cathode via electro-osmotic drag is simulated with a source term in the cathode catalyst layer. It is clear that the shoulders of the collector plate have enough impact on oxygen transport to cause a non-uniform oxygen distribution. Figure 6.23, which is a contour plot of the oxygen distribution across the surface of the cathode catalyst layer, shows that the reduction in oxygen transport underneath the shoulders also causes the oxygen to be distributed non-uniformly across the catalyst layer. The 2D model is unable to predict these results as it does not describe behavior in the z-direction and instead represents a single plane perpendicular to the membrane.

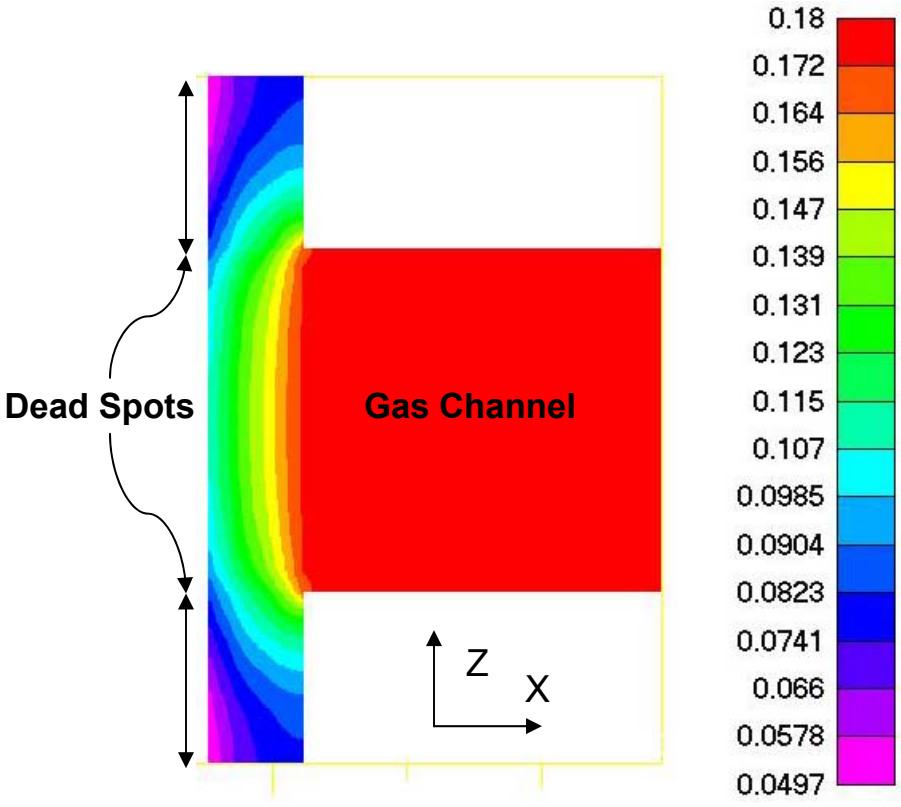

Figure 6.22 Contour plot of oxygen mass fraction near the cathode inlet (Y = 3 cm, Basecase conditions).

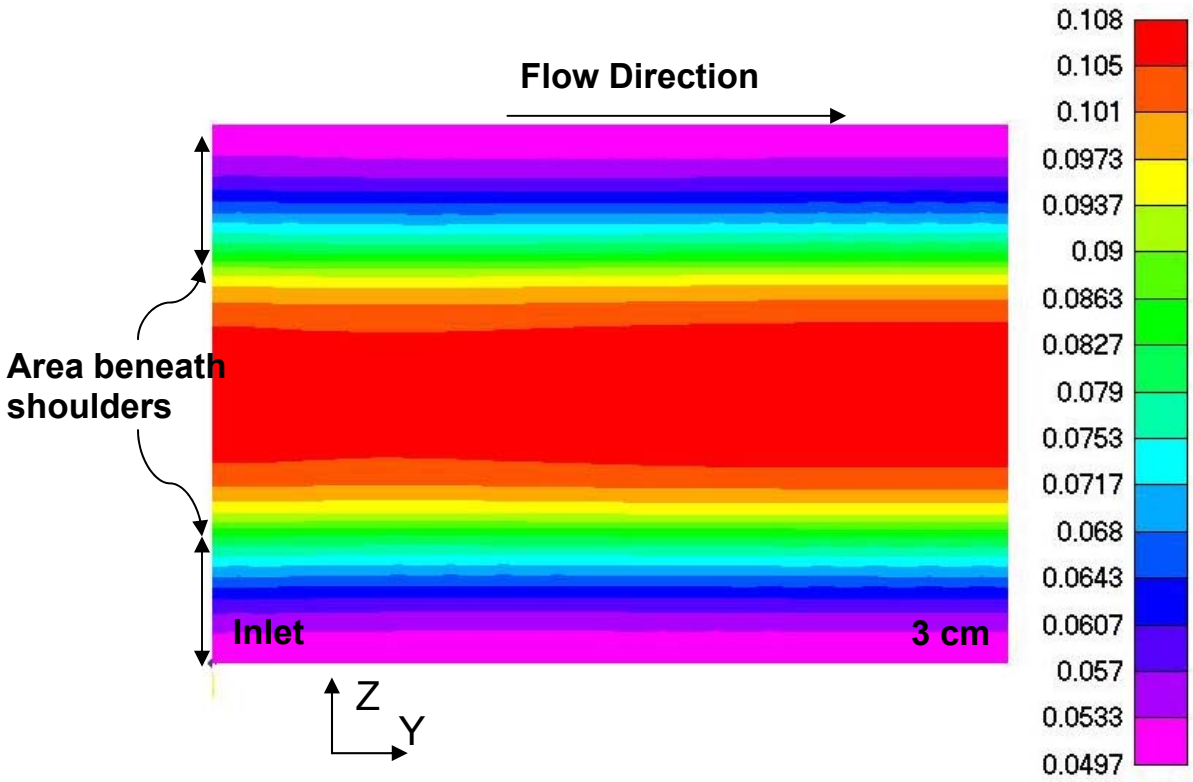

Figure 6.23 Oxygen mass fraction distribution across the surface of the cathode catalyst layer for the first 3 cm from the inlet (basecase conditions).

Liquid water transport is also influenced by the presence of the collector plate shoulders. Figure 6.24 shows a contour plot of liquid water saturation generated with the three-dimensional model. The level of liquid water saturation shown in Figure 6.24 is somewhat higher under the channel shoulders than it is directly under the gas channel itself. The increase in saturation under the collector plate shoulders also results in an increase in resistance to reactant diffusion through the porous GDL, compounding the effects associated with the longer diffusive pathway. The end result of the "dead spots" created by the collector plate shoulders is that the current density produced by the cell is non-uniform. Figure 6.25 shows a contour plot of current density across a surface passing through the middle of the membrane (current density is constant through the thickness of the membrane and equal to the current density produced by the cell). It is evident from these results that a significant fraction of the catalyst layer is not being utilized to its full potential, which results in a non-uniform current density profile. Furthermore, the transport effects associated with the

crushing of the GDL are not included in these results; if they were, the non-uniformity in current density would likely be even more pronounced. The significance of this effect can be illustrated by comparing the average current density over the region shown in Figure 6.25, which is 0.28 A/cm^2, to the current density in the area directly under the gas channel, which is 0.33 A/cm^2. The presence of the collector plate shoulders reduces the average current density by 15 %.

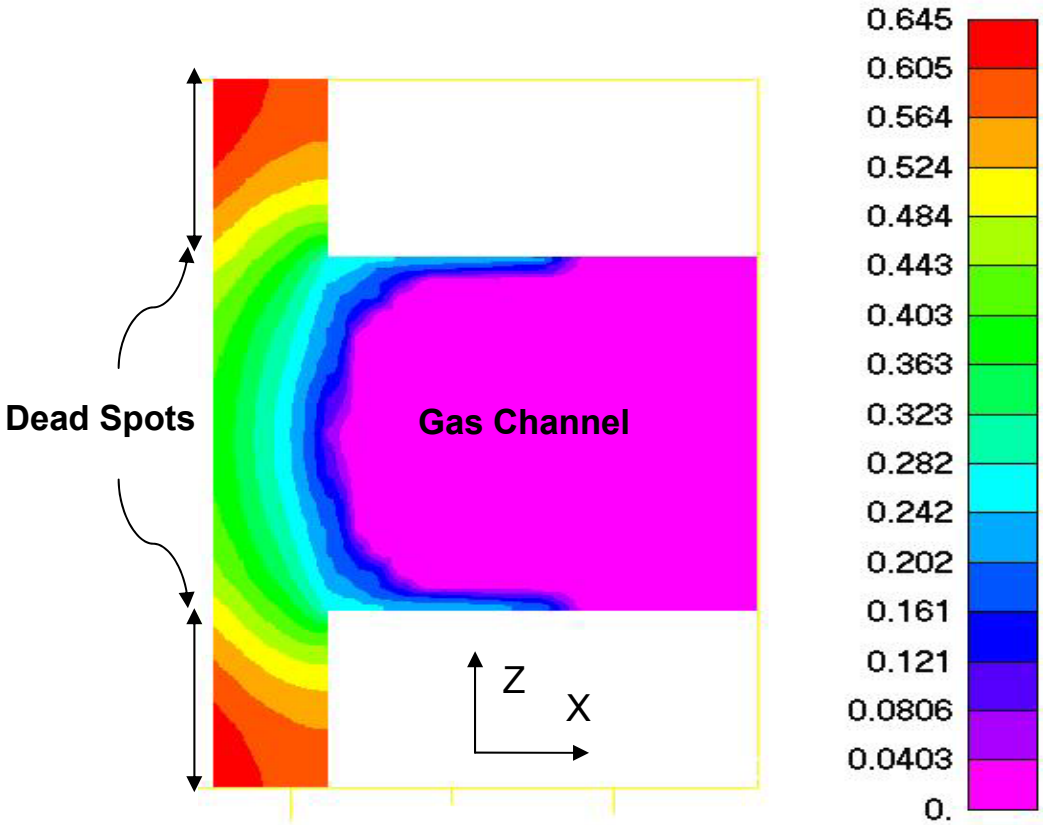

Figure 6.24 Liquid water saturation distribution across the cathode at a position 3 cm from the inlet (Basecase conditions).

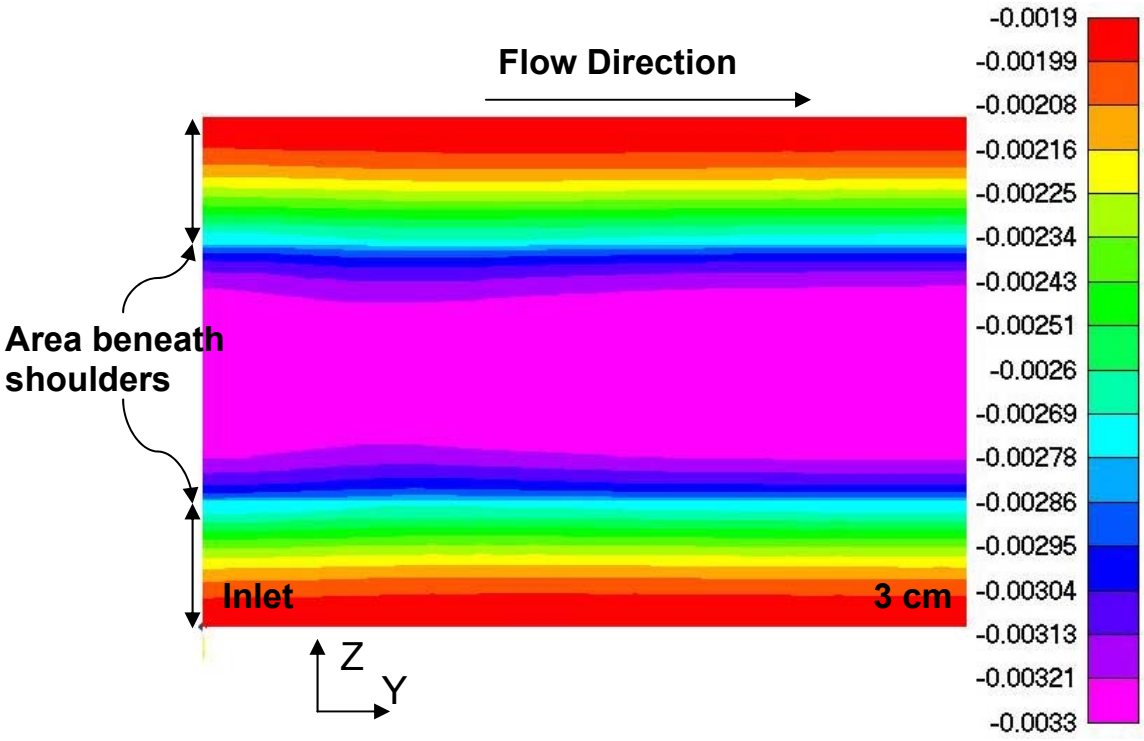

Figure 6.25 Current density contours across a surface passing through the middle of the membrane (current density is shown in A/mm^2).

It is evident from the preceding three-dimensional results that the presence of the collector plate shoulders significantly affects cell performance. This is further illustrated in Figure 6.26, which shows a comparison between the cell performance predicted by the 2D and 3D models under the same operating conditions. The current density produced by the cell at a given voltage, as predicted by the 3D model, is lower than that predicted by the 2D model. The difference between the performance predicted by the 2D and by the 3D model increases with current density; at higher current density, the mass transport effects associated with the presence of the shoulders, in the 3D model, become more pronounced, leading to a greater deviation from the 2D results.

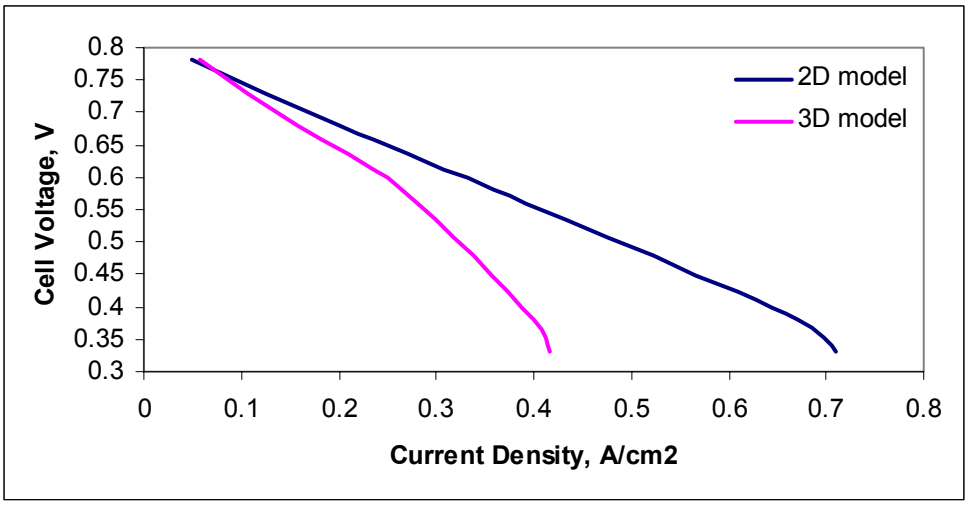

Figure 6.26 Performance comparison of the 2D and 3D models operating under the basecase conditions.

In order to compare the 3D results directly to experimental data, the model must be tuned. At present, the 3D model uses physical property values that have been determined through the tuning process discussed in Section 6.1 for the 2D geometry. The tuning process for the 3D model would likely show that some of the physical properties as determined for the 2D model must be changed in order to bring the 3D model into closer agreement with experimental data. In particular, it is likely that physical properties associated with gaseous reactant transport in the porous GDL and catalyst layers as well as liquid water transport would be different in the 3D and 2D models. For instance, the tortuosity of the GDL, which influences gaseous reactant diffusion in the GDL, is set such that the 2D model results will match the performance of the test cell in the mass-transport regime. Since the 2D model does not include the mass transport resistance caused by the collector plate shoulders but is still able to match experimental data in the mass-transport regime, it follows that the role of the tortuosity, with regard to mass-transport limitations, is overstated. If the shoulder effects were included, as in the 3D model, the value of the tortuosity of the GDL determined through tuning would be less than that currently used.

6.4 Parametric Studies

One of the most effective ways of learning about the fundamental processes governing fuel cell operation is by performing parametric studies. In this section, the two-dimensional model is used to show how certain parameters, or groups of parameters, affect the performance of a fuel cell. The results presented in Sections 6.4.1 through 6.4.3 illustrate how changes in fuel cell design parameters affect performance. These are parameters over which some degree of control is possible with regard to the construction of an actual fuel cell. The results presented in Sections 6.4.4 and 6.4.5 illustrate model sensitivity to physical properties that are not well established and that are more difficult to control. The sensitivity of the model results to these parameters is important considering that, as model complexity increases, so does the number of required physical properties, many of which carry a degree of uncertainty with regard to their numerical values.

6.4.1 Reactant Transport in the Gas Phase

Reactant transport in the gas phase has a significant impact on fuel cell performance, particularly within the cathode GDL and catalyst layer. Within these porous regions, reactant transport occurs by both advection and diffusion. However, due to the relatively small bulk velocity in these regions, the diffusive transport component dominates. The diffusive flux is given by Eq. (6.1) as a function of both independent variables (s, ρ^g, w^g_k, D^g_k) and physical parameters (ε_{gdl}, τ_{gdl}, Δt). It is assumed that, within the GDL and catalyst layer, the diffusive flux in the direction through the layer thickness is much more important, with regard to performance, than the flux in either of the other directions. The physical parameters, which are affected by the design of the fuel cell i.e., choice of materials, are grouped together into a single parameter, that is, the GDL diffusion parameter, or GDP, given by Eq. (6.2). The GDP directly influences the diffusive transport of gaseous reactants through the GDL.

$$N^g_{k,D} = -\frac{\varepsilon_{gdl}}{\tau_{gdl}}(1-s)\cdot D^g_k \rho^g \frac{\Delta w^g_k}{\Delta t_{gdl}} \tag{6.1}$$

$$GDP = \frac{\varepsilon_{gdl}}{\tau_{gdl}\Delta t_{gdl}} \tag{6.2}$$

Figure 6.27 shows a set of polarization curves, taken at base case conditions, for three values of the GDP given in Eq. (6.2). The model results show that an increase in the value of the GDP leads to an increase in performance across nearly the entire load range, including an increase in the limiting current. Performance increases because increasing the value of the GDP decreases the diffusive resistance of the GDL. Figure 6.28 shows normalized oxygen mass fraction profiles taken midway down the channel at 0.3 V. The drop in oxygen mass fraction between the gas channel and the catalyst layer decreases as the GDP increases. It is clear, from Eq. (6.2), that an increase in porosity or a decrease in either tortuosity or the thickness of the GDL increases the GDP and improves mass transport. However, in addition to affecting the GDP, the thickness of the GDL and the porosity can also affect reactant distribution across the surface of the catalyst layer as well as the electrical conductivity of the GDL. Thus, while increasing the GDP improves performance, the consequences of the changes required to improve the GDP must be considered.

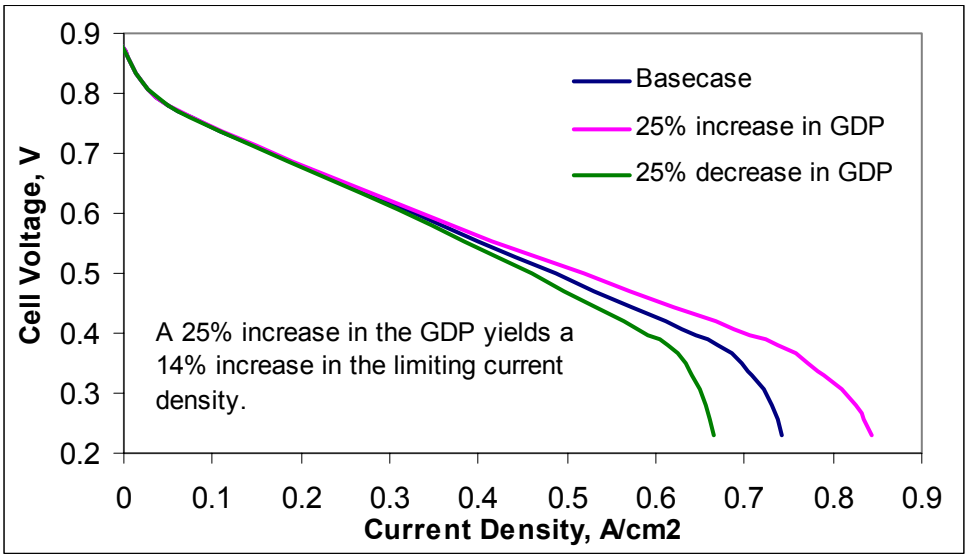

Figure 6.27 Variation in cell performance with the GDL Diffusion Parameter (GDP).

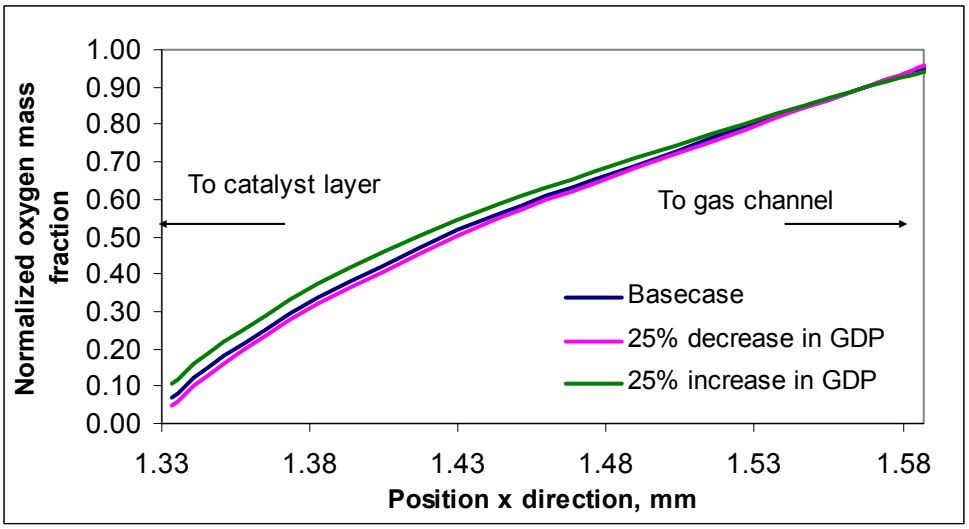

Figure 6.28 Influence of GDP on oxygen mass fraction profiles across the cathode GDL (basecase conditions, V_{cell}=0.3V). Oxygen mass fraction was normalized relative to the value at the GDL / gas channel interface.

In the catalyst layer, the group of terms associated with diffusive transport in the gas phase has a slightly different form than Eq. (6.2). The catalyst diffusion parameter or CDP is shown in Eq. (6.3). Notably absent from this expression is the tortuosity, a parameter for which data does not exist with regard to the catalyst layer. Instead, the Bruggeman correction is used to include the effects of tortuosity and porosity in one term [29]. This is discussed in Section 4.1. Figure 6.29 shows polarization curves for three different values of the catalyst diffusion parameter. It should be noted that the volume fraction of Pt/C catalyst and polymer within the catalyst layer were held constant for this parametric study. The consequences of this assumption are discussed in Section 6.4.4. Since the catalyst layer is so thin, changes in the diffusive resistance do not markedly affect performance unless they are relatively large. Figure 6.30 shows the corresponding normalized oxygen mass fraction profiles through the catalyst layer at a cell voltage of 0.3 V. A comparison of Figure 6.30 and Figure 6.28 shows that the relative drop in oxygen mass fraction is greater across the gas diffusion layer than across the catalyst layer. This is due principally to the fact that the gas diffusion layer is much thicker.

$$\mathrm{CDP} = \frac{\left(\varepsilon_{\mathrm{cat}}\right)^{1.5}}{\Delta t_{\mathrm{cat}}} \tag{6.3}$$

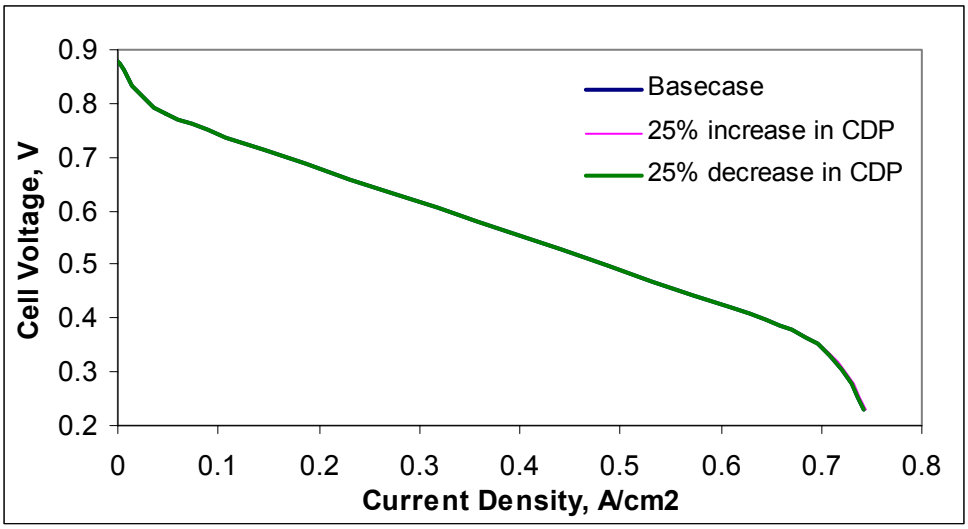

Figure 6.29 Variation in cell performance with Catalyst Layer Diffusion Parameter (CDP).

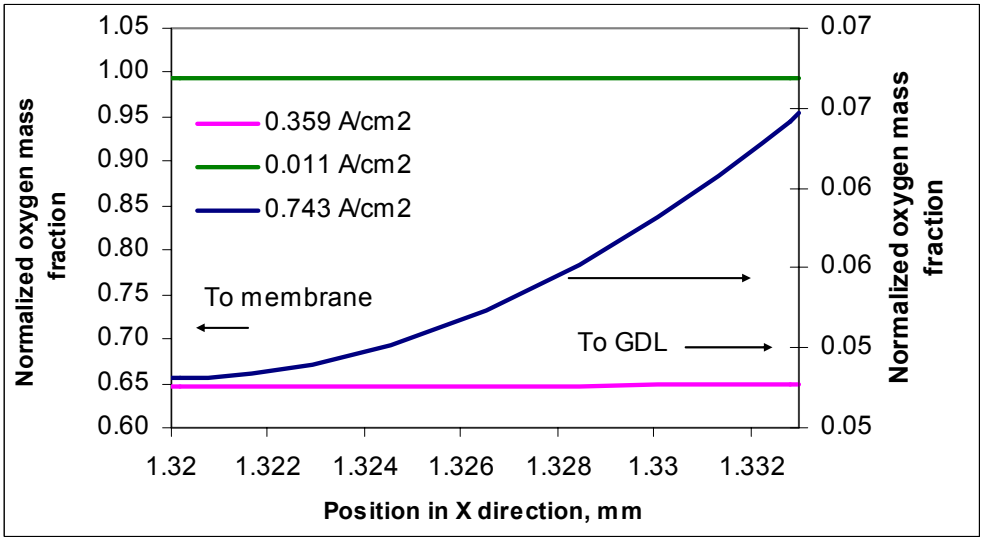

Figure 6.30 Influence of CDP on oxygen mass fraction profiles across the catalyst layer (basecase conditions, V_{cell}=0.3V). Mass fraction normalized relative to the mass fraction at the GDL/gas channel interface.

6.4.2 Reactant Transport within the Catalyst Layer Agglomerates

To reach the platinum catalyst reaction sites, reactants moving through the catalyst layer must dissolve into and diffuse through the polymer portion of the catalyst agglomerates.

This adds an additional mass transport resistance that is modeled with an effectiveness relationship, Eq. (6.4), based on Thiele's modulus, Eq. (6.5), both of which are discussed in Section 3.4.2. A group of physical properties can be isolated from Eq. (6.5) that has a particular influence on the magnitude of the effectiveness. This group of properties is shown in Eq. (6.6) and is called the agglomerate diffusion parameter (ADP). It is used to model both hydrogen and oxygen transport through the agglomerates. The agglomerate diffusion parameter is a function of the solubility of a given reactant in the polymer, denoted by Henry's constant, h_k^p, the diffusion coefficient within the polymer, D_k^p, and the diffusive path length through the agglomerate, $L_{aggl,d}$.

$$\eta_{aggl,d} = \frac{3}{\beta_d}\left(\frac{1}{\mathrm{Tanh}(\beta_d)} - \frac{1}{\beta_d}\right) \tag{6.4}$$

$$\beta_d = L_{aggl,d}\sqrt{\frac{|R_d|}{c_k^p D_k^p n_d F}} \tag{6.5}$$

$$\mathrm{ADP} = \frac{\sqrt{h_k^p D_k^p}}{L_{aggl,d}} \tag{6.6}$$

Figure 6.31 shows a set of polarization curves taken at base case conditions for three different values of the agglomerate diffusion parameter on the cathode side of the fuel cell. It is evident that even a small change in the value of this parameter has a significant impact on cell performance as predicted by the model. This is an important observation given that all three of the physical properties used in the formulation of the agglomerate diffusion parameter must be estimated to some degree. Specifically, there is some uncertainty with regard to the value of Henry's constant as well as to the value of the dissolved reactant diffusion coefficient for both hydrogen and oxygen species. In addition, data related to the variation of these properties with temperature and polymer water content is presently unavailable. Evaluation of the characteristic length of the agglomerates can be done using mercury porosimmetry and is discussed in Section 4.

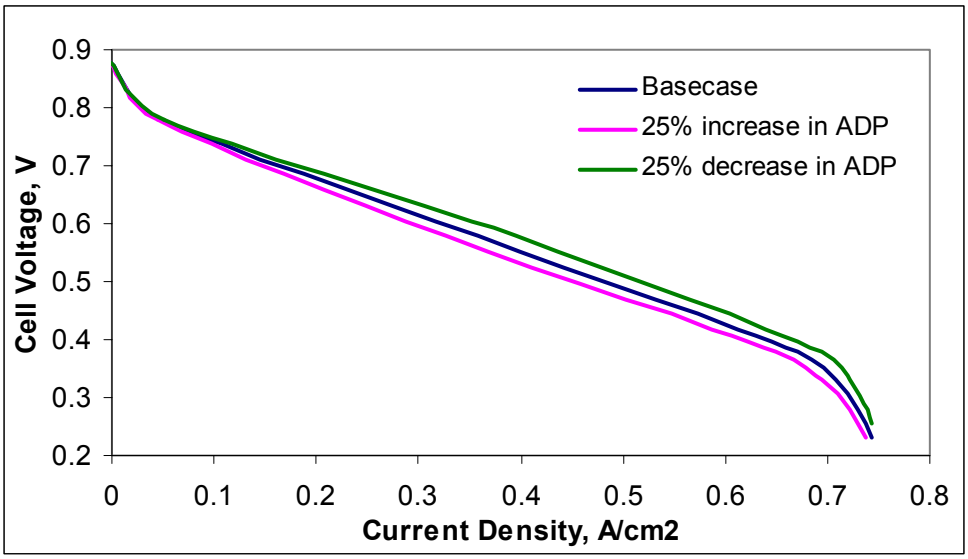

Figure 6.31 Variation in cell performance with the ADP (basecase conditions).

6.4.3 Catalyst Layer Composition

The composition of the catalyst layer with regard to the relative volume fractions of polymer, void volume, and Pt/C catalyst can influence cell performance in a variety of ways. Assuming a constant volume fraction of Pt/C catalyst as well as a constant catalyst layer volume, when a change is made in the porosity of the catalyst layer, a corresponding change must be made in the volume fraction of polymer. Figure 6.32 shows the variation in the amount of current density produced by a fuel cell at two set voltage levels as a function of the void volume fraction or catalyst layer porosity. The two curves shown in Figure 6.32 represent fuel cell operation in the ohmic regime (V_{cell}=0.58 V) and the mass-transport regime (V_{cell}=0.33 V). The vertical line indicates the catalyst layer porosity used in the basecase model. When operating in the mass-transport limited regime, there is an optimum porosity value. If the porosity is increased above this value, performance drops due to increased ohmic losses. A reduction in the catalyst layer porosity from the optimum value results in an increased resistance to reactant diffusion within the catalyst layer and a corresponding drop in performance. For operation in the ohmic regime (V_{cell}=0.58 V), increasing the porosity to a value greater than 0.05 leads to a decrease in performance. This results from a decrease in the ionic conductivity of the catalyst layers with porosity. A

decrease in the catalyst layer porosity below 0.05 leads to a decrease in performance due to increased mass transport resistance.

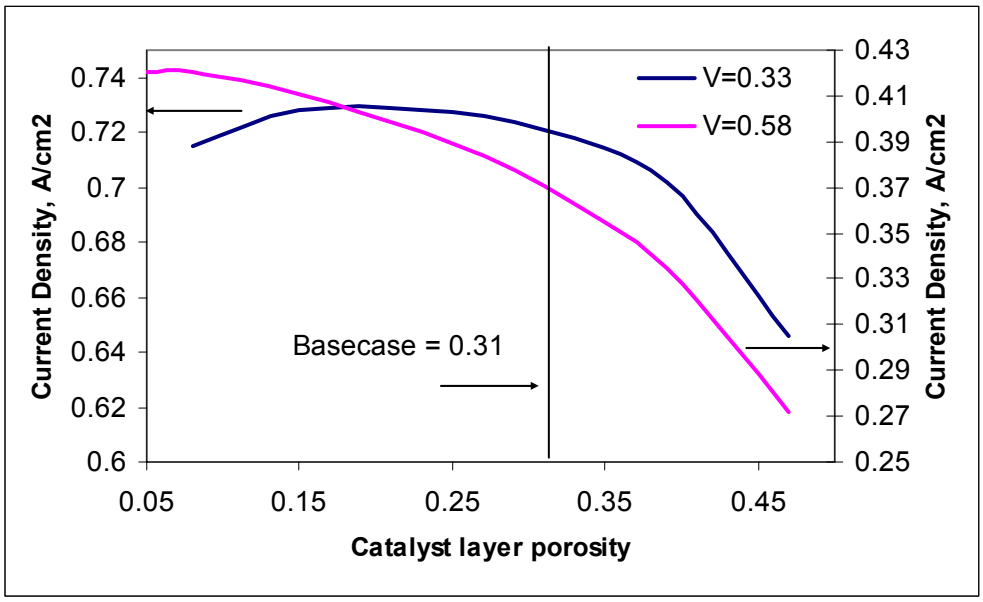

Figure 6.32 Influence of catalyst layer porosity on performance

The volume fraction of Pt/C catalyst within the catalyst layers can also influence performance. The amount of catalyst reaction area for a given catalyst layer volume can be changed either by changing the loading or the %wt of platinum relative to carbon support. In either case, the result is that the reaction rate at a given potential may be increased or decreased. In this model, the Pt catalyst surface area per catalyst layer volume is grouped together with another physical property, the reference exchange current density, to form a parameter called the reaction rate coefficient (RRC). The mathematical formulation of the reaction rate coefficient is given by Eq. (6.7). The Pt catalyst surface area per catalyst layer volume, A, may be determined experimentally using cyclic voltammetry, as discussed in Section 4.3. The reference exchange current density, $i_{0,k}$, which is a function of temperature, has been experimentally determined for the oxygen reduction reaction over a limited range of conditions [19,22]. Results from the model show that an increase in the reaction rate coefficient allows the fuel cell to produce more current at a given voltage. Figure 6.33 shows polarization curves at three values of the reaction rate coefficient. Although an increase in the RRC results in a corresponding increase in performance over the majority of the load

range, the limiting current remains unchanged. This result indicates that the value of the reaction rate coefficient does not directly influence mass transport effects within the fuel cell.

$$RRC = A\ i_{o,k} \tag{6.7}$$

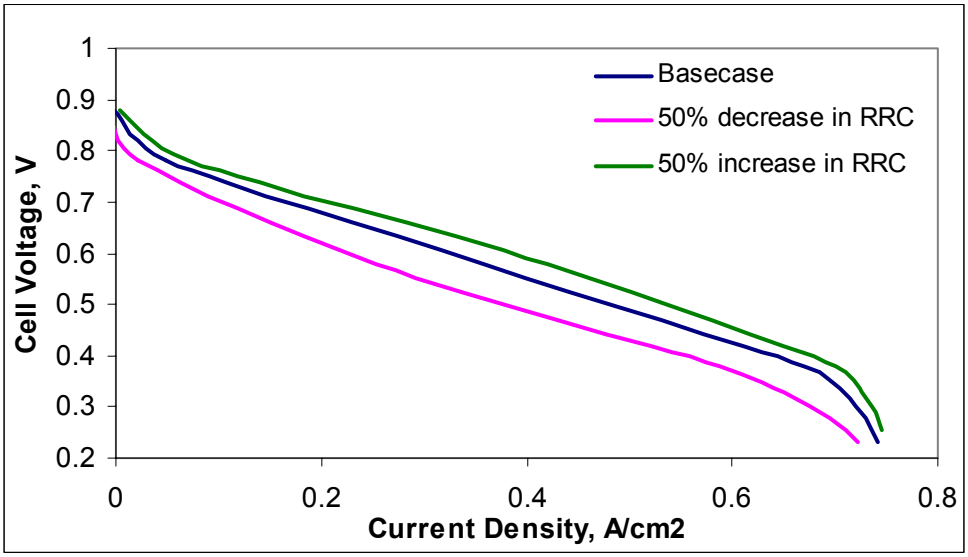

Figure 6.33 Influence of the Reaction Rate Coefficient (RRC) on cell performance (basecase conditions). The RRC was adjusted on both the anode and cathode sides of the cell.

6.4.4 Transport of Liquid Water within the Catalyst and Gas Diffusion Layers

As mentioned in Section 6.2.3, liquid water transport affects cell performance by increasing the diffusive resistance to gas phase mass transport and by blocking reaction sites within the catalyst layer. Furthermore, there is significant uncertainty associated with the determination of the liquid water diffusion coefficient. Figure 6.34 shows a set of polarization curves for different values of the liquid water diffusion coefficient. In one case, the effect of liquid water on cell performance has been taken out of the model completely. In the other case, the results indicate that a change in the liquid water diffusion coefficient not only affects the limiting current but also affects cell performance through most of the ohmic region. The activation regime is relatively unaffected. From the results presented in Figure 6.34, it is evident that the model is particularly sensitive to the value of the liquid water

diffusion coefficient in the ohmic and mass-transport regimes. Figure 6.35 shows model results for the liquid water saturation distribution along the cathode for basecase conditions. Figure 6.36 shows the same for a model having a liquid water diffusion coefficient that is 25% less than basecase value.

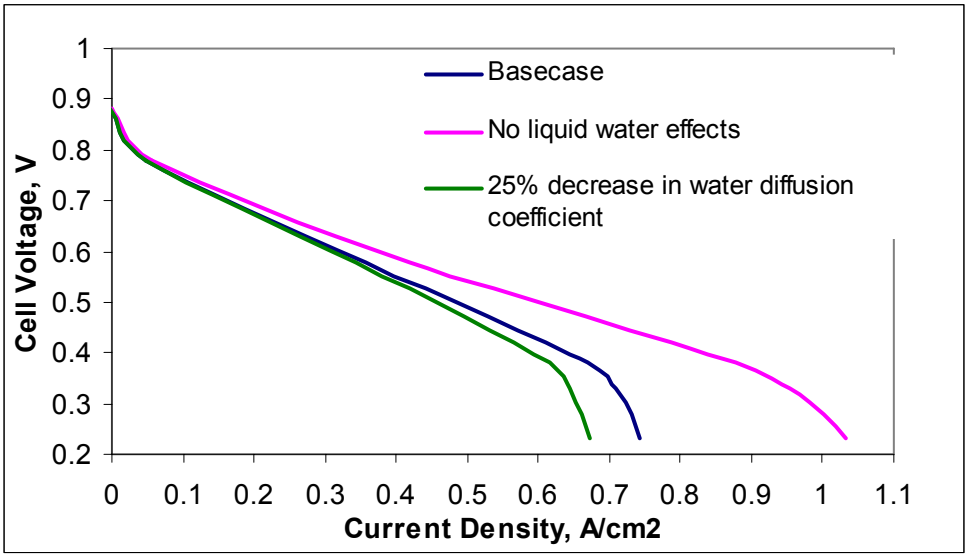

Figure 6.34 Effect of liquid water diffusion coefficient on performance

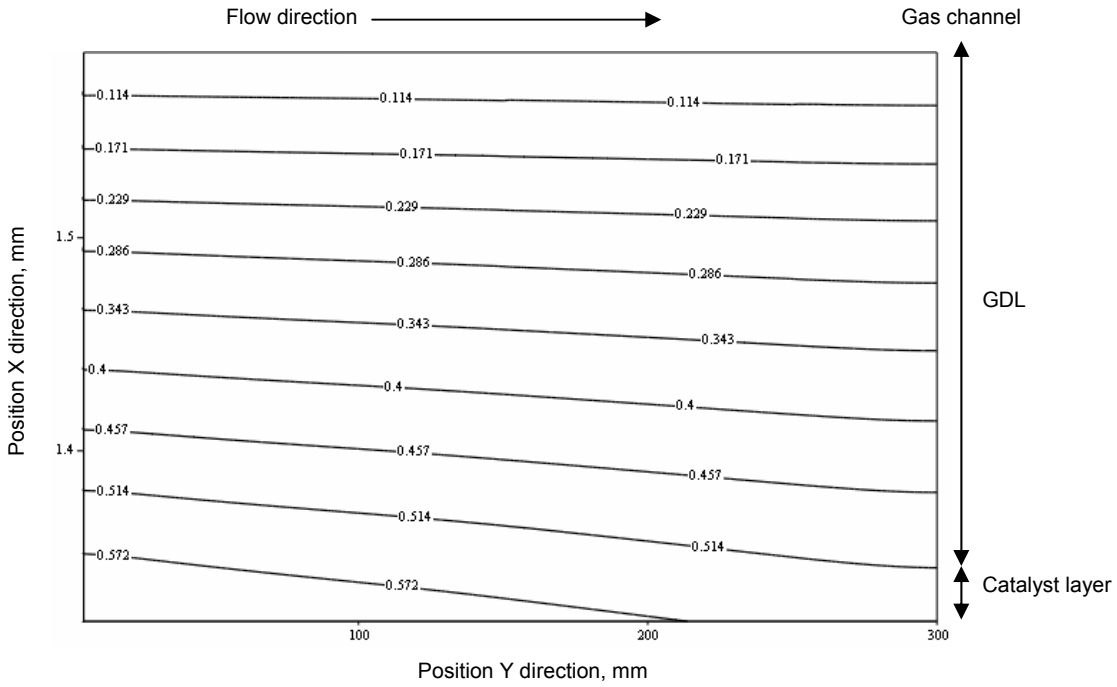

Figure 6.35 Liquid water saturation profile in the cathode GDL and calalyst layer for basecase conditions.

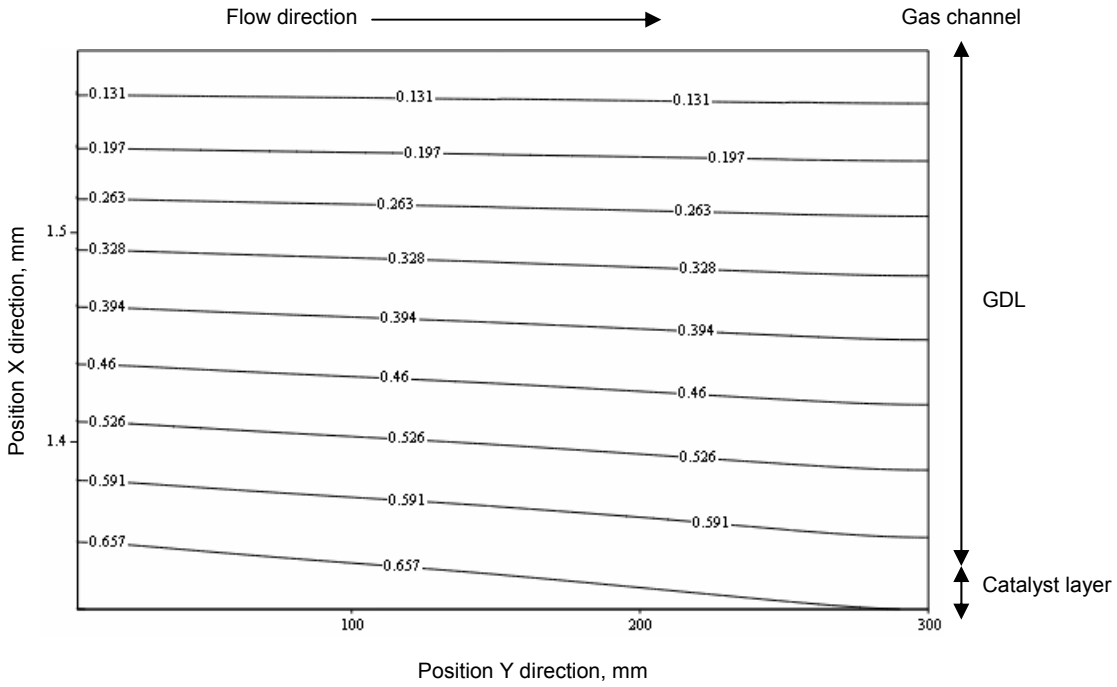

Figure 6.36 Liquid water saturation profile in the cathode GDL and catalyst layer with a 25% reduction in the liquid water diffusion coefficient.

Decreasing the liquid water diffusion coefficient by 25% causes the maximum saturation level in the cathode to increase by about 15%. The additional water accumulation leads to an increase in diffusive reactant transport resistance and a reduction in performance in the ohmic and mass-transport regimes.

6.4.5 Charge Transfer Coefficient

The charge transfer coefficient, α_d, is a measure of how much of the activation overpotential is applied toward changing the reaction rate [34] as determined by the Butler-Volmer formuation, Eq. (3.45). Since it appears in the exponent of the Butler-Volmer equation, even a small change in its value has a significant impact on performance as predicted by the model. Figure 6.37 shows the variation in performance for three values of the charge transfer coefficient. Typically, the value of the coefficient is reported as 0.5 for hydrogen oxidation and somewhere between 0.55 and 0.61 for oxygen reduction [19, 22],

although there is some degree of uncertainty with regard to the values reported in the literature.

$$R_d = (1-s)A\ i_{o,k}\left(\frac{c_k^p}{c_{k,ref}}\right)^{\gamma}\left[e^{(\phi_{e,d}-\phi_i)\alpha_d\frac{n_dF}{RT}} - e^{-(\phi_{e,d}-\phi_i)\alpha_d\frac{n_dF}{RT}}\right] \quad (3.45)$$

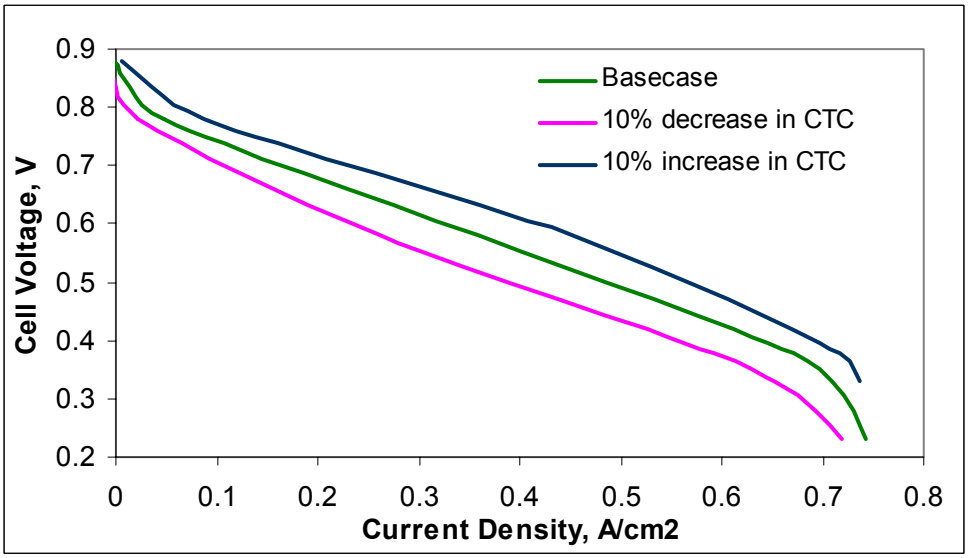

Figure 6.37 Variation in cell performance with the cathode Charge Transfer Coefficient (CTC) at basecase conditions.

Changing the transfer coefficient by even a small amount significantly affects cell performance over the entire operating range, with the exception of the limiting current density. An increase in the value of the charge transfer coefficient results in an increase in current production for a given cell voltage. In the activation regime, this is manifested as a reduction in the slope of the polarization curve. The slope in the ohmic region remains relatively unchanged.

6.5 Summary of modeling results

The modeling results presented in the preceding sections, 6.3 and 6.4, are summarized below.

6.5.1 Summary of model validation results

Model validation was performed at basecase conditions as well as at low anode relative humidity and low cell temperature. The results from the model validation work are summarized below:

- The two-dimensional model shows good agreement with experimental data at basecase conditions over the entire load range. The small differences that exist between the model results and experimental data are due to experimental uncertainty or uncertainty involved with the specification of numerical values for certain physical properties used in the model.
- The model can accurately predict the change in cell performance with operating temperature; performance decreases across the entire load range as temperature is decreased. It is necessary to adjust the liquid water diffusion coefficient in order to accurately predict the reduction in limiting current with temperature. The adjustment in the liquid water diffusion coefficient accounts for a change in the liquid water removal rate in the gas channels with temperature.
- The model predicts a decrease in performance in the activation and ohmic regimes as anode relative humidity is decreased. The model also predicts an increase in the limiting current as humidity is decreased. The reduction in performance in the ohmic and activation regimes results from a decrease in the ionic conductivity of the polymer portions of the catalyst layer as well as the membrane and is consistent with the experimental data. The shift in limiting current results from reduced water transport in dissolved form through the polymer from anode to cathode; as the anode relative humidity is dropped, the polymer in the anode catalyst layer dehydrates, thereby reducing its ability to transport water via electro-osmotic drag. The effect on

limiting current is consistent with data reported in the literature but not with our experimental data.

6.5.2 Effect of transport processes on fuel cell performance

The transport of reactants and products within the fuel cell is strongly connected to overall cell performance. A large portion of the modeling work presented in this dissertation is dedicated to exploring this connection. Table 6.3 summarizes the results of the parametric studies related to fuel cell transport processes in the activation regime ($V_{cell} = 0.8$), the ohmic regime ($V_{cell} = 0.6$), and the mass-transport regime ($V_{cell} = 0.3$).

Table 6.3 Summary of parametric studies.

Parameter	**Basecase value**	**$V_{cell} = 0.8$**	**$V_{cell} = 0.6$**	**$V_{cell} = 0.3$**
GDP	0.185 mm^{-1}	25% increase yields negligible increase in current density	25% increase yields a 3% increase in current density	25% increase yields a 13% increase in current density
CDP	13.280 mm^{-1}	25% increase yields negligible increase in current density	25% increase yields negligible increase in current density	25% increase yields negligible increase in current density
ADP	0.195 $(mm/s)^{0.5}$	25% increase yields a 6% increase in current density	25% increase yields a 11% increase in current density	25% increase yields a 1% increase in current density
Liquid water diffusion coefficient	0.0007 mm^2/s	25% decrease yields a 2% decrease in current density	25% decrease yields a 4% decrease in current density	25% decrease yields a 10% decrease in current density

An additional summary of model results is given below:

- Resistance to reactant transport, particularly oxygen diffusion in the gas phase, is greatest within the gas diffusion layer. At basecase conditions, near the limiting current, the oxygen mass fraction drops by nearly 90% through the cathode gas diffusion layer. The drop across the cathode catalyst layer at the same current density is much less. The difference is largely due to the fact that the gas diffusion layer is much thicker than the catalyst layer. The accumulation of liquid water increases the resistance to diffusion in both the cathode GDL and catalyst layer.
- Parameters closely linked to gaseous reactant diffusion in both the gas diffusion layer and the catalyst layer are identified and varied to determine their effect on cell

performance. In the gas diffusion layer, the GDL diffusion parameter (GDP) includes the structural properties of the GDL that influence reactant diffusion. Modeling results show that a 25% change in the GDP causes a significant performance change in the mass-transport regime but does not have a great deal of influence in the ohmic or activation regimes. The catalyst diffusion parameter (CDP) includes the structural aspects of the catalyst layer that are related to gaseous reactant transport. A 25% change in the CDP has little effect on cell performance in any operating regime.

- Reactant diffusion through the catalyst agglomerates occurs much more readily at the anode than at the cathode. This is illustrated by model results showing the distribution of the effectiveness, which is largely a function of the size of the catalyst agglomerates as well as the solubility and diffusion coefficient of a given reactant in the polymer portion of the agglomerates in the anode and cathode catalyst layers. At the anode, the magnitude of the effectiveness is much greater than at the cathode, indicating that hydrogen is transported through the catalyst layer in dissolved form more readily than oxygen.
- The agglomerate diffusion parameter (ADP) consists of a group of physical properties that have a significant influence on reactant transport through the agglomerates (they are all part of the formulation for effectiveness). Model results show that a variation in the ADP affects performance principally in the ohmic and mass-transport regimes, although it does not affect the limiting current.
- A variation in cell performance due to reactant depletion down the channel occurs for inlet stoichiometric ratios of less than 10 (relative to a current density of 1 A/cm^2).
- The transport of water in the dissolved phase influences cell performance by causing a gradient in ionic conductivity across the cell as well as by contributing to liquid water accumulation at the cathode. Under certain conditions, the amount of liquid water transported to the cathode via electro-osmotic drag can exceed the amount of liquid water produced within the cathode catalyst layer by electrochemical reaction.
- Liquid water accumulation influences cell performance by affecting the mass transport resistance of the porous gas diffusion layer and catalyst layer. In addition, the presence of liquid water within the pores of the catalyst layer can reduce the reaction rate by covering catalyst sites, thereby preventing reactant access. Of these

two effects, the mass transport resistance due to liquid water accumulation in the pores is by far the most dominant.

- The transport of liquid water is assumed to occur by diffusion (capillary action). Varying the magnitude of the liquid water diffusion coefficient leads to a variation in cell performance in the ohmic and mass-transport regimes as well as a shift in the limiting current.

6.5.3 Effect of catalyst layer composition on performance

The composition of the catalyst layer influences many aspects of the physics governing fuel cell operation including reactant and product transport, kinetics, and charge transport. A summary of model results related to catalyst layer composition is given as follows:

- The composition of the catalyst layer with regard to the relative amounts of void and polymer volume influences cell performance differently depending on the regime in which the cell is being operated. Model results show that for operation in the ohmic regime, it is desirable to have a large amount of polymer volume relative to void volume. In the mass transport regime, there is an optimum value for the ratio of the pore volume fraction to the polymer volume fraction. Too much porosity leads to a drop in performance due to increased ohmic losses; too little porosity restricts reactant flow through the catalyst and also results in a performance drop.
- The amount of platinum catalyst, in particular the platinum catalyst surface area per catalyst layer volume, influences cell performance. The catalyst area per volume is combined with the exchange current density in the form of a parameter called the reaction rate coefficient (RRC). Model results show that a variation in the RRC influences cell performance over the entire load range, with the exception of the limiting current.

6.5.4 Effect of the charge transfer coefficient on performance

- The charge transfer coefficient is a kinetic parameter that relates activation overpotential to a change in reaction rate. Model results show that a 10% variation in the magnitude of the charge transfer coefficient significantly changes cell performance over most of the load range and particularly in the activation regime.

6.5.5 Three-dimensional transport effects

Although it is possible to learn a great deal about fuel cell operation using a 1D or 2D model, a 3D model must be used to provide the most accurate description of the processes governing fuel cell behavior. Modeling results for the 3D geometry are summarized as follows.

- Solving the mathematical model using a three-dimensional model geometry allows for the inclusion of effects associated with the presence of the collector plate shoulders. 3D model results show that reactant transport is restricted beneath the regions where the shoulders contact the gas diffusion layer. In addition, the collector plate shoulders also inhibit the diffusive transport of liquid water, creating a non-uniform liquid saturation profile, with the regions directly beneath the shoulders having a relatively higher level of saturation. The accumulation of liquid water beneath the shoulders further reduces reactant transport through these regions. The net result is that sizable portions of the catalyst layer are not fully utilized.
- A comparison between the 2D and 3D model shows that the performance predicted by the 3D model is less than that predicted by the 2D model for identical operating conditions. This illustrates the degree to which mass transport effects related to the presence of the shoulders influence performance. It also illustrates that property values determined through the tuning process for the 2D model, e.g. tortuosity, may be different in the 3D model.

7 Conclusions and Recommendations

7.1 Summary

This work includes the development, validation, and application of a computational model of a hydrogen / air proton exchange membrane fuel cell. The model, which was developed from first principles, includes all of the transport processes thought to be relevant to fuel cell performance. The model can be solved in one, two, and three-dimensional geometries with the bulk of the results presented for the two-dimensional geometry. The results generated by the model were compared with experimental data taken with a test fuel cell for purposes of validation. The test data and modeling results were shown to be in good agreement over the entire range of cell operation. Results generated by the model also illustrate how the various transport processes occurring within the fuel cell influence performance as well as the implications of an agglomerate catalyst layer structure. In addition, parametric studies were performed that link cell performance to specific parameters related to reactant and product transport. The parametric studies also illustrate the sensitivity of the model to a variation in certain parameters used in the model.

7.2 Conclusions regarding the computational model

The computational model presented in this work is comprehensive and includes the transport of gaseous species, ionic charge, energy, mass, momentum, and water in the dissolved phase (within the polymer) and the liquid phase. These equations were solved over a single computational domain. The single domain solution approach requires that all of the equations are solved in all of the regions of the model. One of the benefits of the single domain approach is that it is not necessary to specify interface conditions between the individual fuel cell components. The computational model was solved with a commercially available CFD package, CFDesign™, adapted to include the transport relations relevant to PEMFCs.

The model includes the catalyst layers as volumetric regions, as opposed to simply treating them as interfaces at which reactions occur. The catalyst layers have an agglomerate

structure, meaning that they are composed of pores surrounding relatively non-porous regions made of ion conducting polymer and carbon supported platinum catalyst. Details regarding the structure of the catalyst layer were determined as part of this work using electron microscopy. A scanning electron microscope (SEM) was used to determine the thickness of the catalyst layer and to explore the actual structure of the layer. A transmission electron microscope (TEM) was used to explore the structure of the agglomerates themselves, which were found to be non-porous and contain platinum catalyst distributed non-uniformly on carbon support particles. The platinum catalyst surface area available for reaction was determined using cyclic voltammetry (CV). The CV testing showed that the actual platinum surface area was less than the theoretical maximum; this difference was attributed to the non-uniform distribution of the catalyst particles.

The model formulation is dependent on a number of physical properties that are needed to fully describe the transport processes taking place within the fuel cell. Many of these properties can either be measured directly or found in the literature. Some properties are not readily available in the literature or have not been determined to a high degree of accuracy. In this case, it was necessary to estimate the values of such properties. Work done with the computational model showed how predicted results vary with many of these properties and highlighted the importance of accurately determining the physical properties used in constructing the model. Model results, generated with the two-dimensional model, also showed the following:

- Cell performance drops as the temperature is decreased. This is due partly to a reduction in the exchange current density as well as the ionic conductivity with temperature. Liquid water transport also plays a role in the reduction in performance with cell temperature. As the temperature drops, the liquid water diffusion coefficient, assuming capillary flow, also decreases due to the increased liquid water viscosity. The model results indicate that there may be an additional effect, related to liquid water transport in the gas channels, which also affects cell performance as the temperature is changed. In particular, the velocity of the bulk gas flow in the gas channels decreases as cell temperature is decreased. This may lead to a reduction in the liquid water removal rate from the fuel cell. A reduction in the liquid water removal rate from the cell may in turn lead to an increase in liquid water

accumulation in the porous GDL and catalyst layer and a corresponding drop in performance with temperature, particularly in the mass-transport regime.

- Cell performance is affected significantly by reactant transport, particularly by diffusion within the gas diffusion layer. In the base case model, at high current density, the mass fraction of oxygen drops by about 90% across the GDL. This results from the physical structure of the GDL (thickness, porosity, tortuosity) as well as from an increase in diffusive resistance due to liquid water accumulation. By contrast, and under the same conditions, the mass fraction of oxygen drops by only 2% across the catalyst layer, which is much thinner. Parametric studies done with the model illustrate how changes in the GDL structure can affect performance. A reduction in tortuosity is one way to reduce the diffusive resistance of the GDL. Reducing tortuosity, rather than increasing porosity or decreasing layer thickness, is advantageous because it does not have any secondary effects with regard to cell performance (increasing porosity drops electrical conductivity; decreasing thickness reduces reactant dispersion uniformity across the catalyst layer surface).
- Although it was shown that diffusive transport in the gas phase within the catalyst layer does not have a significant impact on cell performance, transport of dissolved reactants within the polymer portion of the agglomerates does. Model results indicate that changes in reactant solubility, diffusion coefficient, or agglomerate size can significantly affect cell performance over nearly the entire operating range. In addition, there is currently little data available regarding the transport of hydrogen and oxygen in Nafion® and other ion conducting polymers.
- The transport of water in dissolved form through the polymer portions of the catalyst layer and membrane can contribute significantly to liquid water accumulation at the cathode. In fact, model results show that under certain conditions the rate at which water is transported to the cathode by electro-osmotic drag can equal or even exceed the rate at which water is produced by the electrochemical reactions.
- Liquid water accumulation in the cell affects performance by both restricting reactant transport through the porous gas diffusion layer and catalyst layer as well as by blocking access to reaction sites within the catalyst layer itself. The restriction of reactant transport by water accumulation is by far the more important of these two

effects. Currently, there is some degree of uncertainty with regard to the mechanisms by which water is transported in both the porous and non-porous sections of the fuel cell. Given the importance of liquid water transport to cell performance, as illustrated by the model, it follows that additional investigation of these phenomena is needed.

- The composition of the catalyst layer with regard to void volume and polymer volume can be optimized for maximum performance given the operating point (current density). In the ohmic regime (medium current density), a relatively non-porous catalyst layer containing a high volume fraction of ion conducting polymer is preferable. In the mass-transport regime (high current density), a more porous catalyst layer is needed to lessen the diffusive resistance to gaseous reactants.
- The influence of the collector plate shoulders on reactant and product transport as well as on cell performance was investigated using the three-dimensional model geometry. The results from the 3D analysis show that the presence of the shoulders in the fuel cell leads to reduced reactant diffusion and liquid water transport through the GDL. These effects result in a reduction in cell performance due to the incomplete utilization of the catalyst layer. Reducing the footprint of the shoulders on the GDL is one way of alleviating these effects; however, this leads to increased ohmic losses due to the reduced electrical conduction area.
- A comparison between the 3D and 2D models run under the same conditions shows that the performance predicted by the 3D model is less than that predicted by the 2D model. This indicates that the role of physical properties related to reactant diffusion, such as tortuosity, has been overstated in the 2D model. A more accurate estimation of these parameters can be found by tuning the 3D model, as opposed to the 2D model, to match experimental data.

7.3 Recommendations for future work with regard to physical property evaluation

An accurate determination of physical properties on which all computational models rely is essential to increasing the accuracy of any model. Currently, most experimental data

available for physical properties, in particular those involving the polymer electrolyte and catalyst layers, are not complete with regard to the level of information needed by a computational model. For instance, data for the exchange current density for the oxygen reduction reaction on a platinum micro-wire embedded in Nafion® film is available for one value of oxygen pressure, one value of membrane water content, and a range of temperatures. A more appropriate data set for use in a computational model might include:

- Data taken using an experimental electrode that more closely resembles a PEMFC catalyst layer - In particular, oxygen reduction may occur differently on dispersed platinum particles than on a smooth platinum wire. In addition, the properties of Nafion® film used in current experiments are different than the properties of recast Nafion® used in actual catalyst layers.
- The data should be taken over a wider range of conditions including variable membrane water content and variable oxygen pressure as well as variable temperature.

In general, physical property data used in computational models should come from experiments designed to be as similar, physically, to actual fuel cells as possible. In addition, this data should be taken over the entire range of operating conditions for which the model will be used. Future efforts could be aimed at more accurately determining the following physical properties:

- Hydrogen and oxygen solubility and diffusion coefficients within Nafion® and other ion conducting polymers.
- Kinetic parameters such as the exchange current density and charge transfer coefficient for both the oxygen reduction and hydrogen oxidation reactions.
- Physical characteristics of the catalyst layer such as porosity, tortuosity, and agglomerate size / composition.
- Anything having to do with the manner in which liquid water is transported within the porous sections of the cell - For capillary flow, this may amount to determining a relationship between the capillary pressure and liquid water saturation level in the pores.

7.4 Recommendations for improving the numerical model

There are two principal areas where the numerical model can be improved: it can be made more numerically robust, and the solution time can be reduced. As discussed in Section 5, the model is sensitive to large, rapid changes in the density of the bulk gas flow. If the density changes too rapidly, which may happen when the cell current density is high, the velocity and pressure solutions tend to become unstable, which can lead to a diverged solution. Inertial relaxation is currently used to slow down the rate of change of the density, but increasing the inertial relaxation also increases the solution time. It follows that one area in need of improvement is the coupling between the pressure and velocity solvers and the other equations in the mathematical model. Some avenues that should be explored are: determining which matrix solvers are best for each of the equations, determining whether or not the order of solution of the equations has an impact on numerical stability and, if so, what is the best solution sequence, taking a closer look at the actual causes of the density change (the species source terms – preliminary work has been done in this area) and determining if there is a better way of incorporating them into the model.

Methods for improving solution time are discussed in Section 5. The most direct path to decreased solution time is to use a faster computer to solve the model. The CFD package used to solve the model does work, with regard to the momentum and energy equations that come built-in to the solver, on a computer with parallel processors. However, work done early in this project indicated that the equations used to model fuel cell performance were not solvable on a machine using parallel processors. The reasons for the limitations to parallel processing are not known, and the elimination of these limitations is an opportunity for future work. Moreover, the current CFD package requires that the parallel processors be part of the same machine and share the same system memory. Thus, the package will not work on a computer cluster, which typically has system memory distributed among many machines. Even if it was possible to solve the current computational model on a machine with parallel processors, the most powerful of these computers available today cannot rival the computational speed of a cluster. Furthermore, the actual computational model formulation is not limited to any one computer platform or CFD package. For these reasons and in light of the fact that Virginia Tech has more than one cluster on campus, it would be worthwhile to

explore the possibility of adapting the existing CFD package such that it can be solved with a cluster.

7.5 Recommendations for future modeling work

Future modeling efforts might be focused in two directions: improving the existing comprehensive model and creating smaller models of specific fuel cell phenomena or transport processes. The output of these smaller, more focused models may be useful to the more general comprehensive model. Some improvements that might be made to the existing comprehensive model, in addition to those discussed in the preceding section are:

- Refining the model as solved with the 3D geometry - In particular, tuning the 3D model to match experimental data.
- More accurately modeling liquid water transport in the cell - In the near term this might involve determining a way to calculate a liquid water diffusion coefficient for a given cell based on a comparison between the model and experimental data. In the long term, efforts might be directed at more completely modeling two-phase flow within the cell, i.e. using a true two-phase solver.
- Creating a 3D model based on a more accurate representation of a fuel cell flowfield - Currently, the 3D model consists of two straight channels. The ability to explicitly model a fuel cell with a serpentine flowfield would be advantageous. The only drawback is that this type of model would be computationally intensive and require a rather powerful computer (cluster) in order to solve it. It may be possible to gain useful information from a model that includes only the mass and momentum equations, but for a more realistic flowfield design. The results from such a model could then be applied to the more complete comprehensive model.
- Explore the role of the momentum equations in the model - It may be possible to make the model more numerically robust by redefining the approach taken in coupling the momentum equations to the other fuel cell transport equations. It is even possible that the model could be adapted in such a way as to produce useful results without including the solution of the momentum equations.
- Investigate how the model might be adapted for use in system level modeling efforts.

Small, focused models could be used to explore individual transport processes or transport in individual fuel cell components with a degree of resolution not feasible with the more general comprehensive model. The knowledge gained from these models could then be used to refine the comprehensive model. Some areas where focused models would be useful are:

- Transport of gaseous reactants and liquid water within the catalyst layer and the gas diffusion layer.
- Transport of dissolved reactants within the catalyst agglomerates - In this case, microscopic models of the catalyst layer may be useful.
- Transport of liquid water within the gas channels - The model presented in this work assumes that liquid water transport occurs as finely dispersed droplets within the gas channel. It is possible that this assumption is not correct and that liquid water, at least in some cases, may be transported as a film or as large droplets. A two-phase model of water transport in the gas channels and along the gas channel / GDL interface may be useful in understanding, among other things, why cell performance changes with temperature in the mass-transport regime.

7.6 Closing remarks

The computational model developed in this work represents a step forward in the ability to simulate, comprehensively, the physical processes governing fuel cell behavior. Using the computational model, it is possible to more fully understand what impact design parameters have on fuel cell performance. The ability to do this is useful not only as learning tool, but also as a first step in the process of designing fuel cells. In addition, the computational model can be used as a starting point for future modeling efforts. These may include further refinement of the existing model as more is learned about the physical aspects of fuel cells or perhaps adaptation of the model to simulate other types of fuel cells such as direct methanol or solid oxide fuel cells. The inherent versatility of the model with regard to both the mathematical and geometric structure gives it the potential to be useful in a wide variety of fuel cell research activities.

References

1. T.E. Springer, T.A. Zawodzinski, S. Gottesfeld, "Polymer Electrolyte Fuel Cell Model," J. Electrochem. Soc., Vol. 138, No. 8, 1991, pp. 2334-2341.
2. T.E. Springer, S. Gottesfeld, "Pseudohomogeneous Catalyst Layer Model for Polymer Electrolyte Fuel Cell," Proc. of the Symposium on Modeling of Batteries and Fuel Cells, R.E. White, M.W. Verbrugge, and J.F. Stockel, Editors, PV 91-10, pp. 197-208, The Electrochemical Society Softbound Proceedings Series, Pennington, NJ, (b).
3. K. Broka, P. Ekdunge, "Modelling the PEM fuel cell cathode," J.Applied Electrochemistry, Vol. 27, pp. 281-289, 1997.
4. P.C. Sui, L.D. Chen, J.P. Seaba, Y. Wariishi, "Modeling and Optimization of a PEMFC Catalyst Layer," SAE Congress, 1999-01-0539, 1999, pp. 61-70.
5. C. Marr, X. Li, "Composition and Performance modeling of catalyst layer in a proton exchange membrane fuel cell," J. Power Sources, Vol. 77, 1999, pp. 17-27.
6. Z.H. Wang, C.Y. Wang, "Two-Phase Flow and Transport in the Interdigitated Air Cathode of Proton Exchange Membrane Fuel Cells," Proceedings ASME Heat Transfer Division, HTD-Vol.366-1, 2000, pp. 27-33.
7. B. Eaton, M.R. von Spakovsky, M.W. Ellis, D.J. Nelson, B. Olsommer, N. Siegel, "One-Dimensional, Transient Model of Heat, Mass, and Charge Transfer in a Proton Exchange Membrane," Proceedings of IMECE, 2001.
8. D. Natarajan, T. Van Nguyen, "A Two-Dimensional, Two-Phase, Multicomponent, Transient Model of the Cathode of a Proton Exchange Membrane Fuel Cell Using Conventional Gas Distributors," J. Electrochem. Soc., Vol. 148, No. 12, 2001, pp. A1324-A1335.
9. F. Jaouen, G. Lindbergh, G. Sundholm, "Investigation of Mass-Transport Limitations in the Solid Polymer Fuel Cell Cathode," J. Electrochem. Soc., Vol. 149, No. 4, pp. A437-A447, 2002.
10. D. Natarajan, T.V. Nguyen, "Three-dimensional effects of liquid water flooding in the cathode of a PEM fuel cell," J. Power Sources, Vol. 115, 2003, pp. 66-80.
11. D. Genevey, M.R. von Spakovsky, M.W. Ellis, D.J. Nelson, B. Olsommer, F. Topin, N. Montel, N.P. Siegel, "Transient Model of the Heat, Mass and Charge Transfer as well as Electrochemistry in the Catalyst Layer of a PEMFC," International Mechanical Engineering Congress and Exposition – IMECE'2002, ASME IMECE Paper No. 33322, N.Y., N.Y., November, 2002.
12. D.M. Bernardi, M.W. Verbrugge, "A Mathematical Model of the Solid-Polymer-Electrolyte Fuel Cell," J. Electrochem. Soc., Vol. 139, No. 9, pp. 2477-2490.
13. V. Gurau, H. Liu, S. Kakac, "Two-Dimensional Model for Proton Exchange Membrane Fuel Cells," J.AIChe, Vol. 44, pp. 2410-2422.
14. J.S. Yi, T.V. Nguyen, "An along-the-channel model for proton exchange membrane fuel cells," J. Electrochem. Soc., Vol. 145 (4), 1998, pp. 1149-1159.
15. S. Um, C.Y. Wang, K.S Chen, "Computational Fluid Dynamics Modeling of Proton Exchange Membrane Fuel Cells," J.Electrochem.Soc, Vol 147, No. 12, pp. 4485-4493, 2000.

16. S. Dutta, S. Shimpalee, J.W. Van Zee, "Numerical prediction of mass-exchange between cathode and anode channels in a PEM fuel cell," Int. J. Heat and Mass Transfer, Vol. 44, 2001, pp. 2029-2042.
17. N.P. Siegel, M.W. Ellis, D.J. Nelson, M.R. von Spakovsky, "Single domain PEMFC model based on agglomerate catalyst geometry," J. Power Sources, Vol. 115, 2003, pp. 81-89.
18. N.P. Siegel, M.W. Ellis, D.J. Nelson, M.R. von Spakovsky, "A two-dimensional computational model of a PEMFC with liquid water transport," Accepted J. Power Sources, Sept. 20 , 2003.
19. A. Parthasarathy, S. Srinivasan, A.J. Appleby, C.R. Martin, "Temperature Dependence of the Electrode Kinetics of Oxygen Reduction at the Platinum/Nafion® Interface – A Microelectrode Investigation," J. Electrochem. Soc., Vol. 139, No. 9, pp. 2530-2537, 1992.
20. T.A. Zawodzinski, T.E. Springer, J. Davey, R. Jestel, C. Lopez, J. Valerio, S. Gottesfeld, "A comparative study of water uptake by and transport through ionomeric fuel cell membranes," J. Electrochem. Soc., Vol. 140, No. 7, 1993, pp. 1981-1985.
21. T.E. Springer, T.A. Zawodzinski, M.S. Wilson, S. Gottesfeld, "Impedance Sectroscopy," J. Electrochem. Soc., Vol. 143, No. 2, 1996, pp. 587-599.
22. L. Zhang, C. Ma, S. Mukerjee, 'Oxygen permeation studies on alternative proton exchange membranes designed for elevated temperature operation,' Electrochimica Acta, 48, pp. 1845-1859, 2003.
23. L. Wang, A. Husar, T. Zhou, H. Liu, "A Parametric Study of PEM Fuel Cell Performances," Proceedings of IMECE, IMECE2002-33167, 2002, pp. 1-7.
24. J. Russell, M.W. Ellis, "Experimental investigation of the effects of catalyst layer composition on the performance of proton exchange membrane fuel cells," Proceedings of IMECE, IMECE2003-42817, 2003.
25. J. Ihonen, F. Jaouen, G. Lindbergh, A. Lundblad, G. Sundholm, "Investigation of Mass-Transport Limitations in the Solid Polymer Fuel Cell Cathode," J. Electrochem. Soc., Vol. 149, No. 4, pp. A448-A454, 2002.
26. K.C. Desrosiers, "Evaluation of Novel and Low-Cost Materials for Bipolar Plates in PEM Fuel Cells," Masters Thesis, Virginia Polytechnic and State University, 2002.
27. R.B. Bird, W.E. Stewart, E.N. Lightfoot, "Transport Phenomena, 2nd Edition," Wiley, 2001.
28. F.A.L. Dullien, "Porous Media: Fluid Transport and Pore Structure," Elsevier, London, 1992.
29. J.A. Currie, "Gaseous diffusion in porous media. Part 2. – Dry granular materials," Br.J.Appl.Phys., Vol. 11, 1960, pp. 318-324.
30. O. Levenspiel, "Chemical reaction engineering," Wiley, 1972.
31. M. Kaviany, "Principles of Heat Transfer in Porous Media," Springer, New York, 2002.
32. J.B. Russell, "Investigation of the effect of catalyst layer composition on the performance of PEM fuel cell," Masters Thesis, Virginia Polytechnic and State University, 2003.

33. R. O'Hayre, "A sharp peak in the performance of sputtered platinum fuel cells at ultra-low platinum loading," Journal of Power Sources, 109, pp. 483-493.
34. J. Larminie, A. Dicks, "Fuel Cell Systems Explained," Wiley, West Sussex, 2003.
35. FEMAP® V8.0, EDS, 2002.
36. CFDesign® V5.1, Blue Ridge Numerics, 2003.
37. S. Patankar, "Numerical Heat Transfer and Fluid Flow," Hemisphere, Washington D.C., 1980.
38. R. Fox, A. McDonald, "Introduction to Fluid Mechanics," Wiley, New York, 1992.

Appendix A: Basecase physical properties and model parameters

Table A1 Physical property values for the basecase model

Property	Value	Source
Faraday's constant, F	96485 C/mol	[15]
Permeability of gas diffusion layer, κ	1.2×10^{-6} mm^{-2}	[15]
Cathode gas viscosity, μ_{air}	1.0×10^{-5} Pa-s	Calc.[1]
Anode gas viscosity, μ_{H2}	2.0×10^{-5} Pa-s	Calc.[1]
Liquid water viscosity at 80 C, μ_{WL}	4.0×10^{-3} g/cm·s	[38]
Diffusivity of oxygen in the polymer, $D_{m,O2}$	2.0×10^{-4} mm/s	Est[2]
Diffusivity of hydrogen in the polymer, $D_{m,H2}$	7.9×10^{-4} mm/s	[12]
Reference anode exchange current density, $i_{0,H2}$	3.0×10^{-5} A/mm^2	[34]
Reference cathode exchange current density, $i_{0,O2}$	4.0×10^{-9} A/mm^2	Est.[2]
Anodic transfer coefficient, α_a	0.50	[34]
Cathodic transfer coefficient, α_c	0.64	Est.[5]
Oxygen reference concentration, $c_{O2,\,ref}$	8.4×10^{-10} mol/mm^3	Calc.[2]
Hydrogen reference concentration, $c_{H2,\,ref}$	2.83×10^{-9} mol/mm^3	Calc.[3]
Solubility coefficient for the cathode, $h_{d,c}$	0.19	Est.[2]
Solubility coefficient for the anode, $h_{d,a}$	0.64	Calc.[3]
Entropy of reaction – anode, $s^0_{f,a}$	42.5 J/mol-K	Calc.[4]
Entropy of reaction – cathode, $s^0_{f,c}$	126.8 J/mol-K (liq wtr) 64.8 J/mol-K (wtr vpr)	Calc.[4]

Notes:
[1] Calculated from inlet conditions.
[2] Estimated from data in [22] at a temperature of 343 K and fully humidified O_2 pressure of 1 atm.
[3] Calculated from data in [12] at a temperature of 353 K and H_2 pressure of 1 atm.
[4] Based on anode and cathode half reactions.
[5] Based on data in [19].

Table A2 Structural parameters and operating conditions for the basecase model

Property	Value	Source
Gas channel length, W_{gc}	30.0 cm	Measured
Gas channel length, L_{gc}	1.0 mm	Measured
Gas channel height, H_{gc}	1.0 mm	Measured
Collector thickness, t_{col}	1.5 cm	Measured
Anode GDL thickness, t_{agdl}	0.254 mm	Est.[1]
Cathode GDL thickness, t_{cgdl}	0.254	Est.[1]
Gas diffusion layer void fraction, ε_{gdl}	0.375	Est.[1]
Catalyst layer thickness, t_{cat}	0.013 mm	Measured
Pt and carbon volume fraction in the catalyst layer, ε_{cat}^{C}	0.45	Calc.[2]
Catalyst layer void fraction, ε_{cat}	0.31	Calc.[2]
Polymer volume fraction in the catalyst layer, ε_{cat}^{p}	0.24	Calc.[2]
Membrane thickness, t_m	0.0508 mm	Measured
Cell temperature, T_{cell}	353 K	Measured
Outlet pressure, P_{cell}	101 kPa	Measured
Air inlet relative humidity, Rh_c	100%	Measured
Fuel inlet relative humidity, Rh_a	100 %	Measured
Theoretical open circuit voltage, E_{th}	1.18	Calc.[3]
Open circuit voltage, V_{oc}	Varies	Measured
Specific reaction area of the catalyst layer, A	7000 mm^{-1}	Measured
Mean agglomerate size, L_{aggl}	1.0 μm	Data fit[4]
Tortuosity of the GDL, τ_{gdl}	8.0	Data fit[4]
Evap./cond. mass transfer coefficient, ψ_e, ψ_e	0.0011 $g/mm^3 \cdot s$	Equil.[5]
Dissolved/vapor mass transfer coefficient, h_m	5000 s^{-1}	Equil.[6]

Notes:

[1] Estimated from the uncompressed thickness, void fraction, and degree of compression.

[2] Calculated from the catalyst layer composition and mass.

[3] Calculated from Nernst equation for base case reactant temperature, pressure, and composition.

[4] Property adjusted (within the range reported in the literature) to fit the data.

[5] Chosen large enough to maintain equilibrium between liquid and vapor phases.

[6] Chosen large enough to maintain equilibrium between dissolved and vapor phases.

Appendix B: Fuel cell test data

Fuel cell testing, for the purpose of model validation as discussed in Section 6, was performed over a range of operating conditions. Figures B1-B6 show the performance of the test fuel cell for inlet pressures ranging from 0 psig to 30 psig, anode relative humidity ranging from 50% to 100%, cell temperature ranging from 40C to 80C, cathode stoichiometric ratios of 2.0 and 5.0, and anode stoichiometric ratios of 1.3 and 5.0, respectively. Baseline conditions apply to all parameters other than that which is varied. Error bars are shown indicating the uncertainty associated with the current density and voltage measurements.

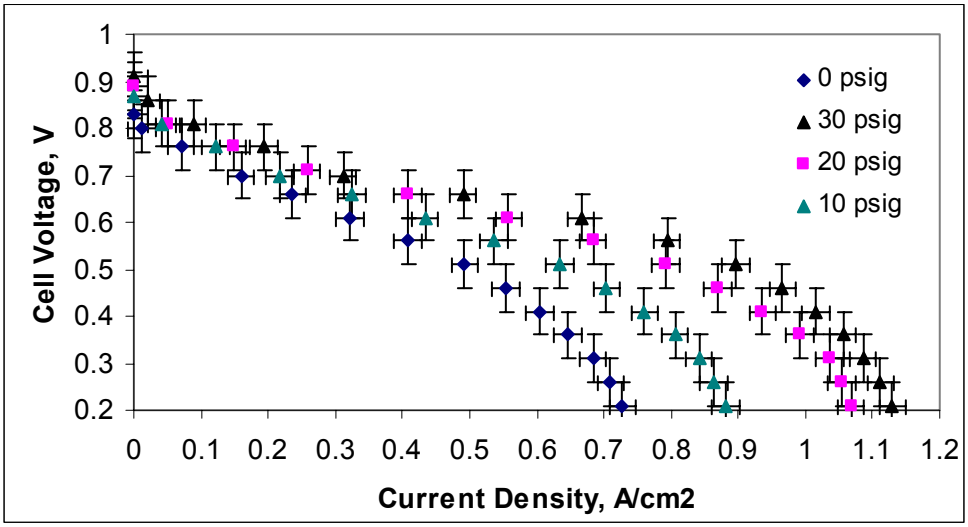

Figure B1 Variation in cell performance with inlet pressure. Anode and cathode pressure is the same.

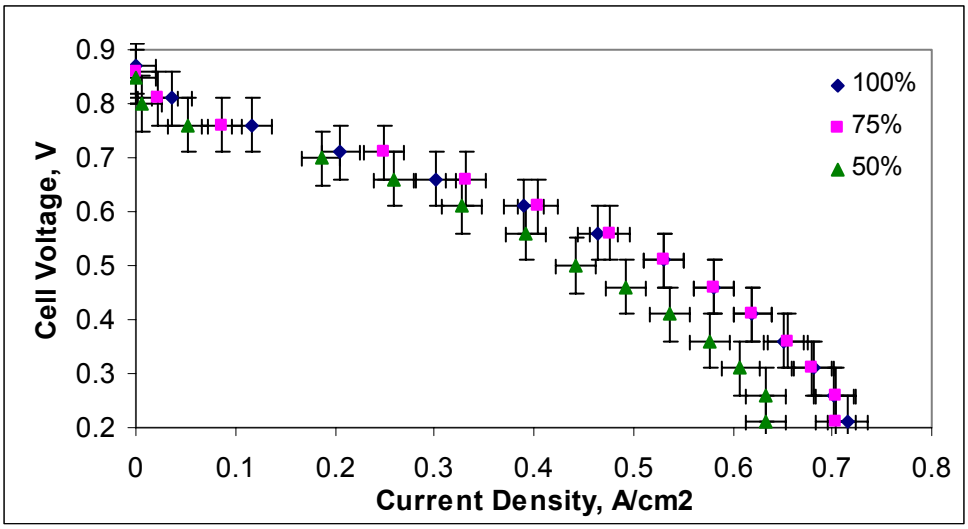

Figure B2 Variation in cell performance with anode inlet relative humidity. This is the original data set which was determined to be invalid for the 50% Rh case. The test cell was not given sufficient time to re-equilibrate following the change from 100% Rh to 50% Rh. The test was repeated.

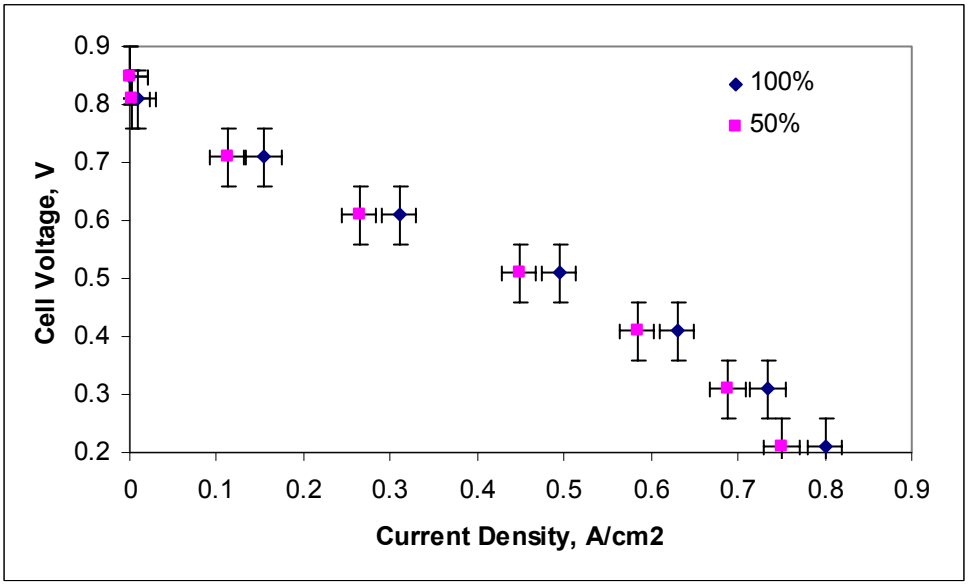

Figure B3 Variation in cell performance with anode inlet relative humidity. This data set was taken allowing sufficient time for the test cell to re-equilibrate following the change in anode relative humidity from 100% to 50%.

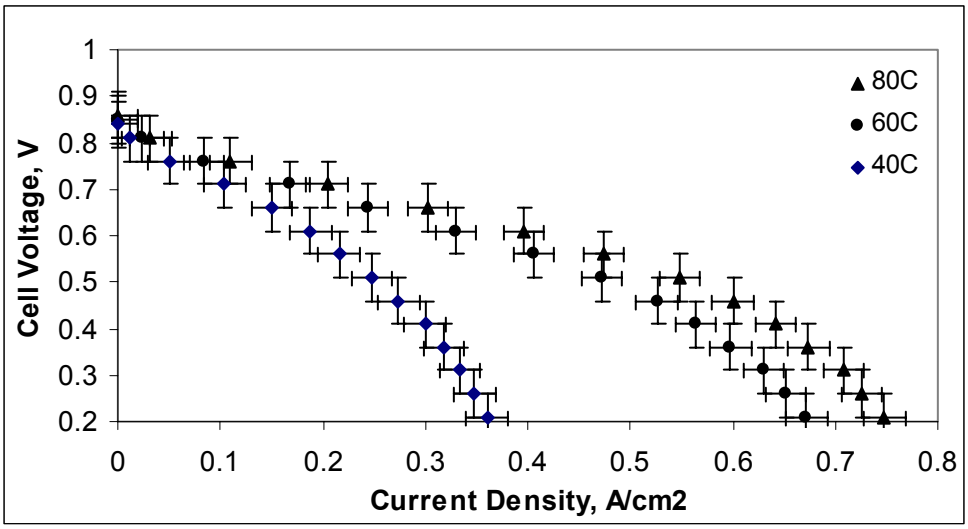

Figure B4 Variation in cell performance with cell temperature.

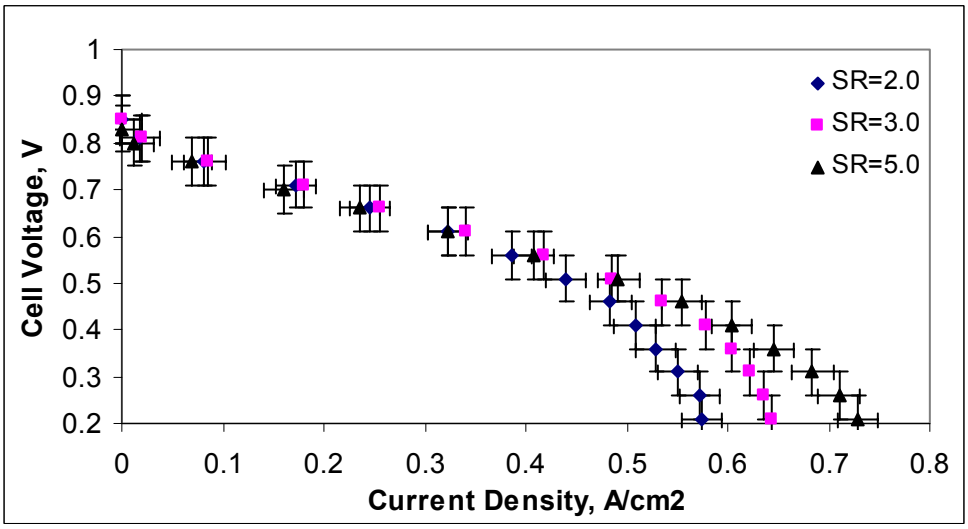

Figure B5 Variation in cell performance with cathode inlet stoichiometric ratio.

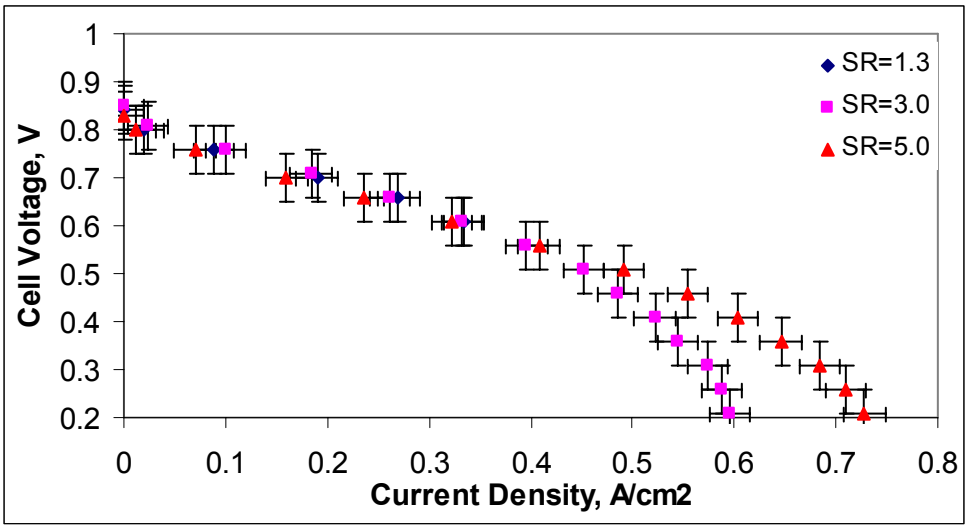

Figure B6 Variation in cell performance with anode inlet stoichiometric ratio.

The results presented in Figures B1-B6 were taken after the cell had undergone a 48 hour break-in period. During break-in, the cell was operated at 0.5V, 80 C, anode and cathode relative humidity of 100%, ambient exit pressure, and mass flow rates of 0.2 SLPM of H_2 and 0.47 SLPM of air, respectively.

Appendix C: SEM images

The microstructure of the test MEA was imaged using a scanning electron microscope (SEM). The imaging was helpful in estimating the catalyst layer thickness and porosity as well as in characterizing the microstructure; the agglomerate model for reactant transport within the catalyst is largely based on conclusions drawn from SEM analyses. The images presented in Figures C1-C6 are for the test MEA.

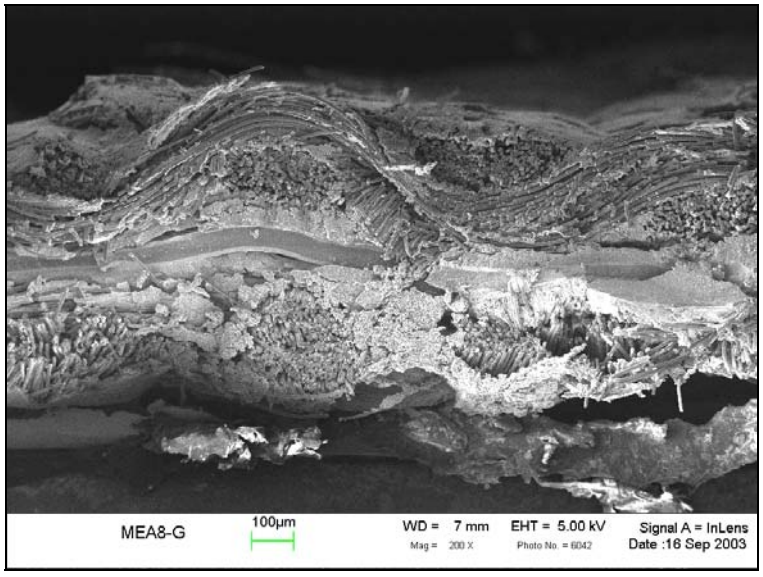

Figure C1 SEM image of the MEA after testing in the cell. The GDL is still attached to both sides, and deformation of the catalyst layer is evident. Magnification is 200X.

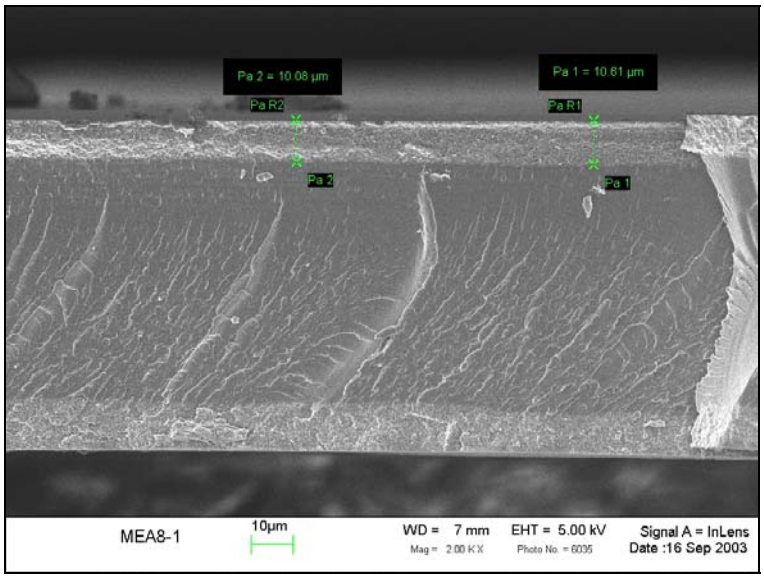

Figure C2 SEM image of the MEA before testing. The catalyst layer thickness shown is roughly 10 microns. Magnification is 2.0kX

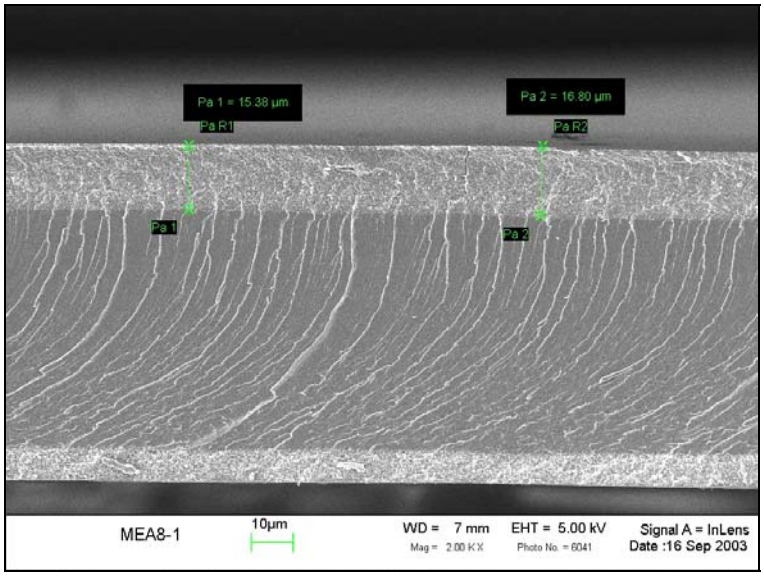

Figure C3 SEM image of the MEA before testing. The catalyst layer thickness shown is roughly 16 microns. Magnification is 2.0kX

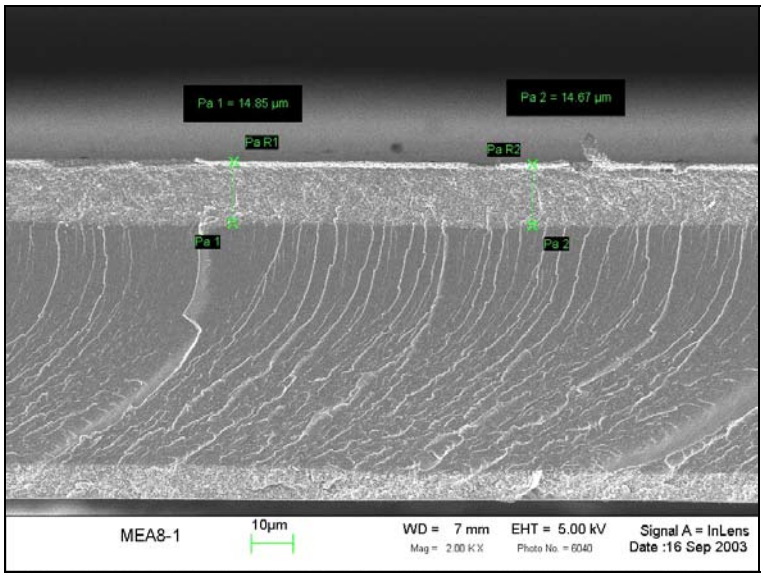

Figure C4 SEM image of the MEA before testing. The catalyst layer thickness shown is roughly 15 microns. Magnification is 2.0kX

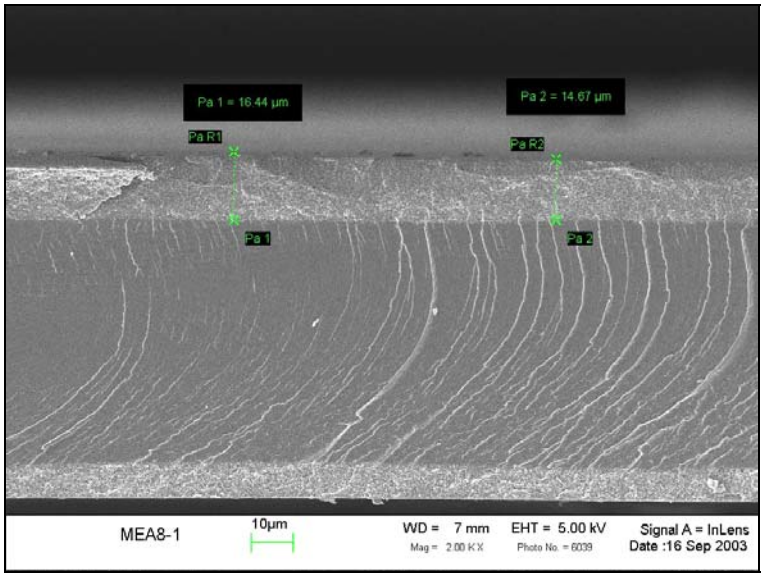

Figure C5 SEM image of the MEA before testing. The catalyst layer thickness shown is roughly 15 microns. Magnification is 2.0kX

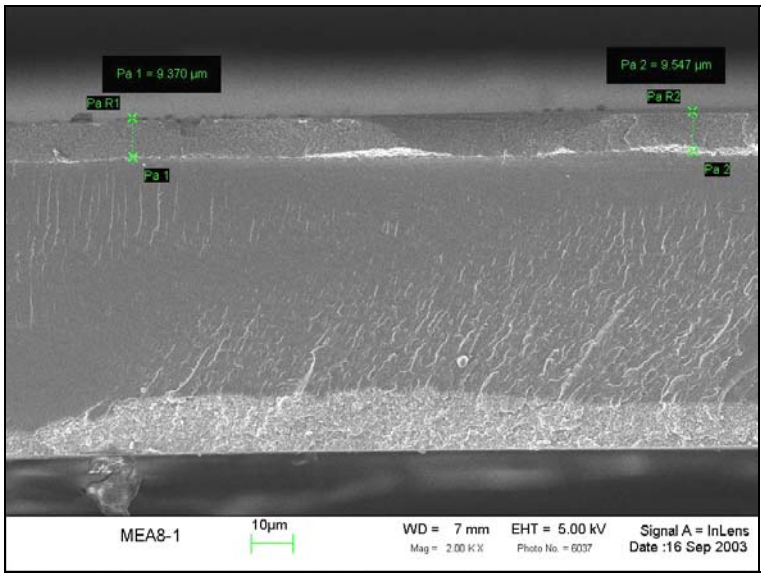

Figure C6 SEM image of the MEA before testing. The catalyst layer thickness shown is roughly 10 microns. Magnification is 2.0kX

Appendix D: Constructing the finite element geometry using FEMAP®

As discussed in Section 5, the numerical model of the fuel cell presented in this work is solved using a CFD code that is based on the finite element method. The first step in the solution process, which begins once the numerical formulation of the model has been completed, is the construction of the finite element model(s) that explicitly defines the computational solution domain. The construction of a finite element model includes the following four steps:

- Construct the model geometry
- Create the finite element mesh
- Apply the boundary conditions
- Export the completed finite element model to the CFD solver

All four of these steps are done using FEMAP®, a finite element pre and post-processing software package.

Constructing a two-dimensional model geometry using FEMAP

The following procedure is used to construct the geometry for a two dimensional, down-the-channel fuel cell model in FEMAP. Specific menu commands, or command paths in FEMAP are indicated in bold type.

1) Beginning with a new model file, create a rectangle having the dimensions of the anode gas channel. Assume that the x direction is the direction through the thickness of the cell, and the y direction is down the channel.
2) Turn on **Update surfaces**
3) Create a boundary surface from the rectangle. Use **Boundary surface – from curves - select all.**
4) Create a rectangle, adjacent to the anode gas channel, having the dimensions of the anode gas diffusion layer. As a rule, it is best to create the geometry so that each

component of the fuel cell is adjacent to the one created in the previous step, the alternative requires that the components be repositioned.

5) Create a boundary surface by selecting the curves on this new rectangle.
6) Create a rectangle having the dimensions of the anode catalyst layer.
7) Create a boundary surface by selecting the curves on this new rectangle.
8) Create a rectangle having the dimensions of the anode special region.
9) Create a boundary surface by selecting the curves on this new rectangle.
10) Create a rectangle having the dimensions of the membrane.
11) Create a boundary surface by selecting the curves on this new rectangle.
12) Create a rectangle having the dimensions of the cathode special region.
13) Create a boundary surface by selecting the curves on this new rectangle.
14) Create a rectangle having the dimensions of the cathode catalyst layer.
15) Create a boundary surface by selecting the curves on this new rectangle.
16) Create a rectangle having the dimensions of the cathode gas diffusion layer.
17) Create a boundary surface by selecting the curves on this new rectangle.
18) Create a rectangle having the dimensions of the cathode gas channel layer.
19) Create a boundary surface by selecting the curves on this new rectangle.

Constructing the finite element mesh for a two-dimensional model using FEMAP

1) Define the properties of each component. This has nothing to do with the actual material properties, but is simply a way of labeling the components. Select **Model – Property**. For property 1, write Anode Gas Channel for the title, check that the element type is plate, and hit **OK**. Hit **OK** again to create Material 0, hit **OK** again and enter the remaining property titles, one for each component of the model. It is not necessary to specify material properties in FEMAP®, this will be done later in CFDesign®.
2) Select **Mesh – Mesh Control – Attributes on surface.** Highlight a surface and apply the appropriate property when prompted. Repeat for all of the surfaces in the model.

3) Define the mesh. Select **Mesh – Mesh Control – Size Along Curve.** Select a curve or curves and hit **OK.** Enter the number of elements along the curve as well as any biasing information. Repeat this step for all of the curves in the model.
4) Select **Mesh – Mesh Control – Approach on Surface.** Select one of the surfaces. Select **Mapped Four Corners**. Enter the numbers representing the points on the corners of the surface that was selected. Repeat for all of the surfaces.
5) Mesh the surfaces. Select **Mesh – Geometry – Surface.** Select one of the special regions. Under **Property** it should say **Use mesh attributes,** and under **Shape**, **Quads** should be selected. Hit **OK** and the selected surface will be meshed.
6) Check the mesh. If it looks bad it is likely a result of improperly specifying the number of elements along the curves bounding the surface or because the **Approach on surface** was not done.
7) Mesh the remaining surfaces individually. Meshing all of the surfaces at once will result in a bad mesh.
8) Merge the coincident nodes. When surfaces sharing a boundary are meshed, the operation results in the creation of two nodes at any given position along this boundary. These nodes must be merged. Select **Tools – Check – Coincident nodes.** Enter a distance that is smaller than that between any two nodes in the densest part of the model mesh. What this will do is merge all nodes that are separated by a distance less than the number specified.

Applying boundary conditions to a two-dimensional model using FEMAP

1) Center the model in the window. **CTRL-A.**
2) Define two load sets. The first set is for the initial conditions, the second set is for boundary conditions. Select **Model-Load-Set**. The title for load set number 1 should be "Initial". CFDesign® will read these loads as initial conditions.
3) Now that load set one is active, apply the appropriate loads to the model. All initial conditions are applied directly to the nodes. Select **Model-Load-Nodal**. When the dialog box comes up, select **Method-On Surface**. Highlight the surfaces containing the nodes on which a specific initial condition will be applied and hit **OK**. A load

description dialog box will come up. For initial conditions on user defined equations (extra scalars) the type of load is called **General Scalar.** Select **General Scalar** and enter a value of -1. This will mark all of the nodes on the selected surface(s) with a scalar value of 1. CFDesign® recognizes any load with a negative sign as pertaining to a user defined variable.

4) Continue applying initial conditions on the remainder of the model. Separate initial conditions should be used for the anode and cathode sides. For instance, if the cathode is marked with general scalar = -1, the anode should be marked with a general scalar of -2.
5) Select **Model-Load-Set.** Enter the number 2 for the load set number, and erase any writing from the title (leave it blank). Load set 2 will contain the boundary conditions.
6) Apply the boundary conditions to the curves making up the outer boundaries of the model. Select **Model – Load – On Curve.** Select the curve on which the BC is to be applied; the load dialog box will appear.
7) On the inlet to the anode gas channel apply: flow velocity, a general scalar marking the inlet, and a marker for a flux boundary condition (this may or may not actually be used). **Rotational acceleration** in the **x-direction** is used to mark a flux BC. Input a *positive* number that is different from any of the other numbers used to mark loads.
8) The cathode gas channel inlet has similar boundary condtions.
9) The outlets to the gas channels should both have **Static fluid pressure** values of zero applied as well as **general scalars** and **rotational acceleration in the x-direction**.
10) The outer boundaries of the porous sections of the cell (catalyst layers and GDL's) should be marked with a **Slip Wall Condition.** This is necessary if the Darcy equation for momentum is being solved in these regions.
11) The boundaries along the gas channels should also be marked with **general scalars**, but not with flux BC's (rotational acceleration).
12) Once all loads have been applied to the appropriate curves, the loads must be mapped to the nodes associated with these curves. Select **Model – Load – Expand.** Hit **OK** to expand all loads in the set.

13) The model is now complete. Export the FEMAP® neutral file to the appropriate directory. Select **File-Export-FEMAP neutral.** A dialog will come up, select version 7.1 and make sure to export the **Entire model.**

Constructing a three-dimensional model geometry using FEMAP®

1) The 3D geometry is extruded from the 2D geometry. The first step is to create a 2D geometry using the procedure outlined above.

Constructing the finite element mesh for a three--dimensional model using FEMAP®

1) Size the curves on the 2D geometry and mesh according to the procedure outlined above (do not merge coincident nodes, this will be done later). A generic 2D **Property** should be used for all of the fuel cell components in this mesh.
2) Create a **Property** for each of the components in the 3D model. Unlike the 2D model, the type of elements used for these properties will be solids (not plate elements).
3) Now extrude the mesh in the direction along the channel. Select **Mesh – Extrude – Element** and select the elements from an individual surface on the 2D geometry. Enter the length to extrude as well as the number of elements along the extrusion. Make sure it is being extruded as a new part.
4) When the mesh dialog comes up, select the appropriate **Property** for the section being extruded. Hit **OK.**
5) Now merge the coincident nodes just as was done for the 2D model.

Applying boundary conditions to a three-dimensional model using FEMAP

1) Create the necessary load sets, one and two (set one has the title "Initial").
2) Create a **Group** for each of the fuel cell components. Select **Group – Operations – Generate – Element** and choose **Property** as the method of element selection. Label each group according the name of the component. Once a group of elements is

created, display it by itself by selecting **Ctrl-S** and selecting **Model data – Group – Active.**

3) Add nodes to the group by selecting **Group – Nodal** and using **On Element** as the node selection method. Select all elements displayed.
4) Do steps 2 and three for each component.
5) Now, apply the initial conditions by displaying one group at a time and applying the appropriate general scalar load.
6) Switch to load set two.
7) Apply boundary condition loads at the original 2D surface.
8) Apply boundary conditions at the opposite end by selecting **Load – Nodal** and **Free Surface** as the method of selection. This allows you to select only those nodes on the surface of the mesh. A similar procedure may be used to apply the boundary conditions along the length of the gas channels.
9) Once the boundary conditions are finished, export the FEMAP neutral file.

Appendix E: Setting up a CFD analysis in CFDesign®

The procedure for setting up an analysis in CFDesign® is presented in this section. The process involves the following steps.

- Write the code representing the set of transport equations.
- Write the code defining all closure relations.
- Set up the solution parameters.

Coding the transport equations

The transport, or governing equations, are input to CFDesign® via the file exscal.eqn. Within this file, a section is set aside for each equation. Within each section, the transport equation is broken down into advective, diffusive, and source term components. The equation must be expressed in the form shown in Eq. E1 prior to coding. Expressing the equation in this form facilitates the separation into advective, diffusive, and source term components.

$$\rho u_x \frac{\partial \varphi}{\partial x} + \rho u_y \frac{\partial \varphi}{\partial y} + \rho u_z \frac{\partial \varphi}{\partial z} = \frac{\partial}{\partial x}\left(D_\varphi \frac{\partial \phi}{\partial x} \right) + \frac{\partial}{\partial y}\left(D_\phi \frac{\partial \varphi}{\partial y} \right) + \frac{\partial}{\partial z}\left(D_\varphi \frac{\partial \varphi}{\partial z} \right) + S_\varphi \qquad \text{(E1)}$$

An example of a typical entry for a transport equation in exscal.eqn is given below.

The first line gives the version of CFDesign with which this file will work.

The next line indicates which equation is being built and which form of that equation. For example, assuming that the energy equation was being built, in "exscal.eqn" you would see:

5.1-0
EXTRA 1

This indicates that the energy equation is being built and is the first variable defined.

In the comments to follow, you see that this is the incompressible static energy or temperature equation.

Following this line, is the number of primary or dependent variables that will be needed to build this equation. For example,

```
7       // There are 7 variables
kU      // U momentum is needed to establish the advection terms in the energy eqn
kV      // V momentum is needed to establish the advection terms in the energy eqn
kW      // W momentum is needed to establish the advection terms in the energy eqn
kP      // Pressure is needed to establish the flow for the advection of energy
kT      // Temperature dependent variable
kKin    // Turbulent Kinetic energy is needed for turbulent flow
kDiss   // Turbulent energy dissipation is needed for turbulent flow
```

Next is the number of property variables needed to build this pde. For example,

```
3
kRho    // density for advection and transient terms
kCond   // conductivity for diffusion or conduction terms
kCp     // specific heat for advection or transient terms
```

Next is the number of calculation variables. This should probably not be calculated. These variables are used as scratch vectors either during the form (like in the advection terms) or during the solve (like in the pre-conditioner).

Next is the number of constant factors. These include things like the gravitational vector, rotational vector, constants for the turbulence model, ...

Then, the pde equation sections follow.

Transient

This section is used for just the transient terms.

The first line in this section has the flag indication whether the transient terms are on (> 0) or off (= 0). You will see various positive numbers for this flag. These numbers are also codes to indicate which transient scheme to use for this variable. The safest number to use for this is "1". "1" is the flag for our default 1st order backward difference which is very stable, albeit not as accurate as some of the other schemes available.

The second number on this line is the number of variable factors that are in the transient term. For the energy equation, there are 2 factors: density and specific heat.

So, for the energy equation, the transient section would appear as:

*** Transient
1 2 On/Off, number of factors
kRho density
kCp specific heat

Advection

This section is used for both the advection (or convection) and the transient terms if no separate transient section is included in the file.

The first line in this section has the flag indication whether the advection and transient terms are on (> 0) or off (= 0). You will see various positive numbers for this flag. These numbers are also codes to indicate which advection scheme to use for this variable. The safest number to use for

this is "1". "1" is the flag for our default streamline upwind which is very stable, albeit not as accurate as some of the other schemes available.

The second number on this line is the number of variable factors that are in the advection or transient term. For the energy equation, there are 2 factors: density and specific heat.

So, for the energy equation, the advection section would appear as:

*** Advection
1 2 On/Off, number of factors
kRho density
kCp specific heat

Diffusion

This section is used for the diffusion or conduction terms.

The first line in this section has the flag indication whether the diffusion term is on (> 0) or off (= 0).

The second number on this line is the number of variable factors that are in the diffusion term.

The third number on this line is the number of variable codes that will be used to define the diffusion term. There could be only one factor in the diffusion term, but the factor may be different in each of the three coordinate directions.

The second line is the Schmidt or Prandtl number to be used for turbulent flow. In turbulent flow, we use the Reynolds analogy that all fluxes can be related to the

momentum flux by use of a Prandtl/Schmidt number. For laminar flows, this value should be 1.0.

The second line indicates that there is a different Y diffusion coefficient than for the X diffusion term. If this value is 0, the Y diffusion coefficient is the same as the X diffusion. If it is "1", it is different.

The third line indicates that there is a different Z diffusion coefficient than for the X diffusion term. If this value is 0, the Z diffusion coefficient is the same as the X diffusion. If it is "1", it is different.

The next lines contain the variables that are needed in the diffusion terms. The first variable is listed for all three directions unless the Y and Z offsets are zero. In that case, only one line is used for the first diffusion coefficient or variable. Both the variable needed for laminar flow and the variable needed for turbulent flow should be listed. The other variables needed follow.

For the energy equation, the diffusion section looks like:

*** Diffusion
1 1 1 On/Off, number of factors, number of codes
1.0 PrSc
0 Y-offset
0 Z-offset
kCond kCeff Laminar kCode label (conductivity), turbulent kCode label (effective conduct.)

For the pressure equation, the diffusion-like terms are different in each of the 3 coordinate directions. However, they are the same for laminar and turbulent flow. The diffusion section of the pressure equation looks like:

*** Diffusion

1 2 6 On/Off, number of factors in each diff. term, number of codes

1.0 PrSc

1 Y-offset (y is different from x)

1 Z-offset (z is different from x)

kRho kRho Laminar kCode value, turbulent kCode value - both are density

kRho kRho first term in all three coord. directions is the density

kRho kRho

kKSubU kKSubU the x-direction term is determined from the U-velocity equation

kKSubV kKSubV the y-direction term is determined from the V-velocity equation

kKSubW kKSubW the z-direction term is determined from the W-velocity equation

Source Terms

This section is used for all general source terms. The following example illustrates how a source term in input to exscal.eqn.

Example:

```
Source = rho*omega**2*X + rho*omega*v - .5*K*rho*u**2
     + visc/X**2*dvdy + C*visc*u + u**(1/3)
```

Number of terms (divided by + or -) is nTerms:

```
nTerms = 6      > rho*omega**2*r, rho*omega*v, -.5*K*rho*u**2
                  visc/r**2*dvdy, C*visc*u, u**(1/3)
```

Number of constants in the terms is nConFac:

```
nConFac = 4     > omega, -.5, K, C
```

Number of coordinate factors (X, Y, Z) is nCoorFac:

nCoorFac = 1 > X

Number of derivative factors is nDerivFac:

nDerivFac = 1 > dvdy

Number of field variable (variables stored at every node) is nVarFac:

nVarFac = 4 > rho (density), v (velocity), u, visc (viscosity)

Number of exponent factors is nExpFac:

nExpFac = 1

The coordinate direction that is referred to in nCoorFac is SelCoor:

SelCoor(1) = 1 > X (X is 1, Y is 2, Z is 3)

(If nCoorFac > 1, there would be other SelCoor for each factor)

The variable in the derivative factor is DerFacCode:

DerFacCode(1) = kV > dvdy

(If nDerivFac > 1, there will be a DerFacCode for each factor)

The derivative coordinate direction is DerivCoor:

DerivCoor(1) = 2 > dvdy (X is 1, Y is 2, Z is 3)

(If nDerivFac > 1, there will be a DerivCoor for each factor,
corresponding to the DerivCoor)

The codes for the variables are stored in VarFacCode:

VarFacCode(1) = kRho
VarFacCode(2) = kV
VarFacCode(3) = kU
VarFacCode(4) = kVisc

The codes for the exponent factors are stored in ExpFacCode:

ExpFacCode(1) = kU

The exponents for the exponent factors are stored in ExpFacExp:

ExpFacExp(1) = 0.3333

The constant factors are stored first in ConFac, then the other factors
needed are stored after the constants:

ConFac(1) = Omega
ConFac(2) = -.5
ConFac(3) = K
ConFac(4) = C
ConFac(5) = r
ConFac(6) = dvdy
ConFac(7) = rho
ConFac(8) = v

ConFac(9) = u

ConFac(10) = visc

ConFac(11) = u**(1/3)

The number of denominator factors in each term is nDenomFac:

nDenomFac(1) = 0

nDenomFac(2) = 0

nDenomFac(3) = 0

nDenomFac(4) = 2

nDenomFac(5) = 0

nDenomFac(6) = 0

The factors in the denominators are stored in DenomFac and refer to the way the factors were stored in ConFac:

DenomFac(1,4) = 5 > r : ConFac(5)

DenomFac(2,4) = 5

The number of numerator factors in each term is stored in nNumFac:

nNumFac(1) = 4

nNumFac(2) = 3

nNumFac(3) = 5

nNumFac(4) = 2

nNumFac(5) = 3

nNumFac(6) = 1

The factors in the numerators are stored in NumFac and refer to the way the factors were stored in ConFac:

```
NumFac(1,1) = 7        > rho : ConFac(7)
NumFac(2,1) = 1        > omega : ConFac(1)
NumFac(3,1) = 1
NumFac(4,1) = 5        > r : ConFac(5)
NumFac(1,2) = 7        > rho
NumFac(2,2) = 1        > omega
NumFac(3,2) = 8        > v : ConFac(8)

NumFac(1,3) = 2        > -.5 : ConFac(2)
NumFac(2,3) = 3        > K : ConFac(3)
NumFac(3,3) = 7        > rho
NumFac(4,3) = 9        > u : ConFac(9)
NumFac(5,3) = 9
NumFac(1,4) = 10        > visc : ConFac(10)
NumFac(2,4) = 6        > dvdy : ConFac(6)
NumFac(1,5) = 4        > C : ConFac(4)
NumFac(2,5) = 10        > visc
NumFac(3,5) = 9        > u
NumFac(1,6) = 11        > u**(1/3)
```

The code for whether the integrated term should be multiplied by the shape function or one of its derivatives is stored in nShapFac:

```
nShapFac(1) = 4      > shape function (1 = DWDX, 2=DWDY, 3=DWDZ, 4=W)
nShapFac(2) = 4
nShapFac(3) = 4
nShapFac(4) = 4
nShapFac(5) = 4
nShapFac(6) = 4
```

The flag for whether the term should be a diagonal factor (on the LHS of the

equation) or a source term (RHS of the equation) is stored in DiagFac:

DiagFac(1) = 0 > diagonal factor (=1), RHS factor (=0)
DiagFac(2) = 0
DiagFac(3) = 0
DiagFac(4) = 0
DiagFac(5) = 0
DiagFac(6) = 0

The way this data would appear in the .eqn file is:

```
*** Source
1 5 4 1 1 4 0    On/Off nTerms nConFac nCoorFac nDerivFac nVarFac nExpFac
4             nNumFac(1)
7                  NumFac(1,1)
1                  NumFac(2,1)
1                  NumFac(3,1)
5                  NumFac(4,1)
0               nDenomFac(1)
4               nShapFac(1)
0               DiagFac(1)
3             nNumFac(2)
7                  NumFac(1,2)
1                  NumFac(2,2)
8                  NumFac(3,2)
0               nDenomFac(2)
4               nShapFac(2)
0               DiagFac(2)
5             nNumFac(3)
2                  NumFac(1,3)
```

```
3                NumFac(2,3)
7                NumFac(3,3)
9                NumFac(4,3)
9                NumFac(5,3)
0              nDenomFac(3)
4              nShapFac(3)
0              DiagFac(3)
2            nNumFac(4)
10                NumFac(1,4)
6                NumFac(2,4)
2              nDenomFac(4)
5                DenomFac(1,4)
5                DenomFac(2,4)
4              nShapFac(4)
0              DiagFac(4)
3            nNumFac(5)
4                NumFac(1,5)
10                NumFac(2,5)
9                NumFac(3,5)
0              nDenomFac(5)
4              nShapFac(5)
0              DiagFac(5)
1            nNumFac(6)
11                NumFac(1,6)
0              nDenomFac(6)
4              nShapFac(6)
0              DiagFac(6)
500          ConFac(1)   omega = 500
-0.5         ConFac(2)
.33          ConFac(3)   K = .33
.014         ConFac(4)   C = 0.14
```

1 SelCoor(1) this coordinate will be stored in ConFac(5)
kV DerFacCode(1) this derivative will be stored in ConFac(6)
2 DerivCoor(1)
kRho VarFacCode(1) this variable will be stored in ConFac(7)
kV VarFacCode(2) this variable will be stored in ConFac(8)
kU VarFacCode(3) this variable will be stored in ConFac(9)
kVisc VarFacCode(4) this variable will be stored in ConFac(10)
kU ExpFacCode(1) this exponent factor stored in ConFac(11)
0.3333 ExpFacExp(1)

P Source

This section is only used for momentum equations. It represents the pressure source terms in those equations.

BC

This section is used to describe flux boundary conditions, both nodal and elemental.

Example: In the energy equation, there are two flux boundary conditions. There is a specified heat flux, q and a film coefficient boundary condition, h(Tamb-T). Both of these are fluxes across element faces. We currently do not support nodal bc fluxes.

Since the flux integrals are surface integrals for 3D and line integrals for 2D analyses, there will be flux integrals in each of the coordinate directions.

The nomenclature for source terms is repeated here.

nTerms - the number of terms in the flux integrals. There will be an "nTerms" for all 3 coordinate directions.

nSurfFac - similar to ConFac for source terms. This is the number of constant factors in the flux integrals.

nVarFac - the number of dependent variable factors

nNumFac - the number of numerator factors in each of the coordinate dirs.

nFluxFac - this is a flag that indicates whether direction is on (= 1) or off (= 0). That is, the flux is represented by dotting the magnitude with the element face normal.

DiagFac - flag that indicates whether the flux term should be added to the RHS (= 0) or to the matrix diagonal (= 1)

```
*** BC
0       Node BC - On/Off          // Nodal flux bc's are off
1       Element BC - On/Off       // Element flux bc's are on for this equation
2       Number of element BC types// There are 2 element BC types
kHeatFlux   First element BC type // The first is a heat flux BC type
1  1  1    nTerms (x y z)        // There is 1 terms in each of the 3 coordinate dirs.
0       nSurfFac                  // There are no constant factors in the surface int.
0       nVarFac                   // There are no variable factors
0       nNumFac (x + y + z)       // There are no other numerator entries - just the
0                                 //    flux value itself
0
1       nFluxFac                  // The flux integral is directional dependent
0       Diag Fac (x + y + z)  // These terms are source terms, not diagonals
```

```
0
0
kFilmCoef   Second element BC type// The second BC type is a film coefficient
2 2 2       nTerms (x y z)              // There are 2 terms h*Tamb and -h*T
0           nSurfFac                    // There are no additional constant factors
0           nVarFac                     // There are no additional variable factors
0           nNumFac (x + y + z)         // There are no additional numerator entries
0
0
0
0
0
1           nFluxFac                    // The flux integral is directional dependent
1           Diag Fac (x + y + z)  // The first term for X direction is a diagonal.
0                                       // THe second term for X is a source term.
1                                       // The first term for Y direction is a diagonal.
0                                       // The second term for Y is a source term.
1                                       // The first term for Z direction is a diagonal.
0                                       // The second term for Z direction is a source term.
```

Coding the closure relations

The closure relations, which may include definitions for source terms, material properties, and other information needed to completely define the numerical model, are input to CFDesign® via the file uservar.c. Uservar.c is programmed in C++. The file can be broken down into three components: Variable declaration, global variable / property definition, and local variable / property definition. Figure E1 is an illustration of the structure of uservar.c.

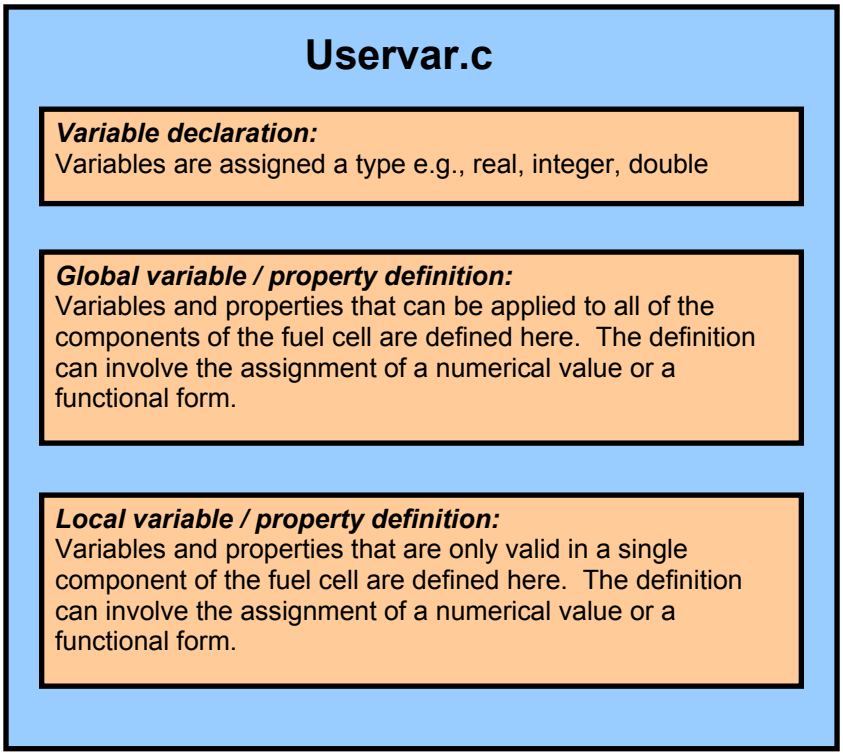

Figure E1 Structural diagram of uservar.c

Setting up the solution parameters

When a new model is created for solution with CFDesign®, it is necessary to first set up the solution parameters that control how the numerical model is read, solved, and how the results are output. Most of this can be done from the CFDesign® graphical user interface (GUI). The following procedure is used to set up a new model from the GUI once exscal.eqn, uservar.c, and the FEMAP® neutral file have been created. Operations involving a specific menu path are given in bold type.

1) Create and launch an executable from Visual C++®
2) Select **File – New** from the GUI menu. This launches a new control (.ctl) file. The name of the file will be the same as that of the neutral file (.neu) on which it is based.
3) Select the **Options** tab to bring up the dialog window.
4) Set the units, flow conditions, and check the box marked **General Scalar** under **Optional Parameters**.

5) Select the **Output** tab. Click on the box corresponding to **Scalar** under **Basic Flow Values**.
6) Select **Properties – Fluids**. This brings up the fluid properties dialog window. Hit **Delete.**
7) Hit **New**. Pull down the **Existing Property IDs** menu and select any one of the components that are to be considered fluids (this includes all of the cell components except the membrane and the special regions). Hit **Ok.**
8) Under **Name** select **User Defined**. Hit the tab for **Viscosity** and enter the mixture viscosity to be used in the current component.
9) If the component is porous, check **Extended Attributes** and enter a value for the permeability.
10) Repeat steps 7 – 9 for all of the properties, and then hit **OK** to exit.
11) Select **Properties – Solids**. Repeat steps 7-8 for the membrane and special regions.
12) Select **Control – Fuel Cell.**
13) Every variable used in the model is defined here. Solution variables (variable representing transported quantities e.g., water vapor mass fraction or energy) are given a non-zero value in the molecular weight field. This signals to the solver that the variable corresponds to an equation defined in exscal.eqn. To input the individual variables. Select **New** and enter the **Scalar ID,** corresponding to the numerical label given to the variable, as well as a title. A non-zero number must be entered in the molecular weight field for solution variables.
14) Repeat step 13 until all variable have been defined.
15) The values for the boundary conditions, which are applied to the boundaries marked in FEMAP®, can now be defined.
16) Select a **Scalar Number** corresponding to a solution variable. Select the **Inlet Number** corresponding to the boundary on which the Dirichlet boundary condition is to be applied. Enter a value for the boundary condition, hit **Update BC Value**. Repeat for all Dirichlet boundary conditions for this scalar.
17) If the solution variable requires the specification of a flux condition, select **Flux BC No.** input the value of the flux at the appropriate boundary, hit **Update Flux**.
18) Repeat steps 16 and 17 for all solution variables.

19) The analysis is started by first selecting the **Analysis** tab. Input the number of iterations to run. Hit **Analyze.**

20) Once the analysis is complete, or when it diverges, open up the control file in Visual C++®. All of the parameters set in the GUI can be modified using Visual C++ as a text editor.

21) Scroll to the bottom of the control file to the section labeled as follows:

*** Extra Scalar Solver: Name,Solver,Solve_iter,Debug,Solve_crit,Relax
Vapanode 1 60 1 0.000001 1.000000
Vapcathode 1 10 1 0.000001 1.000000
Potentialm 4 100 1 0.000001 1.000000

This is where the real magic happens. On each line of this section, the following information is given: which equation is being solved, what solver is being used, how many local iterations are taking place, what is the debug level, what is the change between successive local iterations required for convergence, and what level of under-relaxation is being used. Select the solver appropriate for the equation being solved. This is typically dependent on whether or not the equation is symmetric or non-symmetric (containing advective terms). Some of the solvers available in CFDesign are:

A. TDMA - this solves both symmetric and non-symmetric equations. Its numerical label is 1. The number of recommended internal iterations is between 1 and the square root of the number of nodes in the model.
B. PCCG – this solves symmetric equations. Its numerical label is 3. The number of recommended internal iterations is more than 10.
C. SPCCG – this solves both symmetric and non-symmetric equations. Its numerical label is 4. The number of recommended internal iterations is more than 10.
D. BiCGStab – this solves non-symmetric equations. Its numerical label is 6. The number of recommended internal iterations is more than 1000.

The highest probability of successfully solving a given equation can be achieved using either the TDMA or SPCCG solvers.

The Solve_Crit value should be set to three orders of magnitude less than the required precision of the solution variable. For instance, if the temperature solution is required to a precision of one decimal place (300.1) then the Solve_Crit value should be set to 0.0001.

In general, a fair amount of trial and error is involved in determining the correct solver and number of internal iteration required for any given equation.

22) Below the Scalar Solver section is the following text:

*** Constants
kExtConv 34
kInflate 0 0 1 3 0 1 3 0.5 1 0.01
kAutoYP 0 1 36 1 300.000000 1

The second line, kExtConv 34, sets the scalar that is displayed on the GUI during the solution. In this case, scalar variable 34 is displayed. This line can be edited to display any of the solution variables. The only stipulation is that only one variable can be displayed at a time.

23) Once the modifications have been made to the equation solvers and display settings, save the control file and re-launch the executable. Open the control file and start another analysis.

Vita

Nathan Siegel was born in Long Beach, California, in 1975. His career as a professional student began in 1993 at Palomar Community College. Following a two year stay at Palomar, Nathan moved on to Cal Poly, San Luis Obispo, where he received a B.S. degree in mechanical engineering in 1998. Forced to move south by El Niño, Nathan spent the next two years in San Diego attending San Diego State University. He received a M.S. degree in mechanical engineering in 2000. With the exception of a brief trip to Massachusetts when he was two years old, Nathan had never spent any time on the East Coast and decided that he wanted to see how folks lived over there. On July 23, 2003, Nathan left California in his truck with most of his worldly belongings and headed east. He arrived in Virginia three weeks later and began attending Virginia Tech. In January of 2004 Nathan received a Ph.D. in mechanical engineering. He is currently on sabbatical from his career as a professional student.